Chem Soc Rev

REVIEW ARTICLE

View Article Online
View Journal | View Issue

Cite this: *Chem. Soc. Rev.*, 2025, **54**, 983

Advances in the photon avalanche luminescence of inorganic lanthanide-doped nanomaterials†

Marcin Szalkowski,[ab] Agata Kotulska,[a] Magdalena Dudek,[a] Zuzanna Korczak,[a] Martyna Majak,[a] Lukasz Marciniak,[a] Malgorzata Misiak,[a] Katarzyna Prorok,[a] Artiom Skripka,[ce] P. James Schuck,[d] Emory M. Chan *[e] and Artur Bednarkiewicz *[a]

Photon avalanche (PA)—where the absorption of a single photon initiates a 'chain reaction' of additional absorption and energy transfer events within a material—is a highly nonlinear optical process that results in upconverted light emission with an exceptionally steep dependence on the illumination intensity. Over 40 years following the first demonstration of photon avalanche emission in lanthanide-doped bulk crystals, PA emission has been achieved in nanometer-scale colloidal particles. The scaling of PA to nanomaterials has resulted in significant and rapid advances, such as luminescence imaging beyond the diffraction limit of light, optical thermometry and force sensing with (sub)micron spatial resolution, and all-optical data storage and processing. In this review, we discuss the fundamental principles underpinning PA and survey the studies leading to the development of nanoscale PA. Finally, we offer a perspective on how this knowledge can be used for the development of next-generation PA nanomaterials optimized for a broad range of applications, including mid-IR imaging, luminescence thermometry, (bio)sensing, optical data processing and nanophotonics.

Received 12th July 2024

DOI: 10.1039/d4cs00177j

rsc.li/chem-soc-rev

1. Introduction

Photon avalanching (PA) is a highly nonlinear upconversion process in which the absorption of a single additional photon by a material produces a cascade of photophysical interactions that ultimately induce the emission of many photons, as shown in Fig. 1a. In PA, weak ground-state absorption (GSA) is followed by a sequence of efficient excited-state absorption (ESA) and energy cross-relaxation (CR) processes that are repeated in a positive feedback loop, which explains the high non-linearity and narrow 'window' in which PA is observed as well as the existence of PA threshold and saturation regions (Fig. 1b) in a pump power-dependent luminescence profile. For example, Tm^{3+}-doped $NaYF_4$ PA nanoparticles were recently shown to exhibit nonlinearities with the order $S = 30$, meaning that above their PA threshold, their luminescence intensity scales with the 30th power of the excitation intensity, similar to a 30-photon process. Thus, doubling the input power results in a staggering 10^4–10^6-fold increase in emission intensity. These extreme nonlinearities have been historically investigated and exploited in bulk, lanthanide-doped crystals (*e.g.*, in Pr^{3+}-doped $LaCl_3$ and $LaBr_3$ single crystals[1]) and fibers to develop new upconversion laser materials and infrared quantum counters. However, the application of PA has been limited by the large size and stringent requirements for observing PA in these materials (*e.g.*, high-quality crystals and cryogenic temperatures). Another characteristic feature of PA emission is its long luminescence rise time, which varies with pump power and excitation history (Fig. 1c).

A resurgence of interest in PA has been driven by the recent observation of room-temperature PA in nanoscale materials[2,3] and the corresponding advances in the synthesis,[2,4–6] heterostructuring,[3,5,7–9] modelling,[2,3,6,10–13] sensitization,[3,7–9,11,14] and biofunctionalization[15,16] of lanthanide-doped colloidal nanoparticles that exhibit PA. Scaling PA below 100 nm allows its extreme nonlinearity to be leveraged for applications in sub-diffraction imaging and sensing of temperature, forces, and analytes. In these applications, performance metrics such as spatial resolution and sensitivity are determined by the small size and high nonlinearity of the probe. The colloidal nature of

[a] *Institute of Low Temperature and Structure Research, Polish Academy of Sciences, ul. Okolna 2, 50-422 Wroclaw, Poland. E-mail: a.bednarkiewicz@intibs.pl*
[b] *Nanophotonics Group, Institute of Physics, Faculty of Physics, Astronomy and Informatics, Nicolaus Copernicus University in Toruń, 87-100 Toruń, ul. Grudziądzka 5, Poland*
[c] *Department of Chemistry, Oregon State University, Corvallis, Oregon 97331, USA*
[d] *Department of Mechanical Engineering, Columbia University, New York, NY, USA*
[e] *The Molecular Foundry, Lawrence Berkeley National Laboratory, Berkeley, California 94720, USA. E-mail: emchan@lbl.gov*

† Electronic supplementary information (ESI) available: Overview of PA in various lanthanide ions, comparison table of PA In nano- and micromaterials, comparison table of sub-diffraction imaging with PA nanoparticles. See DOI: https://doi.org/10.1039/d4cs00177j

PA nanoparticles also facilitates incorporation of these materials into biological environments and the solution-phase processing of high-density devices for optical storage, computing, and detection. A key advantage of these avalanching nanoparticles (ANPs), which are built upon decades of research into lanthanide-doped upconverting nanoparticles, is that they exhibit excellent photostability, narrowband absorption and emission, high biocompatibility, relatively low critical pump threshold, and extreme susceptibility to signals such as temperature, infrared light, and chemical environment.

This review surveys the recent developments in photon avalanching nanomaterials, with emphasis on their design, synthesis, characterization, and application. This review complements the canonical reviews on PA in bulk materials[17–19] to cover the surge in reports on PA nanomaterials within the past 5 years. Initially, we introduce the general principles, mechanism and key features of PA (Section 2) and its brief history in bulk materials (Section 3). Section 4 and Section 5 survey the recent developments in nanomaterials that exhibit PA and discuss their unique optical properties. Section 6 reviews the applications enabled by these PA nanomaterials. Finally, we offer a perspective on the future opportunities and challenges for research in the field of PA nanomaterials in Section 7. By providing a deep understanding of PA and its current state-of-the-art, we hope that this review will stimulate the further development of PA nanomaterials for photonics, biomedicine, sensing, computing, and other applications that would benefit from extreme nonlinearity.

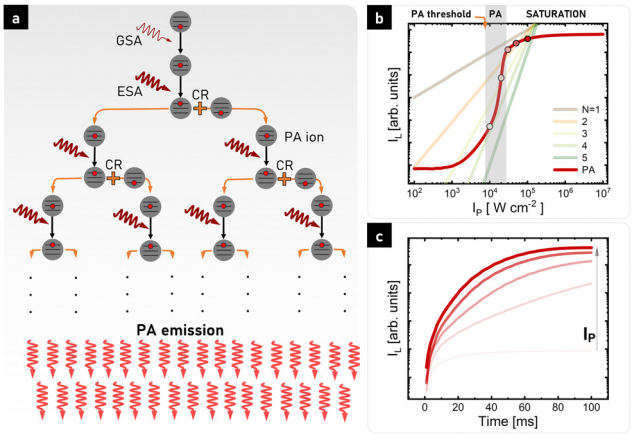

Fig. 1 'Chain reaction' mechanism of PA emission (a) and basic features of PA emission – pump power-dependent PA luminescence intensity (b) compared to linear (N = 1) and nonlinear (N = 2, 3, 4, 5) luminescence behaviour, as well as PA luminescence rise times upon switching on photoexcitation (c); curves in (c) correspond to circles in (b) of the respective shade of red colour.

Marcin Szalkowski

Marcin Szalkowski received his PhD in Biophysics in 2019 from Nicolaus Copernicus University in Toruń. His doctoral research focused on the application of plasmonically active materials in biosolar cells. In 2020–2022, he worked as a Postdoctoral Fellow in the group of Prof. Artur Bednarkiewicz at the Institute of Low Temperatures and Structure Research, PAS, in Wrocław, where he studied the optical properties of photon avalanching materials. Currently, he continues his research on plasmonics, microscopy techniques and photon avalanche in nanomaterials in the Nanophotonics Group headed by Prof. Sebastian Maćkowski at the Nicolaus Copernicus University in Toruń.

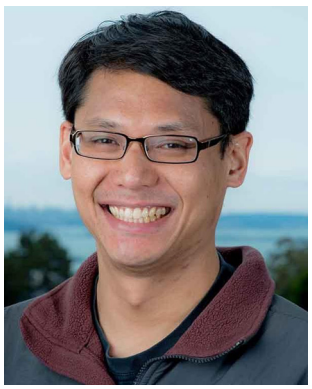

Emory M. Chan

Dr Emory Chan is a Career Staff Scientist at the Molecular Foundry, a U. S. Department of Energy nanoscience user facility at Lawrence Berkeley National Laboratory. Dr Chan's research interests include the combinatorial, high-throughput synthesis of nanomaterials with complex compositions, such as semiconductor nanoparticle heterostructures tailored for solid-state lighting and biological imaging. He also investigates nanomaterials that host complex energy transfer networks, such lanthanide-doped upconverting nanoparticles for lasing and super-resolution imaging. Towards this, Dr Chan has developed robotic workflows that increase the reproducibility and throughput of colloidal nanoparticle synthesis, while also enabling machine-learning guided experimentation.

Artur Bednarkiewicz

Professor Artur Bednarkiewicz works in the Institute of Low Temperature and Structure Research, Polish Academy of Sciences in Wroclaw, Poland. He is interested in physics, modeling, and spectroscopy of lanthanide-doped materials; developing novel materials, methods and optical instrumentation for imaging and sensing. His current interdisciplinary research focuses on optical nano(bio)spectroscopy, imaging, sensing; novel designs of lanthanide-doped nanoparticles and photon avalanche (bio)labels towards luminescence nanothermometry and biosensing; upconversion FRET (bio)sensing; reservoir computing.

2. Fundamentals of photon avalanche

2.1 Conventional Stokes and anti-Stokes luminescence

PA materials are intriguing because they do not follow the photophysical mechanisms of luminescence found in most of the known emitters, such as organic dyes and quantum dots. Conventional linear emitters exhibit the most basic form of Stokes emission, *i.e.* fluorescence, in which the GSA of excitation energy quanta ($h\nu_{EXC}$) is followed by the emission of a photon ($h\nu_{EMI}$) whose energy is lower compared to the incident one ($h\nu_{EXC} > h\nu_{EMI}$). This process is relatively fast, with timescale of 10^{-10}–10^{-8} s. However, in selected compounds, for example, organic (collagens and lipids) and inorganic crystals, nonlinear anti-Stokes phenomena ($h\nu_{EXC} < h\nu_{EMI}$), such as second-harmonic generation (SHG) and third-harmonic generation (THG) (Fig. 2a), can be observed, where the input frequency (ω) is, respectively, doubled (2ω) or tripled (3ω), resulting from the higher order susceptibility ($\chi^{(2)}$ and $\chi^{(3)}$) of the medium. The observation of SHG and THG became possible by the invention of high-intensity, polarized and coherent light sources, lasers. In this case, an electric field with amplitude $E(\omega)$ traveling through a medium exhibiting nonlinear susceptibility tensor, $\chi^{(2)}$, can be described in terms of polarization at double frequency, $P(2\omega) = \epsilon_0\chi^{(2)}E^2(\omega)$. However, besides a few recently published

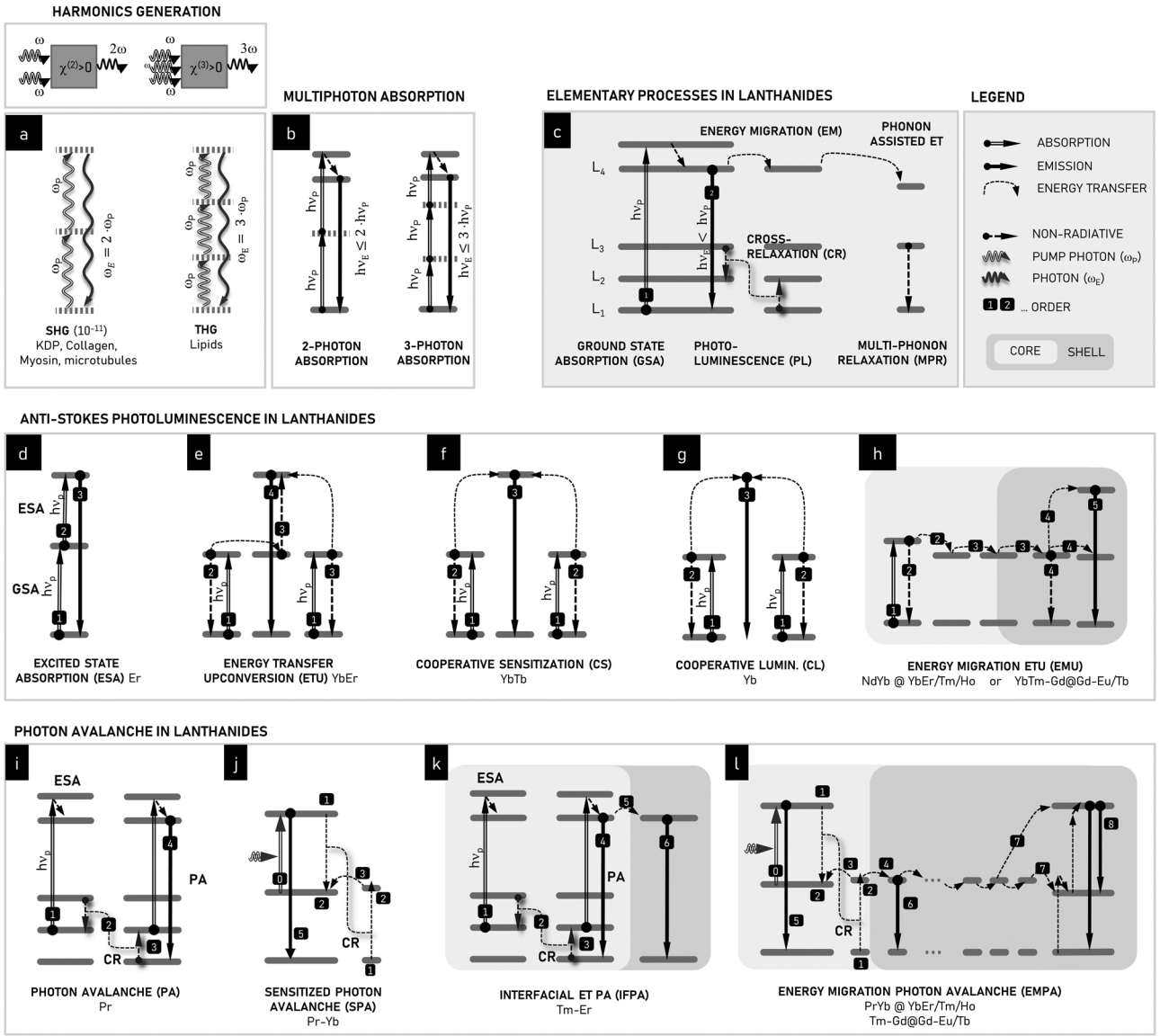

Fig. 2 Schematic ET processes leading to anti-Stokes emission in Ln^{3+} ions compared to nonlinear optical processes such as second and third harmonics generation (a) and 2- and 3-photon absorption (b). In lanthanides, numerous energy transfer (ET) processes may occur (c): ground-state absorption (GSA), Stokes photoluminescence (PL), energy migration (EM), cross-relaxation (CR), phonon-assisted ET, and multi-phonon relaxation (MPR), Numerous anti-Stokes processes can be found in lanthanides: (d) GSA + excited-state absorption (ESA), (e) energy transfer upconversion (ETU), (f) cooperative sensitization (CS), (g) cooperative luminescence (CL), (h) energy migration ETU (EMU), (i) photon avalanche (PA), (j) sensitized photon avalanche (SPA), (k) inter-facial energy transfer photon avalanche (IFPA) and (l) energy migration-assisted PA (EMPA). EMU, IFPA and EMPA are only possible in non-trivially distributed lanthanide ions using core–shell compositional architectures. All lanthanides denote the 3+ ions.

reports,[20] the probability of this process is rather low and can only be observed in non-centrosymmetric crystals under precise phase matching conditions between the laser beam and crystallographic axes of the crystal.[21] Another type of anti-Stokes emission can occur following a 2- or 3-photon absorption process (Fig. 2b), in which the excited state of the emitter is reached *via* the simultaneous absorption of 2 or 3 photons, respectively. While 2- or 3-photon microscopy is feasible and used to enhance the imaging depth and spatial confinement, similar to the previous processes, these mechanisms require excitation with high-power, ultrafast pulsed lasers.

2.2 Upconversion in lanthanide ions

PA is observed in lanthanide ions because they can host anti-Stokes mechanisms that are not accessible to other fluorophores. The forbidden nature of the f–f transitions in trivalent lanthanide ions and ladder-like arrangement of energy levels result in long-lived metastable excited states through which ions can be repeatedly and sequentially excited to high energies. This efficient upconversion in the rich energy level structure of lanthanides is further facilitated in solid state materials by the fact that neighbouring lanthanide ions can interact and transfer energy amongst themselves in processes (Fig. 2c) such as (i) resonant energy migration (EM), (ii) phonon-assisted energy transfer (PAET), and (iii) cross-relaxation (CR). In efficient upconverting materials, these photon excitation and energy transfer (ET) processes outcompete processes that quench the excited states through non-radiatively relaxation, including multiphonon relaxation (MPR), energy quenching on crystal defects, and ET to surface ligands and solvent molecules. CR and MPR are typically considered parasite processes, which limit the brightness of lanthanides. CR results in concentration quenching, preventing the use of higher amounts of emitting lanthanide centers. Alternatively, MPR deactivates excited states non-radiatively to lower intermediate levels or to the ground state, which limits the emission quantum yield significantly. Thus, upconversion in lanthanide-doped materials is the result of a complex, nonlinear network of photophysical interactions,[22] involving all the processes summarized in Fig. 2c.

Most upconversion applications utilizing lanthanide ions follow the two-photon upconversion processes shown schematically in Fig. 2d and e. The upconversion process in Fig. 2d involves the sequential absorption of two photons by the same ion, *i.e.*, the GSA between the ground energy level and a metastable intermediate level, followed by ESA from the intermediate level to a higher emitting state. A variant of this upconversion scheme, known as ET upconversion (ETU) or APTE (addition de photon par transferts d'energie), utilizes ET to sensitize absorption with a second lanthanide ion such as Yb^{3+} (Fig. 2e). In the case of both ESA and ETU, it is preferable if the energy of the photon absorption transitions is equal to the energy of the excitation radiation. However, these phenomena may still be observed with a limited amount of energy mismatch with the assistance of phonons, albeit with lower transition probabilities and efficiencies. Thus, as a general rule, resonant photon absorption is desirable for most upconversion applications. The other mechanisms include the much weaker cooperative sensitization (CS) and cooperative luminescence (CL). By exploiting core–shell heterostructured nanomaterials, where the core and the shell are individually optimized and doped with different Ln^{3+} ions, the combination of EM and ETU has opened new possibilities, such as UC under the more biocompatible 800 nm excitation and multicolour emission.[23–26]

Stemming from the basic ET processes found in Ln^{3+} ions (Fig. 2c) and conventional upconversion mechanisms (Fig. 2d–h) in homogenously and heterogeneously doped nanomaterials, various PA mechanisms can be derived, such as the conventional single-dopant PA (Fig. 2i – PA) and sensitized PA (Fig. 2j – SPA), which are the underlying mechanisms for interfacial ET-based (Fig. 2k – IFPA) and energy migration-based (Fig. 2l – EMPA) photon avalanche emission. The major difference between the conventional non-linear (SHG/THG, 2/3PhAbs) or upconversion processes (*i.e.*, ETU, ESA, CS, and CL) and photon avalanche (*i.e.*, PA, SPA, IFPA, and EMPA) is that PA exploits a combination of inefficient GSA with efficient ESA and purposefully augmented CR processes, whose coexistence enables unique PA features to be achieved, but requires a paradigm change in materials design.

2.3 Mechanism of photon avalanching

The mechanism of PA in lanthanide ions (shown in Fig. 2i and 3) is distinct from the other non-linear or upconversion processes described in Fig. 2 because PA specifically occurs when GSA is extremely non-resonant (Fig. 3, process 1′), while the ESA remains resonant and efficient (Fig. 3, process 2). In a

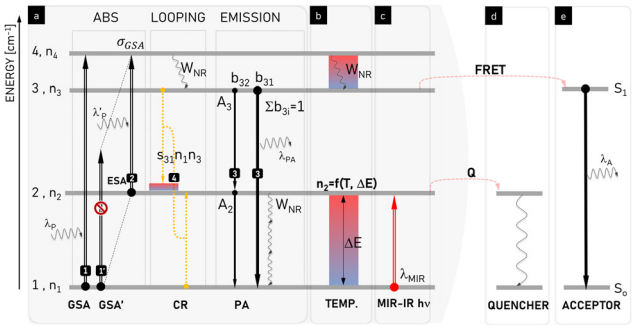

Fig. 3 Schematic presentation and explanation of the physical processes involved in photon avalanche emission. Phenomena leading to (a) pure PA, which can be modulated by (b) temperature, (c) illumination with medium-infrared (MIR) photons, and (d) presence of an energy quencher or (e) acceptor. At increased temperature (b) or in the presence of MIR photons (c), the population of the starting level (n_2) increases, which modifies PA performance. Temperature may be additionally involved in temperature-sensitive phonon-assisted ET (*e.g.* cross-relaxation $s_{31}(T)$) and multi-phonon relaxation ($W_{NR}(T)$) responsible for energy looping in the system. Because the energy quencher Q (d) or acceptor (e) compete for energy stored in level 2 and 3, the cross-relaxation-based energy looping (4) becomes compromised and the intermediate starting level population (n_2) gets smaller. Thus the ESA (2) is hindered, which overall suppresses the PA intensity and increases the PA threshold. $\lambda_P/\lambda_{PA}/\lambda_A$ denotes the emission wavelength of the pump/photon avalanche/acceptor, s_{31} defines the temperature-dependent looping rate, W_{NR} denotes the temperature-dependent rate of multiphonon relaxation, b_{3i} is the host-dependent branching ratio of emission between levels 3 and i_{th}, and ΔE is energy gap between levels 1 and 2.

conventional upconversion process in which GSA is followed by ESA, slow GSA will limit the overall rate of upconversion given that it will not be able to populate the intermediate level (n_2) sufficiently to enable appreciable ESA. However, the unique mechanism of PA circumvents this GSA bottleneck (which occurs due to weak side-band phonon-assisted ground-state absorption) through the use of a type of ET known as cross-relaxation (CR). Here, in the rare circumstance that an Ln^{3+} ion is excited *via* ESA, it transfers some of its energy to a neighbouring Ln^{3+} ion in its ground state, resulting in two Ln^{3+} ions in their intermediate states. Thus, CR can double the population of the intermediate level, n_2, in every iteration of the ESA+CR "energy looping" process (3; 1) → (2; 2). Subsequently, this enhanced n_2 population becomes responsible for the enhanced rate of ESA, and the material becomes less transparent to the PA photoexcitation wavelength (λ_P). Thus, CR bypasses the need for GSA. The enhanced ESA results in increased CR, resulting in a positive feedback loop in which repeated cycles of ESA+CR looping result in the exponential amplification of the population of the n_2 and other excited states. This 'explosion' of population gives rise to a corresponding 'avalanche' of photons emitted from highly excited states, thus giving rise to the PA nomenclature. In short, the mechanism of PA is defined by three main features, as follows: (1) non-resonant GSA, which initially limits luminescence, (2) resonant ESA, and (3) CR, which couples with ESA in a positive feedback loop to non-linearly populate the intermediate levels from which ESA originates.

2.4 Prerequisites for observing photon avalanching

Although the mechanistic features listed above are necessary for PA, they are not sufficient to observe the highly nonlinear optical responses characteristic of PA. A common rule-of-thumb for achieving PA is that the ratio of resonant ESA cross section $\sigma_{ESA}(\lambda_P)$ to non-resonant GSA cross section $\sigma_{GSA}(\lambda_P)$ at a given pump wavelength λ_P follows the condition:

$$\beta = \frac{\sigma_{ESA}(\lambda_P)}{\sigma_{GSA}(\lambda_P)} > 10\,000 \qquad (2\text{-}1)$$

To date, although there is no consensus on a strict β parameter value, β smaller than 10 000 is typically known as energy looping rather than PA. The primary distinction between energy looping and PA is that PA exhibits a much more nonlinear optical response at the excitation power threshold at which the populations and luminescence suddenly increase. Furthermore, although no clear definitions of avalanche and looping processes exist, based on the present literature, $S \sim 10$ seems to be a commonly observed non-linearity that separates the looping ($3 < S < 10$) regime from the avalanching ($S \geq 10$) regime. A β parameter larger than 10 000 is commonly assumed to be required, but not a sufficient condition to achieve PA. The second condition is an efficient CR process to multiply the intermediate manifold population, which then enhances the efficiency of ESA. Due to the increased concentration of doping ions, the cross relaxation process between neighbouring ions is competitive with the luminescence in the PA regime, ultimately leading to the avalanche of photons, *i.e.*, the release of energy accumulated in the system during the ESA+CR looping. Above the PA threshold (I_{TH}), rapid luminescence intensity (I_L) growth is observed in response to a minute increase in the pump intensity (I_P). This pump power-dependent relationship is described by a simple power law,[27] as follows:

$$I_L \sim (I_P/I_{TH})^S \qquad (2\text{-}2)$$

which remains valid from the PA threshold up to the saturation region, where efficient ESA+CR keeps the population of intermediate looping level high, and thus S becomes reduced to $S = 1$. In PA, the nonlinearity S values in eqn (2-2) are larger than 10, and values of up to 12.6 (for Tm^{3+} in $LiYF_4$),[6] 31 (for Tm^{3+} in $NaYF_4$),[2] 46 (for $Pr^{3+}Yb^{3+}$–$Yb^{3+}Tm^{3+}$ co-doped in $NaYF_4$)[3] or even above 500 (for Tm^{3+} in $NaLuF_4$)[28] have been experimentally evidenced in nanomaterials at room temperature. It is important to mention here that the population of the emitting (n_3) and/or looping (n_2) levels can be easily perturbed by exogenous fields, conditions, quenching centers, defects or molecules. For example, temperature (Fig. 3b) or medium IR photons (Fig. 3c) may augment the seed looping level population, and thus decrease the PA threshold compared to the pristine condition. Independently, quenching of the looping (Fig. 3d) and/or the emitting (Fig. 3e) levels should increase the PA threshold and decrease the observed nonlinearities. Due to highly non-linear behaviour of PA emission stemming from the positive looping, these external factors may significantly modify the luminescence of PA materials, and providing the opportunity to utilize PA materials for sensing applications, as we discuss in subsequent chapters.

2.5 Criteria for confirming photon avalanching

The ability to extract critical parameters from power- and time-dependent luminescence data allows one to objectively determine whether PA is actually occurring. In its most rigorous definition, one can classify a material as undergoing PA when all the following criteria are satisfied simultaneously:

(i) Although measuring ESA directly is challenging, the ESA/GSA ratio should exceed $\beta > 10^4$. Given that the ESA and GSA are wavelength dependent, the ability to tune the laser wavelength to maximize the β value is critical and a non-optimal β may be prohibitive to get PA emission or reduce its PA character.

(ii) There are no rigid rules about nonlinearity and PA gain, but the values of PA non-linearity of $S \geq 10$ and PA gain of $\Delta_{AV} \geq 100$ (eqn (2-7)), respectively, are typically considered to indicate PA. Materials that do not meet these criteria but exhibit the same mechanism are considered to be undergoing energy looping. Measuring these values experimentally in a reliable and operator-to-operator variation free manner is often difficult, and thus some hints are presented in Section 2.7. Also, some computer algorithms have been developed to automatically derive S, I_{TH} and Δ_{AV}.[6]

(iii) A significant slowing down of the rise times at the PA threshold, and their shortening as excitation intensities are increased above the threshold.

2.6 Modelling of PA with rate equations

Numerical modelling of lanthanide photo physics proved critical in the discovery of PA in nanomaterials. In fact, PA in nanomaterials and its utility in sub-diffraction imaging[29] were predicted with rate equation modelling several years before experimental realization. The absorption and luminescence processes of the simple system presented in Fig. 3a can be described by the following general rate equations:

$$\frac{dn_1}{dt} = -I_{GSA}\sigma_{GSA}n_1 - s_{31}n_1n_3 + b_{31}A_3n_3 + (W_{NR} + A_2)\cdot n_2 \quad (2\text{-}3)$$

$$\frac{dn_2}{dt} = -I_{ESA}\sigma_{ESA}n_2 + 2s_{31}n_1n_3 + b_{32}A_3n_3 - (W_{NR} + A_2)\cdot n_2 \quad (2\text{-}4)$$

$$\frac{dn_3}{dt} = 1 - \frac{dn_1}{dt} - \frac{dn_2}{dt} \quad (2\text{-}5)$$

where $\sum_{i=1..3}\frac{dn_i}{dt} = 1$, and I_{GSA}, σ_{GSA}, denote the pump intensity and the absorption cross section under GSA, while I_{ESA}, σ_{ESA} denote the pump intensity and absorption cross section under ESA; s_{31},W_{NR} denote the CR rate between level 3 and 1, b_{ai} denotes the branching ratio between states $\left(\sum_{i=1,2} b_{3i} = 1\right)$, and A_a is the radiative rate from level a (a = 2 and 3), respectively. In the steady state, $\frac{dn_i}{dt} = 0$ occurs (for all the levels), which enables the derivation of the n_3 population the luminescence intensity (A_3n_3) as functions of the excitation power density. In the case of PA, analytically solving the set of rate equations may be too complex or even impossible, and thus numerical methods are used.

Due to the inherent nature of PA emission, pump power-dependent luminescence rise times of up to hundreds of milliseconds ($\tau_R \sim$ 100–1000 ms) have been observed (Fig. 4).

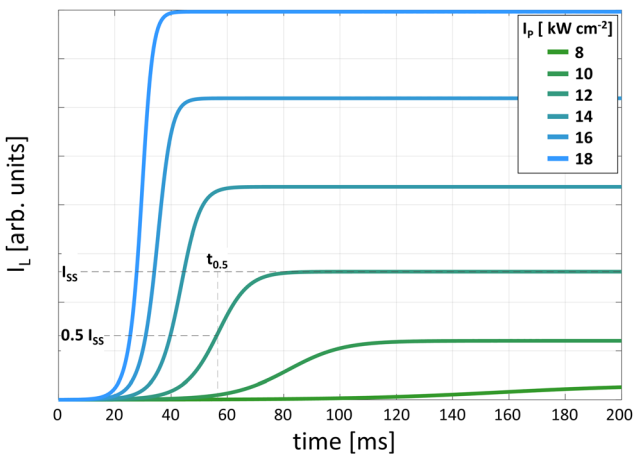

Fig. 4 DRE-simulated kinetic profiles of luminescence intensity rise for different excitation intensities. The 50% rise time ($t_{0.5}$) is shown as the time at which the intensity reaches half of the steady state intensity (I_{SS}).

Under sufficiently long excitation pulses ($t > \tau_R$), these kinetic profiles of the PA(t) luminescence intensities enable the extraction of the steady-state luminescence intensity (I_{SS}) and rise time of the luminescence intensity. The inverse of the experimental luminescence decay (τ_{exp}) equals the sum of all radiative (k_R) and nonradiative (k_{NR}) rates, as follows:

$$\frac{1}{\tau_{exp}} = k_R + k_{NR} \quad (2\text{-}6)$$

τ_{exp} depends on the material parameters (*i.e.* host, dopant type and concentration, and size of nanoparticles), but in principle, the Stokes emission mode should not depend on the experimental conditions (*e.g.* excitation power). In the anti-Stokes emission model, these luminescence lifetimes demonstrate pump power dependence, owing to the energy stored in the long-lived excited states, which tend to recharge the emptied emitting levels.[22,30] Alternatively, in the PA process, the rise time is not only dependent on the host and dopant, but also strongly related to the excitation power density. In particular, the emission intensity rise becomes very slow close to the PA threshold. To characterize this slow-down or rise times and evaluate PA, one may use rise times extracted from exponential fits or other critical time points such as $t_{0.5}$ and $t_{0.9}$, which indicate the time necessary to reach 50% or 90% of the steady state intensity, respectively, with $I(t_X) = x{\cdot}I_{SS}$. Below the PA pump power threshold the rise times are short given that the emitting level population occurs due to sequential ESA.[3] As soon as the pump power approaches the PA threshold, the intermediate level population enables more efficient ESA and energy looping starts to dominate. A critical slowing down of the rise time is found within the PA regime ($I_{TH} \leq I_P \leq I_{SAT}$), where I_P, I_{TH} and I_{SAT} denote the excitation intensity, excitation intensity at the PA threshold and excitation intensity at the emission saturation, respectively. However, there is typically some ambiguity in establishing PA parameters such as the pump threshold, slope, and saturation region. Below, we recommend methods to derive these factors and regions in a reproducible manner to facilitate cross-lab comparison.

Differential rate equation (DRE) modelling can be useful to both quantitatively and qualitatively understand the particular PA mechanism (*e.g.* the role and mechanism of Yb^{3+} sensitization of Pr^{3+} avalanching),[3,11] and likewise understand some trends in the PA thresholds, slopes or emission quantum yields that occur in response to a variation in the critical PA parameters (*e.g.* the rates of CR, radiative, non-radiative or absorption cross-section).[2,6,11] Moreover, DRE's can be equipped with terms corresponding to additional physical phenomena such as additional ET and relaxations, and has been proven to be an important tool, beside experimental evidence, helping to understand way PA becomes modified in response to a variation in temperature[10] or the underlying quenching mechanism affecting the looping and emitting levels.[12]

2.7 Extraction of key physical parameters of PA from experimental and computational data

Essential PA features can be extracted from the kinetic profiles of PA luminescence intensity ($I_L(t, I_P)$) *vs.* pump power, as

shown in Fig. 4. These critical parameters include the steady-state PA emission intensity ($I_{SS} = I_L(\infty)$) and rise time measured as $t_{0.5}$ (defined as $I_L(t_f, I_P) = f \cdot I_{SS}(I_P) = f \cdot I_L(\infty, I_P)$, where $f \in \langle 0; 1 \rangle$, with the typical $f = 0.5$), as shown in Fig. 5, respectively. These standardized methods for the evaluation of the PA spectral, intensity and kinetics should be adopted to enable quantitative comparisons among materials, dopants and labs.

The rise times (Fig. 4 and 5c) are initially in the microsecond range (very short), then significantly prolong to tens or hundreds of milliseconds (close to the PA threshold), and finally shorten again due to the saturation process with an increase in the pumping intensity.[2,29]

By plotting the pump intensity (I_P)-dependent steady-state PA emission (I_{SS}), one may derive further parameters that characterize the PA emission, such as the pump intensity at which PA occurs (PA threshold, I_{TH}) or saturates (I_{SAT}) and the slope (S) of the power dependence curve (Fig. 5a and b). One may also calculate a pump power-dependent PA gain, which is defined by Lee *et al.*,[2] as follows:

$$\Delta_{AV}(I_P) = \frac{I_L(2 \cdot I_P)}{I_L(I_P)} \quad (2\text{-}7)$$

and shown in Fig. 5d. These quantities are not straightforward to extract manually, while I_{TH}, I_{SAT} and S may be supported by automatic analysis algorithms,[6] and qualitative relations between these quantities (*e.g.* orange lines in Fig. 5, plotted for the cyan curve for $[Tm^{3+}] = 15\%$) may be established. To avoid ambiguity

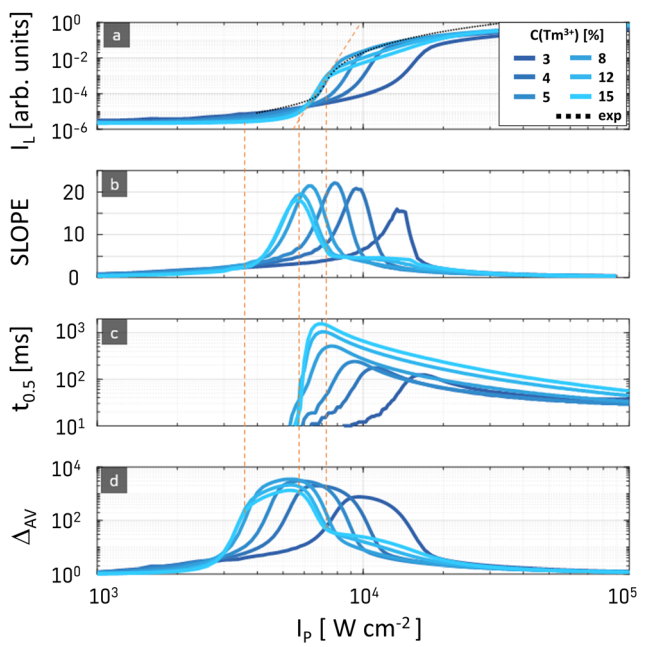

Fig. 5 Characteristic properties of the PA phenomenon: excitation power-dependent (a) steady-state – $I_L(I_P)$, (b) nonlinearities (S), (c) risetime – $t_{0.5}(I_P)$ and (d) PA gain. The dotted line on (a) represents the experimental values for 8%Tm^{3+}-doped $NaYF_4$ avalanching NPs,[2] while the blue lines are generated with the DRE model for an increasing Tm^{3+} concentration developed in ref. 2 (b)–(d) data have been derived from (a) using algorithms from ref. 6 orange dashed lines show correspondence between the (a)–(d) plots and account for the light blue data line (15%Tm^{3+}).

in the manual determination of the threshold and the slopes, some phenomenological observations can be employed. For example, I_{TH} can be correlated with the pump power at which the maximum $S(I_P)$ is found, while the saturation begins at the pump power where $S(I_P)$ reaches a plateau and $t_{0.5}$ begins to monotonically decrease.

One of the most distinctive and unintuitive features of PA is that near the PA pump power threshold, the PA rise time $t_{0.5}$ gets significantly longer, as long as milliseconds or even seconds. These long rise times are useful both for confirming the presence of PA, and also as critical parameters for evaluating PA materials. These long rise times can be disadvantageous, *e.g.*, typically being viewed as detrimental for achieving fast frame rates during imaging.[3] Alternatively, these long rise times allows one to extract 'pure avalanche photons' in the time domain,[29] *i.e.*, the photons that have their origin in the photon avalanche phenomenon and not from the linear absorption and emission ($I_P \leq I_{TH}$) or from saturated emission ($I_{SAT} \leq I_P$). These "pure" avalanche photons, I_{PA}, may be quantified by the $I_{PA} = I(t_2) - I(t_1)$ difference ($t_1 < t_2$), where t_1 and t_2 ($0 < t_1 < t_2$) are arbitrarily selected to discriminate long rise times photons, corresponding to PA, from the faster ones, which can be ascribed to the conventional luminescence.

More precisely, t_1 denotes the time point when steady-state emission is obtained using an excitation intensity close to the saturation region, significantly exceeding the PA pumping threshold. Alternatively, t_2 is the shortest time required to observe steady-state emission from the system excited with the power close to the PA threshold. The "pure" PA photons is a term that may be important for applications where only most nonlinear behaviour is critical, such as in photon avalanche single-beam super-resolution imaging (PASSI).[29]

2.8 Photon avalanching operating regimes

Depending on the excitation power density, three main operating regimes defined the by relations between the efficiencies of the involved processes can be found, as depicted in Fig. 6a–d. Below the PA threshold (Fig. 6b), photoexcitation results in an increase in the population of the n_2 state due to the presence of inefficient GSA.[17] At this point, the energy of the pump light is mainly stored by the system in the increasing population of the intermediate level, spreading thorough the network of Ln^{3+} ions within the host crystal structure with each looping cycle (Fig. 7). However, at this stage, other processes, such as emission, which can be considered a parasitic effect from this perspective, are balancing CRs and one can observe a linear dependence between the excitation and emission intensities ($S = 1$). With a further increase in the excitation intensity exceeding the PA threshold (Fig. 6c), the emission intensity rapidly increases. This is the power regime where a highly nonlinear relationship can be observed between the pumping power density and the resulting output, and the S parameter reaches the highest value. At the atomic level in the avalanching system, the ESA absorption becomes more efficient due to the increased number of ions in the intermediate energy level, and until the saturation regime, the CRs remain effective, leading to a further increase in this population.

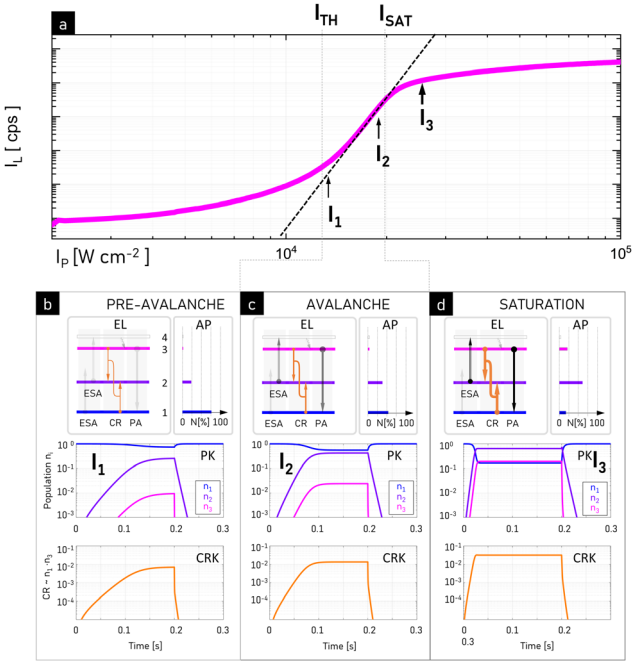

Fig. 6 Pump power-dependent PA luminescence intensity and population dynamics. (a) Typical S-shape relationship between pump (I_P) and luminescence (I_L) intensities. (b)–(d) Simulated kinetics of the population of ground (n_1), intermediate (n_2) and emitting (n_3) levels as well as cross-relaxation strength CR·n_1·n_2 in pre-avalanche (b), avalanche (c) and saturation (d) regions.

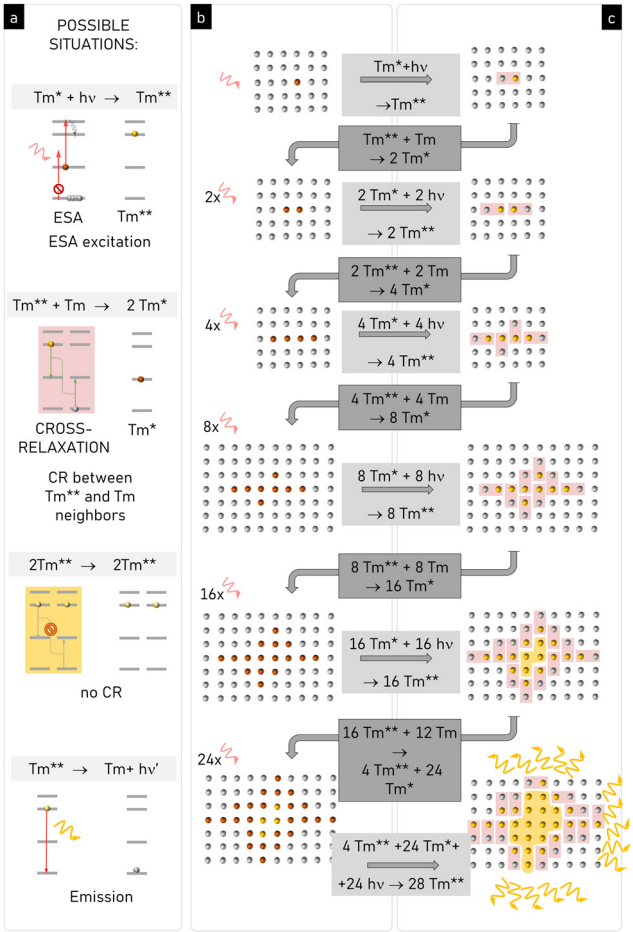

Fig. 7 Mechanistic and time-lapse-like explanation of PA emission. The occurrence of several elementary situations is possible in the avalanching system, including the ESA excitation, CR between the ions, local saturation of the system with emitting state ions and, finally, emission (a). In the initial steps of the avalanche mechanism, the single ion is excited by non-GSA-resonant but ESA-resonant photons and undergoes CR (c) with neighbouring ions to double the population of the starting level (b). Upon ESA photoexcitation, steps (b) and (c) are repeated, and the population of the starting level doubles on each loop iteration, as long as the CR rate is much higher than the photon emission or non-radiative depopulation. Red boxes symbolize the pairs of ions (ground state and excited state energy levels) taking a part in the single CR event. Yellow boxes denotes ions in the excited state, which are not capable of cross-relaxing energy with their ground-state neighbours anymore and tend to emit photons. By default, all lanthanide symbols are 3+ ions.

However, certain domains of ions in the emitting level are surrounded by neighbours also excited to the emitting level, making the emission the only possible way to relax the energy. Importantly, after the emission of photons, this ground state ion may be immediately promoted to the intermediate level by the CR with one of the neighbours in the emitting energy level, and then both of them can turn back to the emitting level after capturing the ESA-resonant excitation light. However, a further increase in the illumination power density gradually limits the number of the ground-state ions in the host material, limiting further CRs (Fig. 6d). The dominant process is now the release of accumulated energy in the form of photons (Fig. 6, bottom row). In the power dependence measurements, a linear dependence between the excitation and emission intensities is observed again at this stage (Fig. 6a) because a balance among ESA, CR, k_{MPR} and luminescence processes is reached. Based on the DRE modelling of the PA Tm^{3+} emission, Fig. 6b–d show the importance of various processes (shown schematically by arrow thickness in energy levels (EL) insets), the average population (AP), as well as the population kinetics (PK) of the ground (n_1), intermediate (n_2) and emitting (n_3) levels, and the contribution of the CR process kinetics (CRK) to the whole PA process. A mechanistic and time-lap like explanation for PA process is schematically presented in Fig. 7.

2.9 Effect of radiative and nonradiative rates on PA

Rate equation models are useful for understanding the design rules for PA materials because they allow the simulation of how the PA parameters will respond to variations in materials properties. For example, in the case of the model depicted in Fig. 3 and described by eqn (2-3)–(2-5), the concentration of dopants, and thus the looping strength may be related to the s_{31} parameter. Although strong CR is indispensable for efficient PA emission, this process may simultaneously reduce the luminescence intensity. Therefore, by fixing all the other parameters, one may qualitatively study how the concentration of the dopant impacts the PA behavior. Similarly, the non-radiative rate, k_{NR}, is related to the host material. In general, the non-radiative quenching of level 2 is undesirable, but non-radiative transitions are needed to bridge the energy gaps between levels

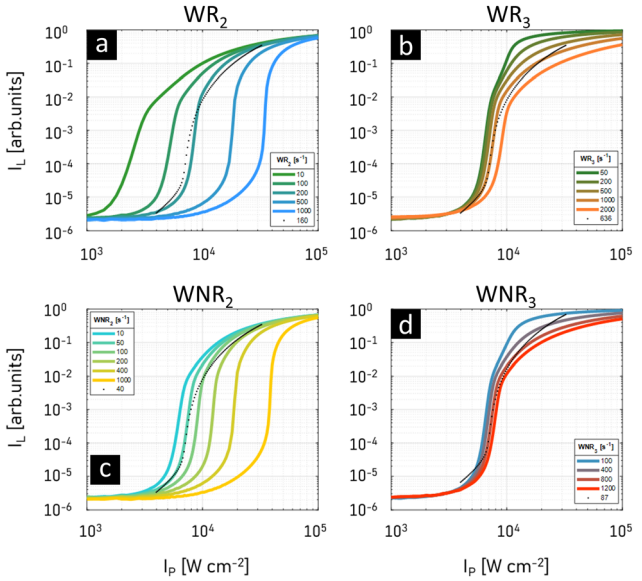

Fig. 8 Simulations of pump power-dependent PA emission intensity of $NaYF_4$:8%Tm^{3+}: materials in response to the radiative rates of level 2 (a) and 3 (b) (WR_2 and WR_3, correspondingly), as well as the impact of non-radiative rates for levels 2 (c) and 3 (d) (WNR_2 and WNR_3 rates, respectively). Simulations include the pristine rates found for the original $NaYF_4$: 8%Tm^{3+} material (experimental data are shown as black dots), while varying respective parameters around original values.[6]

4 and 3. Under real conditions (not included in the rate equations), these phonons are also required to bridge imperfect energy matches between cross-relaxing energy levels (*i.e.* when $|E_3 - E_2| \neq |E_2 - E_1|$).

Fig. 8 semi-quantitatively demonstrates the impact of the radiative and non-radiative rates of the 2nd and 3rd levels in the simplified scheme of an exemplary Tm^{3+} PA material on its power dependence characteristics. It presents the significantly different impact of the dynamics of both levels on the PA performance and its main parameters. In particular, the increasing radiative and non-radiative rates of the 2nd level (the intermediate level during PA) clearly shift the power dependence curve (and the values of the key parameters I_{TH} and I_{SAT}) toward higher powers (Fig. 8a and c).[6] A much smaller trend can be observed in the case of the corresponding rates of the 3rd level (the emitting level), as shown in Fig. 8b and d.

3. Paradigm shift in designing luminescent materials for PA

3.1 Historical context

To put recent advances in PA nanomaterials into context and demonstrate how the theoretical concepts introduced in the previous section have been applied in real materials, we first discuss the development of PA in bulk materials. The history of PA emission dates back to 1979, when Jay S. Chivian *et al.* unexpectedly discovered unusual nonlinear luminescence in $LaCl_3$ and $LaBr_3$ crystals doped with Pr^{3+} (ref. 1) when excited with a green continuous-wave dye laser matching the $^3H_5 \rightarrow {}^3P_1$ ESA transition in Pr^{3+}. Above a critical pump power threshold (1–12 W cm^{-2}) at temperatures in the range of 20–300 K, the Pr^{3+} luminescence increased rapidly by two orders of magnitude, which was the first observation of avalanching. Notably, above the PA threshold, the laser extinction increased dramatically although the bulk crystal was transparent to the laser at sub-threshold excitation powers.

The discovery of PA stimulated researchers to study different materials from this unconventional point of view, inducing further interest and development of infrared quantum counter detectors[1,31] and becoming an impulse for the advancement of upconversion lasers.[32–36] In addition to Pr^{3+}-doped $LaCl_3$, PA was obtained with other quantum counters such as $LaBr_3$:Sm^{3+},[37] and $CeCl_3$:Nd^{3+}.[38] Other early observations of the PA phenomenon were also reported for bulk materials such as $LiYF_4$:Nd^{3+},[19,32,39] YAG:Tm^{3+},[40] ZrF_4–BaF_2–LaF_3–AlF_3–NaF (ZBLAN):Er^{3+},[41] YAG:Ho^{3+} (ref. 42) and ZBLAN co-doped with Yb^{3+} and Pr^{3+}.[43] PA was also investigated in optical fiber materials, especially in ZBLAN cores doped with Tm^{3+} (ref. 44) as well as with Er^{3+} (ref. 45) or co-doped with Yb^{3+} and Pr^{3+}.[46] ZBLAN glasses and $YAlO_3$ doped with Ho^{3+} were also studied as PA materials.[42,47] PA has been reported for YAG waveguides doped with Tm^{3+} (ref. 17 and 48) and BIGaZYTZr glass doped with Tm^{3+},[49] and for many other materials doped with thulium ions, such as $YAlO_3$,[50] $Cs_2NaGdCl_6$,[51] LaF_3,[52] Y_2O_3,[53] Y_2SiO_5,[54] KYF_4,[55] and CdF_2.[56] Moreover, $LiYF_4$ was identified as a favourable material for hosting PA due to its low phonon energy. Doping this host with Tm^{3+},[57] as well as with Nd^{3+},[32] Er^{3+} (ref. 58) or Ho^{3+} (ref. 42 and 59) has been shown to provide suitable conditions to obtain PA. Co-doping materials with a second ion such as Yb^{3+} was beneficial to obtain the PA phenomenon. In these instances, the Yb^{3+} ions act as a sensitizer,[46] enabling the pumping of the emitting states of the activators *via* ETU, and take a part in energy cross-relaxation processes, which is known to be crucial for the energy looping and PA mechanism.

An overview of the early work on PA, which was practically limited to bulk crystals, glasses, fibers and ceramics, can be found in a few early review articles.[17–19,48] However, despite these successful demonstrations, PA remained a scientific curiosity rather than a mainstream research area, as can be concluded based on several publications from a given year reporting investigations of PA in hosts doped with various Ln^{3+} ions (Fig. 9). After the first decade since the groundbreaking experiments

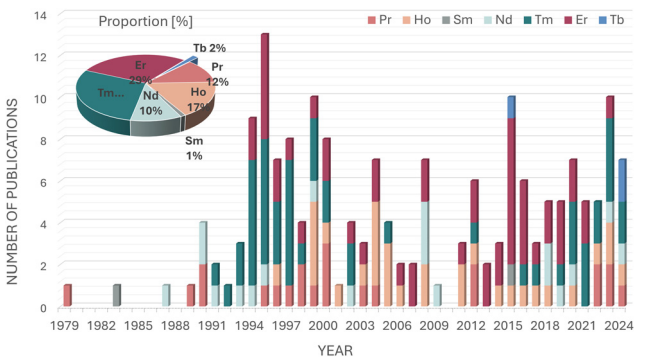

Fig. 9 Historical perspective on the PA emission (WebofScience.com database, update 10.07.2024).

revealing this new phenomenon, only a few new reports were published. In the next few decades, due to trials on utilizing PA mechanisms to develop new possibilities in the field of laser materials, broadened studies of this subject were performed in several research groups, resulting in over ten new papers per year and leading to a much better understanding of the details of this phenomenon, mainly based on Tm^{3+}-, Er^{3+}- or Nd^{3+}-doped host materials. Nevertheless, the rather specific conditions required to observe PA, often limited to low temperatures, even in bulk materials, have limited the development of this topic, especially compared to the number of publications related to the more general issue of upconversion in lanthanides.

3.2 Materials considerations for PA

3.2.1 Host material. For efficient upconversion luminescence, the selection of the host crystal material is essential, which will be even more critical for PA emission. The host determines the local crystal field and chemical environment around the active dopants, the distance between them, the relative spatial position and coordination numbers, and the type of anions around them. Moreover, the crystal fields produced by the host materials promote the f–f electronic transitions within the lanthanide ions by perturbing the 4f wavefunction. Therefore, the variation in the crystal structure of the host materials has significant influence on the optical properties of nanomaterials. The key parameter for the characterization of the host lattice is an optimal (usually low) phonon energy, which is related to the lattice vibration in crystals. The absence of high energy phonons limits the undesired nonradiative MPR of emitting levels, and thus maximizes the probability of radiative processes. Alternatively, the contribution of the phonons present in the host material may have in some systems a positive impact on the upconversion efficiency, given that the excited states can also be populated *via* phonon-assisted ET, which accounts for any energy mismatch. In this case, the higher the phonon energy, the easier it is to populate the excited state of lanthanide ions, and therefore the proper balance of the phonon modes available in the crystal lattice should be achieved.

Changing the host lattice and doping ion concentration allows the design of nanoparticles with predetermined properties. Many types of materials have been studied as hosts for the upconversion process between lanthanide ions including phosphates,[60] vanadates,[61,62] sulfides,[63] borates,[64–66] oxides[67] and fluorides. Among the available types of materials, fluorides, $ALnF_x$ (A = alkali metal, Ln = lanthanide), such as $NaLnF_4$ and $KLnF_4$, and LnF_3, CaF_2, and $KMnF_3$ are considered as ideal host candidates. They are characterized by low phonon energies, high chemical stability and good optical transparency over a wide wavelength range; therefore, they are often used as the host materials for upconversion. Additionally, the host lattice based on Na^+, Ca^{2+}, and Y^{3+} cations with an ionic radius close to the lanthanide dopant ions prevents the formation of crystal defects. Among the fluorides, hexagonal phase sodium yttrium fluoride (β-$NaYF_4$) is regarded as the most efficient host materials for upconversion due to the very low characteristic phonon energy for this crystal lattice (350 cm^{-1}).[68] The crystal structure of the hexagonal phase $NaYF_4$ has been considered beneficial for upconversion efficiency because two types of relatively low-symmetry cation sites are occupied by Na^+ and RE^{3+} ions.[69] Numerous studies have shown that the hexagonal $NaYF_4$ is a much better host lattice for the upconversion emission than its cubic counterpart. Compared to cubic $NaYF_4$:Yb^{3+},Er^{3+}, the green emission in hexagonal-phase $NaYF_4$:Yb^{3+},Er^{3+} is approximately 10 times more efficient. The CaF_2 host lattice shows high thermal and chemical stability, wide transmission range and low phonon energy (328 cm^{-1}). However, the introduction of trivalent lanthanide ions in the divalent alkaline earth fluoride MF_2 (M = Ca, Sr, Ba), in which the Ln^{3+} ion substitutes the M^{2+} ion, potentially leads to the formation of crystal defects and lattice stress due to the difference in charge between the ions.[70] Only lanthanum fluoride (LaF_3) has intense low-energy phonons (Fig. 11), which are advantageous for reducing the multiphonon quenching of the upconversion emission. These modes are located at 227 and 390 cm^{-1}.[71] Other heavy halides (*e.g.*, chlorides, iodides and bromides) exhibit phonon energies less than 300 cm^{-1}, but because of their low chemical stability and hygroscopicity, their potential for application is somewhat limited. The next group of materials that is used as upconversion lattices are oxides (such as Y_2O_3, Gd_2O_3, and Lu_2O_3). Oxide particles are stable in a wide temperature range; moreover, they have good chemical stability and can be doped with a wide variety of lanthanide ions due to the relatively small difference in the ionic radius of the dopant and the same charge as the RE host cations. However, their phonon energy is relatively high (larger than 500 cm^{-1}) due to the stretching vibration of the host lattice. The emission intensity of α-$NaYF_4$ co-doped with Er^{3+} and Yb^{3+} was 20 times higher in comparison to Y_2O_3 co-doped with the same ions.

The choice of low-phonon energy host lattice is crucial for obtaining efficient upconversion or PA. In the high-energy phonon hosts, the luminescence lifetimes, and thus the populations of the intermediate states are reduced by multiphonon relaxation, resulting in low efficiency for upconversion processes. Recently, spectacular PA results have been achieved with ultra phonon energy nanoparticles (KPb_2Cl_5 and KPb_2Br_5[4]) and a more conventional tetrafluoride host ($NaLuF_4$[28]), which clearly indicate that low cut-off energy phonons are important, but they are not the only parameters determining the possibility to get highly non-linear PA emission.

3.2.2 Thermal and phonon effects. Despite the extensive available knowledge on the impact of the host matrix and the ligands on upconversion, there is less experimental evidence on how PA responds to the local environment and chemical surroundings. Here, we highlight the role of temperature-dependent multiphonon relaxation, which is expected to play an important role in energy looping and ESA. Because the PA emission proceeds *via* a relatively complicated set of ETs occurring between multiple manifolds in single doping ions or between the sensitizer and acceptor ions, understanding the role of multiple phonon-assisted (MPA) relaxation or phonon assisted ETr (PAET) is critical to enable the development and optimization of materials suitable for PA.

The Stark levels belonging to one J manifold of a given lanthanide ion ($4f^N$: $^{2S+1}L_J$) in a given host material are usually

split by no more than the available maximum host phonon energy. Because the electron–phonon interaction for the 4f optically active electrons (being screened by electrons in the filled 5s and 5p orbitals) in trivalent lanthanides is low, the relaxation rates of the transitions within a single J manifold are usually much faster than the inter-manifold ($J \rightsquigarrow J'$, with energy gap $\Delta E_{JJ'}$) relaxation rates. A population quasi-equilibrium is established within a single manifold, while inter-manifold transitions are realized by either photon emission (A_r) or sum of all non-radiative transitions (W_{nr}) accompanied by the generation of matrix phonons.

$$\frac{1}{\tau_e} = A_r + \sum W_{nr} \tag{3-1}$$

Due to the interaction of the 4f electrons with their surroundings, these intermediate processes determine the emission quantum yield and efficiency of numerous phenomena such as CR, non-resonant pumping and ET between manifolds or ions, and CL. The non-radiative transition probability is typically quantified by the so-called energy gap law. This phenomenological law, although sufficient to describe most dopants and hosts, may not be valid at increased temperatures and for all $J \rightsquigarrow J'$ transitions (*e.g.* for large $\Delta E_{JJ'} > 2000$ cm^{-1}, and in some hosts, for small $\Delta E_{JJ'} \leq 700$ cm^{-1}, selection rules of $J = 1 \rightarrow J = 0$ may also apply).[72,73]

Based on the Miyakawa–Dexter theory,[74] the MPR rates $W_{JJ'}(\Delta E_{JJ'})$ were phenomenologically found to exhibit exponential dependence on the energy gap $\Delta E_{JJ'}$ between the J and J' manifolds:

$$W_{JJ'}(\Delta E_{JJ'}) = W_{JJ'}(0)\cdot\exp(-\alpha\cdot\Delta E_{JJ'}) \tag{3-2}$$

where $W_{JJ'}(0)$ is the relaxation rate (for a given host material) extrapolated to zero energy gap, which can be obtained by plotting various $W_{JJ'}$ for various $\Delta E_{JJ'}$, found in various lanthanide ions and given hosts. $W_{JJ'}(0)$ and α (experimentally derived exponential coefficient) depend on the host crystal and electron-lattice coupling strength, and with some exceptions independent of the rare earth ions studied or electronic states involved. Three to seven host phonons were shown to be effectively responsible for MPR.[72] This phenomenological relationship is very convenient because with reasonable accuracy, it enables the determination of the properties of luminophores by measuring the relaxation rates ($W_{JJ'}$) for a small number of energy gaps ($\Delta E_{JJ'}$), which correspond to various $J \rightsquigarrow J'$ transitions in a new material. Alternatively, these parameters can be obtained from existing tables[73] for known materials. In general, the stronger the electron–phonon coupling, the faster the multi-phonon relaxation rates expected.

A similar relationship describes PAET processes (*e.g.* CR, ET between two lanthanide ions, *etc.*), as follows:

$$W_{PAT}(\Delta E_{JJ'}) = W_{PAT}(0)\cdot\exp(-\beta\cdot\Delta E_{JJ'}) \tag{3-3}$$

where α (eqn (3-2)) and β (eqn (3-3)) can be related to each other.[75] α and β are exponential coefficients experimentally derived for a given host, but their absolute values are not necessary to relate the PA behaviour to temperature change. At low temperatures, only the spontaneous emission of phonons occurs. With an increase in temperature, the PAET rates increase due to the stimulated emission of phonons. This is especially pronounced for low energy phonons, which may dominate over cut-off phonon frequencies.

Based on theory,[10] the multi-phonon-assisted ET (either relaxation or inter ionic ET) can be expressed as follows:

$$W_{JJ'}(\Delta E_{JJ'}, T) = W_{JJ'}(\Delta E_{JJ'} = 0, T = 0)\cdot\exp(-\alpha\cdot\Delta E_{JJ'}) \times \left[\pm 1 \mp \exp\left(\mp\frac{\hbar\omega}{k_B T}\right)\right]^{-P} \tag{3-4}$$

The upper plus/minus signs in the last bracket refer to phonon emission, while the bottom ones describe phonon absorption. The equation, $P = \Delta E_{JJ'}/\hbar\omega_{max}$, can be used to determine the total (integer) number of effective phonons involved in a relaxation process (with phonon energies of $\hbar\omega_{max}$ being smaller than the highest energy of the optical phonon in the host vibrational spectrum). Generally, most observations of PA for various dopants and matrices have been demonstrated at cryogenic temperatures. Specific temperatures enable tuning of non-resonant MPA and PAET processes by modulating the phonon density of states. The temperature-dependent ET efficiencies strongly depend on the available dominant phonon energies and the resulting number of phonons required to bridge a given energy mismatch. The temperature-dependent MPR rates may be easily achieved by subtracting the inverse of the radiative lifetime from the inverse of an experimental lifetime. The MPR rates increased by *ca.* 10-fold from 100 up to 700 K for 2500–3500 cm^{-1} energy gaps, which required up to 6 phonons.[72] Simultaneously the PAET rates decreased by *ca.* 50% from 80 K to 300 K.[76] This shows how complex the PA phenomenon may be in response to a variation in temperature, in addition to its strong dependence on other factors such as dopant type and concentration, host type and composition, NP surface ligands and surrounding solvents.

3.3 Challenges limiting the development of PA in bulk materials

The lower degree of investigation of PA in bulk materials may originate from its mechanistic complexity and the narrow optimal conditions over which PA occurs. The PA phenomenon, being a positive feedback system, is highly susceptible to tiny perturbations, especially compared to Stokes emitters. The giant nonlinearity of PA means that these small disturbances in ET pathways lead to disproportionately large changes in luminescence. This sensitivity is exacerbated by the complexity of these ET networks in PA materials, where luminescence quenching may occur *via* any process that directs energy away from the looping and emitting levels, whose populations are critically important to make the PA material absorb light.[12] Thus, the PA phenomenon is very demanding in terms of materials (*i.e.* dopant type and concentration, type of host, and surface quenching) and experimental methods (*i.e.* relatively high pump power density, long acquisition times, smooth pump power tuning, *etc.*).

Research in PA utilization is also limited by several practical considerations, such as the need to (i) precisely control the excitation wavelength to ensure resonance or lack of resonance with narrow excitation bands, (ii) pump strongly and continuously or (iii) utilize cryogenic temperatures to diminish MPR. Finally, experimentally confirming the presence of PA is challenging; although there are rigorous criteria for avalanching (Section 2.5), these criteria are debated by some in the community, and ambiguous to others. Consequently, numerous scientific reports on PA luminescence do not definitively confirm all the PA features, and many could be ascribed to pre-PA cases (*i.e.* energy looping)[77] or explained as a combination of ESA and ETU.[17] All these facts have contributed to PA remaining a scientific curiosity with niche applications for over 40 years since its discovery.

Compared to conventional Ln^{3+}-doped materials, the PA phenomenon requires a radical change in the paradigms in materials design. For example, in Ln^{3+}-doped bulk materials photoexcited through GSA (Fig. 10a), the effective concentration of doping ions has been typically limited to below 1% due to the belief that higher concentrations result in "concentration quenching" of the luminescence due to CR or energy migration to defects.[78] Alternatively, in PA luminophores, the absorption occurs from the first excited level, which originally is almost empty, and thus the sample is initially transparent at the pump wavelength. The population of this level and the resulting absorption coefficient may be increased, but the CR process must be engaged to multiply (double) the number of ions in this state (Fig. 10b). This is achieved by increasing the interaction between neighbouring ions by increasing their concentration. Because the luminescence intensity is proportional to the concentration of the activator (in some range), these two facts make the concentration effects a concentration enhancement rather than concentration quenching. However, it should be noted that by further increasing the dopant concentration, the quenching effects start to outweigh the concentration enhancement. Simultaneously, great care must be devoted to optimizing the selection of the hosts and dopants to reduce the non-radiative depopulation of the starting level and stream the pumping energy to enhance the population of the first excited level or the luminescence. The former is achieved through the selection of the appropriate (typically low) phonon host materials, optimization of the temperature, elimination of the sensitizer ions used typically for upconversion, and selection of the lanthanide activators with a supportive energy level scheme that promotes efficient ESA and CR and reduces non-radiative de-excitation.

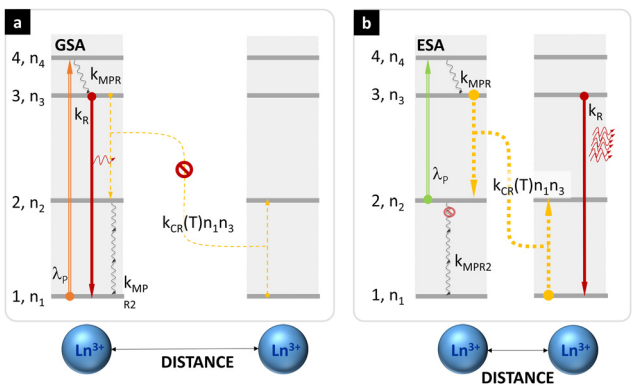

Fig. 10 Comparison of the paradigms for conventional (a) and photon avalanche (b) based luminophores. The conventional GSA-based emission is susceptible to CR-caused concentration quenching (a), while in the PA mode, a high dopant concentration and CR are responsible for positive feedback, enhanced ESA absorption and luminescence (b).

4. Considerations for scaling PA to nanoscale materials

4.1 Challenges limiting the development of PA in nanomaterials

Similar to the many challenges limiting research into bulk PA materials, even more obstacles previously hindered the observation of PA in nanoscale materials. The sensitivity of PA is especially troublesome in nanoscale materials, where their surface to volume (SA : V) ratio is high. The large SA : V ratio of nanoscale materials means that a large portion of these materials is exposed to surface quenching from the environment and defects. The high dopant concentrations required for PA can foster rapid energy migration to the surface of nanomaterials, which is more prone to defects and has a higher concentration of quenching species such as ligands and solvent molecules. Colloidal nanoparticles must be stabilized by ligands to maintain the advantages of colloidal dispersion (discussed in Section 4.4). To date, only a few theoretical[6,79] and experimental[12,80] studies have discussed the impact of surface quenching on PA. Thus, the lack of understanding how to mitigate quenching in nanoscale PA materials has limited their discovery.

Another challenge in achieving PA in nanoscale materials has been the need to develop reliable methods for synthesizing colloidal nanoparticles with robust and reproducible properties. Fortunately, the field of lanthanide-doped nanoparticles has been maturing since 2004, when Haase *et al.*[68] and soon after Gue *et al.*,[81] Yan *et al.*[82] and Capobianco *et al.*[83] managed to develop low-temperature methods for the synthesis of monodisperse $NaYF_4$ nanoparticles. In the 20 years since these seminal reports, researchers have developed robust methods for synthesizing high-quality lanthanide upconverting nanoparticles, *e.g.*, using thermal decomposition.[83] These methods allow control of the crystal size, shape, and crystal phases, *e.g.*, low-phonon-energy matrices such as β-$NaYF_4$,[84,85] which is well-known to host higher upconversion efficiencies than its α-$NaYF_4$ analogue. Additional upconversion enhancement is realized through the synthesis[24,25,85–87] of core–shell nanoparticle heterostructures.[88–91] Undoped shells passivate the doped cores by preventing deleterious ET to surfaces, while the doped "active" shells can be used to sensitize absorption,[25] segregate incompatible dopants, and mediate ET between domains,[23] thereby allowing fine control of the complex ET networks among lanthanide ions. The ability to grow controlled shells has enabled new doping compositions and paradigms, particularly highly doped and alloyed nanoparticles.[2,77,92–95] In

addition to methods for minimizing surface quenching,[93,96–98] biofunctionalization protocols have been developed. All these advancements contributed significantly to the current state of research into lanthanide-doped nanoparticles. In principle, ANPs offer similar advantages together with higher upconversion efficiencies and potential use in applications that exploit the extremely nonlinear response, although several challenges remain. Below, we discuss important considerations when adapting PA for nanoscale materials.

4.2 Size effects and scaling laws

Decreasing the size of crystals down to single nanometres decreases the number of luminescent centres and simultaneously increases their surface to volume ratio, SA : V. Moreover, the distribution of luminescent ions is non-homogenous within the volume of NPs, which may impact the upconversion rates.[99] A significant amount of active ions in nanosized materials is located close to the surface,[100] and thus their excited states are susceptible to quenching by crystal structure defects, the local chemical environment of the active ions, ligands or the solvent molecules.[101] For example, for spherical particles with a diameter of 3 nm, nearly 50% of their atoms are present on the surface. In the case of 10 nm particles, this decreases to 20%, while for a particle with a diameter of 1 μm, only ~0.15% of its atoms are found on its surface. The increasing amount of superficial lanthanide ions makes them susceptible to non-radiative relaxation of both emitting and intermediate levels, occurring in the course of interaction with solvent and ligands molecules. The higher SA : V also increases the relative contribution of surface defects, which cause the additional luminescence quenching. As a consequence, the quantum yield for $NaYF_4$:2%Er^{3+}, 20%Yb^{3+} nanoparticles with a size in the range of 10 to 100 nm is in the range of 0.005–0.3%, while for bulk materials, this parameter can be considerably higher (3%).[100] Direct evidence of the impact of SA : V and its possibly thermal effects on PA was shown by Deng, *et al.*[102] In their work, isolated nanoparticles did not exhibit PA, but clear avalanching phenomena emerged when microscale aggregates of their nanocrystals were formed, which may be a sign of thermal issues. Approaches to circumvent surface quenching have been extensively studied for conventional UCNPs, and thus some fundamental knowledge exists. There are several methods to reduce the detrimental role of MPR and augment the emission quantum yields of up-converting nanoparticles. These methods include optimization of the dopant and co-dopant concentrations,[103,104] intentional altering of the local chemical and structural environment by adding passive co-dopants or changing the 'structural' cations, and managing the distribution of active ions in the host materials by the core–shell approach.

4.3 Heterostructures

One of the most effective strategies to improve the luminescent properties of nanoparticles is the utilization of core–shell structures, where the shell layers are grown around the luminescent core.[105,106] The protective undoped shell both reduces the surface quenching and changes the balance in multiple nonradiative pathways. By coating the shell, the total intensity improves from several times to several hundred times in various upconversion nanoparticle structures.[107] Additionally, nanoparticles doped with lanthanide ions have been used in multicolour labelling and multiplexed bio-detection. The strategy for tuning the emission colour was achieved by manipulating dopant-host combinations and the doping lanthanide ion concentration. For example, the emission spectra of Er^{3+}-doped $NaYF_4$ and $KMnF_3$ nanoparticles differ, owing to the distinct ET pathways stemming from the different dopant-host interactions.[108,109] The concentration, and thus the distance-dependent interaction between the dopants and between the dopants and sensitizers play a key role and actually define the upconversion efficiency. The combinations of different upconverting lanthanide ions and changes in the concentrations thereof cause the tuning of the fluorescence emission wavelengths from the visible to near-infrared (NIR) regions. However, co-doping nanoparticles with several different emissive ions may facilitate the ET process, which leads to deleterious CRs between the adjacent dopant ions, often resulting in the quenching of the excitation energy, and thus in a reduction in the luminescence intensity from the doped ions.[78,110] This limitation can be overcome by providing the spatial isolation of the emissive ions in the core–shell structure by selective doping of the core and shell. The advantages of spatial positioning of the lanthanide ions in the core and shell were first demonstrated by Qian *et al.*[84] The core ($NaYF_4$:Yb^{3+},Er^{3+}) nanoparticles coated with active shells ($NaYF_4$:Yb^{3+},Tm^{3+}) allowed a reduction in the quenching of the fluorescence from the active ions through an increase in the distance between them.

4.4 Ligands and coatings

Currently, nanoparticles are coated not only with other inorganic materials but also with a variety of materials such as silica,[111–113] polymers[85,114,115] and metal nanoparticles[116–118] (Fig. 11). Coating the surface of nanoparticles not only allows an

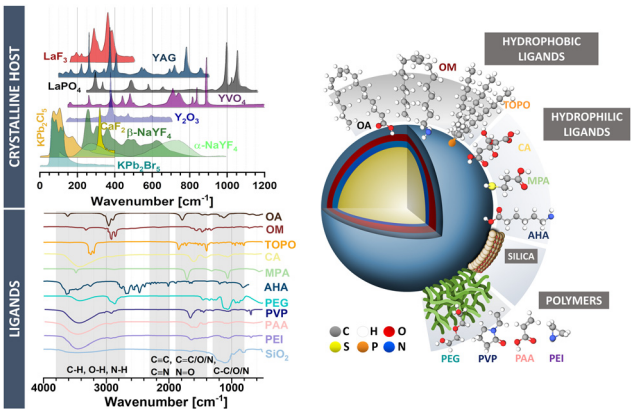

Fig. 11 Phonon properties of the crystalline host and ligands used to stabilize colloidal nanoparticles. Band absorption of vibration modes from solvents and surface ligands. The maximum vibrational phonon energies of commonly used inorganic lattice, based on digitized data for CaF_2,[124] $NaYF_4$,[125] Y_2O_3,[126] YVO_4,[127] $LaPO_4$,[128] YAG,[129] LaF_3,[129] $LaCl_3$,[130] KPb_2Br_5 and KPb_2Cl_5.[4]

improvement in their luminescent properties but also their functionalization for biomedical applications and the creation of multifunctional structures. Alternatively, the capping ligands influence the chemical, physical and optical properties of upconverting nanoparticles. However, their presence on the surface of nanoparticles is necessary to stabilize the surface and prevent the agglomeration of the particles during their synthesis.[119] This is necessary, especially when nanoparticles are to be used in biology and medicine and characterized by a narrow size distribution, suitable shape, high aqueous dispersability, and biocompatibility, and thus require a special method for their synthesis. The most effective method for the synthesis of nanoparticles allowing shape and size control is the thermal decomposition reaction of organic metal salts in high-boiling point solvents, typically with polar capping groups and long hydrocarbon chains (such as oleic acid and oleylamine).[83,120] These molecules can selectively bind to the surface cations of nanocrystals through their carboxylic groups and form a layer of surface ligands. Carboxylic acids are considered good complexing agents of rare earth ions; however, these molecules may also act as surface oscillators, which significantly quench the upconversion emission of lanthanide ions due to the high energy stretching vibration of their long carbon chain $(CH_2)_n$ (about 2800–2950 cm^{-1}) and polar COOH groups (about 3000–3500 cm^{-1}).[121] Due to the presence of a hydrophobic ligand-stabilizing surface, nanoparticles are generally hydrophobic, only dispersable in nonpolar solvents and requiring post-synthetic functionalization to transfer them to aqueous colloids to finally achieve biocompatibility. To enable the dispersibility and stability of nanoparticles in aqueous media, it is indispensable to make them hydrophilic and conjugatable with various biomolecules and functional groups (*e.g.*, carboxyl, amine, thiol, and phosphate).[122] Different surface engineering strategies to transfer hydrophobic nanoparticles from the organic to aqueous phase have been reported including ligand exchange and ligand attraction reactions using a number of different ligands such as citric acid, poly(acrylic acid) (PAA), poly(ethylene glycol) (PEG), poly(ethyleneimine) (PEI), polyvinylpyrrolidone (PVP), and encapsulation in a silica shell. Hydrophilic groups on the surface of nanoparticles provide water-solubility and enable their further bioconjugation. The 'dark' side of the surface functionalization of NPs is that the vibrational states of chemical bonds such as O–H, C–H and N–H match the phonon states of the host lattice and may severely quench the emitting and intermediate levels of the luminescent, long living lanthanide levels.[123] The quenching of the lanthanide excited states occurs by most chemical ligands; however, those comprised of light elements (such as –OH and –CH groups) quench the nanoparticle luminescence more effectively.[101] Simultaneously, O–H vibrations have been reported to be highly effective compared to the C–H vibrational quenching of the excited states. Typically, the upconversion from Yb^{3+} sensitizers to Er^{3+}/Ho^{3+} co-doped nanoparticles results in an intense green emission together with weak red emission. The citrate ligands and OH^- groups present on the surface of NPs after their hydrothermal synthesis change their green to red emission ratio. Additionally, the high energy vibrational modes of the OH^- groups (3200–3600 cm^{-1}) typical for water significantly reduce the emission efficiency compared to oleate-stabilized nanoparticles dispersed in organic solvents.[98]

5. Photon avalanching in lanthanide-doped nanomaterials

Due to the challenges of investigating PA materials in nanoscale size regimes, the development of nanomaterials whose luminescence meet the strict criteria for avalanching has been realized only in recent years. These advances have been driven by the development of high-throughput modelling and synthesis of lanthanide-doped nanoparticles. PA emission has been observed in nanoparticles with compositions including $NaYF_4$:Tm^{3+},[2] $LiYF_4$:Tm^{3+} (ref. 6) and KPb_2Cl_5:Nd^{3+} (ref. 4) (Fig. 14), as well as in Yb^{3+} co-doped with Pr^{3+}.[3,11,14] Table S10 (ESI†) summarizes the studies in the literature on lanthanide-doped nanostructures that claim nanoscale PA emission. Although PA is claimed to occur in other classes of materials (*e.g.*, gold and silver nanowires and gold nanorod-nanoparticle hybrids[131–133]), we focus our survey on lanthanide-doped nanoparticles. The summary in Table S10 (ESI†) lists the essential parameters of the experiments, such as the sizes and compositions of the materials, the used excitation and emission wavelengths, and the key parameters characterizing the PA phenomenon, including the slopes of the emission intensity power dependence or emission dynamics parameters. The table is supplemented by additional comments about the feasibility of achieving PA under the presented conditions and possible alternative explanations based on the available (not always full) characterization presented in the given articles. These comments were based on clearly defined conditions (efficient ESA with negligible GSA and efficient energy looping) and spectroscopic criteria (*i.e.* clear threshold and steep power dependence with $S > 10$, followed by saturation of emission intensity *vs.* pump intensity, pump power dependent rise times, and PA gain of >100), which should be expected from PA emission. To satisfy the biomedical application of PA, some potential NIR excitation lines are predicted beyond that proposed and studied in bulk materials. However, precise ESA wavelengths are often difficult to define and seem critical within the spectral resolution $\phi \pm 5$ nm.

This ESI† focuses on papers that either hypothesize or directly show photon avalanche behaviour in nanoparticles. There are many reports ascribing luminescence behaviour to PA (given that slopes are higher than 4 and simple ESA/ETU is not sufficient to explain the UC process), but most claims are unsupported and are not formally considered PA because they do not meet the strict criteria outlined in Section 2.5, *i.e.* (i) $\beta > 10^4$ and observation of (ii) clear threshold behavior, and (iii) elongation of rise times near the threshold. The term, "photon avalanche-like behaviour," can be also found in the literature, which typically indicates a situation in which only part of the expected PA features is observed and the authors suspect other mechanisms than pure PA (*e.g.* thermal effects, multiple CR and ESA) play a role. Owing to the set of specific requirements necessary to observe PA, the efficiency of PA varies between different dopant

types, host types and compositions, as well as the presence of external quenchers or temperature. These considerations, supplemented with a collection of the most up-to-date literature on PA emission in nanomaterials are presented in Table S10 (ESI†).

5.1 Establishing the foundation for the discovery of PA in nanomaterials

5.1.1 Energy looping nanoparticles and photon-avalanche-like behaviour. Prior to the first rigorously confirmed reports of PA in lanthanide-doped nanoparticles, several developments established the foundation for the eventual breakthrough. Energy-looping had been observed by numerous groups without the observation of large nonlinearities. For example, in 2016, Levy *et al.*[77] reported the use of a high-throughput rate equation modelling to identify 0.5%Tm^{3+}:$NaYF_4$ nanoparticles as the optimal composition for upconversion excited at 1064 nm, although this wavelength is not resonant with the GSA transition. They reported slopes of $S \sim 3$, firmly in the energy-looping regime. Later work utilized these Tm^{3+}-doped energy-looping nanoparticles (ELNPs) to achieve the first continuous-wave upconverting micro-lasers, whose low thresholds were attributed to the population inversion and gain, facilitated by the avalanche-like energy-looping mechanism.[134] In 2017, Liu *et al.*[95] attributed their ability to achieve amplified stimulated emission and stimulated emission depletion (STED) microscopy with $NaYF_4$ nanoparticles co-doped with 8%Tm^{3+} and 20%Yb^{3+} to a sensitized "avalanche-like process" that induces population inversion.

5.1.2 Computational prediction and demonstration of PA nanoparticles. In 2019, Bednarkiewicz *et al.* used rate equation modelling to computationally predict that if PA could be achieved, *e.g.*, in Nd^{3+}-doped particles excited at 1064 nm, the giant nonlinearities would enable super-resolution imaging in a simple, single-beam confocal microscope (as opposed to the complex multi-beam optics of STED).[95] For example, with nonlinearities of 80, simulations of photon-avalanche single-beam super-resolution imaging (PASSI) resolved features as small as 20 nm. Interestingly, the assumptions made during these Nd^{3+} PA simulations (aiming to simplify the model) were not confirmed experimentally, until ultra-low phonon materials were developed for Nd^{3+} doping, as reported by Skripka and colleagues.[4] This confirms that although the modelling is useful to derive and predict directions for studies, the PA phenomenon is a complex and highly susceptible to nuances and delicate balances between the processes involved.

5.2 PA in singly doped nanoparticles

The first confirmed reports of lanthanide-based PA in single nanomaterials (*i.e.*, not aggregates) used singly doped colloidal nanoparticles including $NaYF_4$:Tm^{3+} NPs,[2] $LiYF_4$:Tm^{3+},[6] KPb_2Cl_5:Nd^{3+} (ref. 4) and $NaLuF_4$:Tm^{3+} (ref. 28) (Fig. 12). In 2021, Lee *et al.* demonstrated the first rigorously validated PA in a single nanomaterial using core–shell $NaYF_4$ nanoparticles highly doped with Tm^{3+} (8–100 mol%) excited at 1064 nm. These avalanching nanoparticles (ANPs) exhibited nonlinearity orders as high as S = 22–31 at threshold powers of *ca.* 20 kW cm^{-2} (Fig. 14) and were shown to meet all three stringent criteria for classifying PA (Section 2.5), including the extension of the rise times to 608 ms. The authors attributed their ability to access PA to the enhancement in cross-relaxation resulting from these high dopant concentrations, together with the thick, 3–9 nm $NaY_{0.8}Gd_{0.2}F_4$ shells, which prevented quenching of PA on the surface of the ANPs. Subsequently, avalanching was observed upon doping Tm^{3+} (3–8%) in $LiYF_4$ NPs, with slopes as high as 12[6] and extremely high values of >500 for $NaLuF_4$:Tm^{3+}.[28] One may note the huge variability in (with thresholds of above 90 kW cm^{-2}) the achieved non-linearities in the Tm^{3+}-doped hosts, from 12 to over 30 and up to 500, which occur in the tetrafluoride fluoride materials $LiYF_4$, $NaYF_4$, and $NaLuF_4$, respectively. These observations confirm the capricious character of photon avalanche emission, given that changes in the local crystallographic sites and

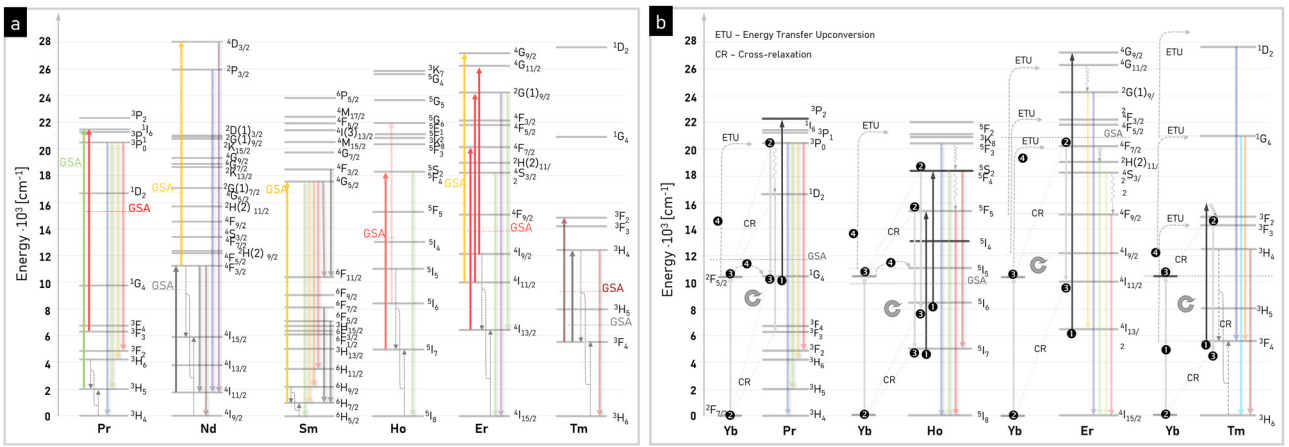

Fig. 12 Overview graph of PA processes that have been observed or can be predicted in singly (a) and co-doped (b) lanthanide ions. The detailed studies on PA in Pr^{3+},[135] Nd^{3+},[29] Sm^{3+},[136] Ho^{3+},[137] Er^{3+},[58] and Tm^{3+} [2] ions and ion-combinations for Yb^{3+}–Pr^{3+},[135,138] Yb^{3+}–Ho^{3+},[139] Yb^{3+}–Er^{3+} and Yb^{3+}–Tm^{3+} [140] are provided in more detail in the summary tables (available in ESI†). The (1), (2), (3), *etc.* symbols indicate the sequence of ET steps in the Yb co-doped photon avalanching pairs. The line named 'GSA' indicates the energy mismatch between the photoexcitation PA photons in relation to the energy levels.

crystal field effects, and possibly tiny variation in the excitation laser line may significantly modify the basic PA features. This variance may also indicate that the methodology of PA measurements and characterization are not sufficiently standardized, and cross-lab verifications in the near future must be performed to understand the origin of these discrepancies.

5.3 Sensitized PA *via* co-doping in nanoparticles

Besides the classical PA scheme (Fig. 2 and 3), in which energy-looping occurs between the same type of dopant (Fig. 12a), PA has also been proposed and reported in co-doped systems, *e.g.*, utilizing different sensitizing and emitting dopants in the same crystalline domain (Fig. 12b). In the sensitized PA scheme reported by Liang *et al.*,[3] and later Dudek *et al.*,[11] Yb^{3+} ions were used to sensitize Pr^{3+} emitters. Core/shell nanoparticles of $NaYF_4$:0.5%Pr^{3+},15%Yb^{3+}@ $NaYF_4$ exhibited PA emission bands at 607 nm and 482 nm, with a slope of 26 and thresholds as low as 60 kW cm^{-2}.[3]

In these systems, the excitation wavelength of the sensitizer remains off-resonance with the wavelengths used to excite the emitter ions through resonant ESA. Owing to the high absorption cross-section and limited concentration quenching of Yb^{3+} ions, these ions accept energy from the looping emitter ions and (i) store it in their long-lived $^2F_{5/2}$ levels or (ii) spread this energy efficiently in the host. Then, these excited Yb^{3+} ions are capable, as in conventional upconversion, of sequentially donating this energy back to neighbouring emitting ions, and thus build the population of intermediate excited states. This is in contrast to the conventional upconversion, in which Yb^{3+} ions are excited directly with 940–980 nm light. Thus, these sensitized PA schemes may be envisioned to occur (similar to conventional UC scheme) between Yb^{3+} sensitizers and $^3H_4 \rightarrow {}^1G_4$ transitions in Pr^{3+}; $^5I_8 \rightarrow {}^5I_5$, $^5I_7 \rightarrow {}^5F_5$ and $^5I_6 \rightarrow {}^5S_2$ transitions in Ho^{3+}; $^4I_{15/2} \rightarrow {}^4I_{11/2}$ and $^4I_{11/2} \rightarrow {}^4F_{7/2}$ transitions in Er^{3+} and $^3F_4 \rightarrow {}^3F_3$, $^3H_4 \rightarrow {}^1G_4$ and $^1G_4 \rightarrow {}^1D_2$ transitions in Tm^{3+} ions. The preliminary results[135,141] for the sensitized approach support the feasibility of achieving PA emission at a much wider selection of emission lines. For example, under 854 nm, Yb^{3+},Pr^{3+} PA behaviour was observed, showing high pump power dependence slopes and pump power-dependent rise times. The 854 nm wavelength is resonant with $^1G_4 \rightarrow {}^3P_{0,1,2}$,$^1I_6$ ESA in Pr, and the two CR processes between the Pr–Pr pair (Pr: $^3P_{0,1,2}$, $^1I_6$; Pr: $^3H_4$) $\rightarrow$ (Pr: $^1G_4$, Pr: $^1G_4$) and between Pr and Yb (Pr: $^3P_{0,1,2}$, $^1I_6$; Yb: $^2F_{7/2}$) $\rightarrow$ (Pr^{3+}: $^1G_4$; Yb: $^2F_{5/2}$) drive energy looping (Fig. 12b). Ultimately, Yb can enhance the Pr: $^1G_4$ population through the Yb: $^2F_{5/2} \rightarrow$ Pr: $^1G_4$ transition. Interestingly, the described Yb^{3+}-sensitized Pr^{3+} PA emission was observed in the $LiYF_4$ single-crystal matrix, but not in the $YAlO_3$ crystal host. This is explained by the fact that the spectral overlap between ESA in Pr^{3+} and GSA in Yb^{3+} is non-negligible, and higher ET rates between Yb^{3+} and Pr^{3+} and within the Pr^{3+} ions were present as well as slower decays found for $YAlO_3$ (*i.e.* 50/11/2000 μs for YLF and 12/4/650 ms for $YAlO_3$ for the Pr^{3+}: $^3P_0$/Pr: $^1G_4$ and Yb^{3+}: $^2F_{5/2}$). These facts show the sensitivity of PA to nuances related to the absorption cross section for ESA and GSA, the metastable character of the intermediate levels, and the host phonon energies. Similar PA schemes may be derived for other lanthanide pairs, in which Yb sensitizes photon avalanching in Er^{3+}, Ho^{3+} or Tm^{3+}.

5.4 ANP nano-heterostructures – expanding the spectral range of ANPs with energy migration

Despite achieving moderate nonlinearities (*ca.* 9) in pure Yb^{3+}/Pr^{3+} co-doped nanoparticles, most attempts to achieve PA in homogeneously co-doped systems result in sharply quenched emission due to the cross-relaxation between the ions. This CR is particularly detrimental to PA because it disrupts the delicate and critical balance between ESA, looping, and emission, an effect that is strongly amplified by the nonlinearity of PA. To minimize this CR, researchers have borrowed the strategy of sequestering sensitizing and emitting dopants into different domains of hetero-structured core–shell nanoparticles. In this scheme, the nonlinear behaviour (*i.e.* high slopes, long rise times, and larger dopants content) of the avalanching ions in one crystalline domain is transferred (typically *via* resonant ET) to the emitting ions in a neighbouring domain, broadening the range of emitters that can exhibit PA emission (Fig. 2l).

Two of these schemes have been proposed recently for UCNPs, exploiting resonant energy migration through either Yb^{3+} or Gd^{3+} ions in UCNPs. Both schemes have been demonstrated experimentally for avalanching nanoparticles.[3,5] In 2022, Liang *et al.*[37] first reported this "migrating" PA (Fig. 13) with slopes as high as 28 in a four-layer nanoparticle heterostructure consisting of an $NaYF_4$:Yb^{3+}/Ho^{3+} (3/4%) active shell sandwiched between a core and 2nd shell doped with Yb^{3+}/Pr^{3+} (15/0.5%), with an undoped outer shell of $NaLuF_4$. When Ho^{3+} was replaced with Tm^{3+} in these 4-layer heterostructures, high slopes of 46 were observed in the 452 nm emission of Tm^{3+}. In these heterostructures, the 852 nm excitation wavelength is resonant with the ESA of the Pr^{3+} ions, and is simultaneously off-resonance with Yb^{3+} and with GSA of Pr^{3+}. The 852 nm pump is not absorbed by the Ho^{3+} or Tm^{3+}-doped active layers; instead, PA occurs in the Yb^{3+}/Pr^{3+}-*co*-doped layers. The PA-enhanced population is transferred *via* resonant energy migration through Yb^{3+} ions to the Yb^{3+}/Ho^{3+}- or Yb^{3+}/Tm^{3+}-doped active layers. Notably, the emission from all of the doping ions, Pr^{3+}, Tm^{3+} and Ho^{3+}, exhibited features of avalanche emission at many lines in the visible spectrum (*e.g.* Tm^{3+}: 452 nm; Ho^{3+}: 541, 646 nm; and Pr^{3+}: 484, 609 nm), providing avenues for multicolour PA emission at visible wavelengths and PASSI microscopy.

One disadvantage of using the Yb^{3+}/Pr^{3+} avalanching pair is the overlap of multiple Pr^{3+} emission lines with the multiple visible emission of other intermediate lanthanide dopants (Fig. 13), such as Tm^{3+}, Ho^{3+}, Tb^{3+} and Eu^{3+}.[3,9,142] This may pose some technical challenges in distinguishing these spectral fingerprints from various PA labels in complex biological samples. As an alternative to migration through the Yb^{3+} sublattice, Skripka *et al.*[5] used migration through an intermediate Gd^{3+}-doped 1st shell to transfer the excited-state populations generated by PA in the $NaGdF_4$:Tm^{3+}-doped core to Eu^{3+}, Tb^{3+}, Er^{3+}, and Ho^{3+} emitters in a 2nd shell of $NaGdF_4$, which was overcoated with a passivating $NaYF_4$ shell (Fig. 14). Exciting the Tm^{3+} avalanching dopants at 1064 nm resulted in visible

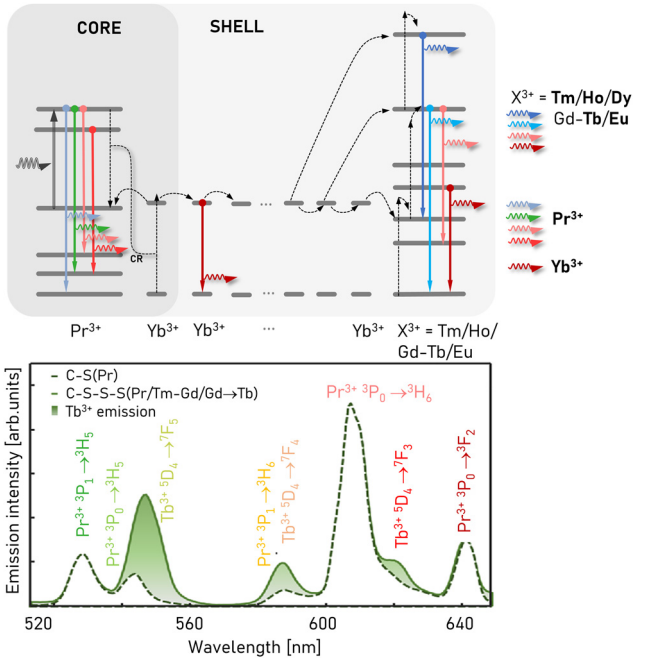

Fig. 13 Basic principles of migrating PA emission. The Yb–Pr pair undergoes sensitized PA mechanism, which makes the Yb^{3+} intermediate migrating ions transfer this behaviour to other lanthanide ions that they sensitize (*e.g.* Tm^{3+} and Ho^{3+}).[3,142] Some emission of emitting ions, which stems from the Yb–Pr^{3+} PA workhorse, spectrally overlap with the Pr^{3+} emission bands. Adapted with permission from ref. 142 Copyright 2024, SPIE and Chinese Laser Press (https://creativecommons.org/licenses/by/4.0/).

emission with nonlinearities of 14.6, 17.2, 10.7, and 11.5, respectively. Notably, the visible emission lines for these emitting dopants do not overlap with that of the Tm^{3+} avalanching dopants. Furthermore, the use of Eu^{3+} and Tb^{3+} is significant because these dopants are typically thought to be less suitable for anti-Stokes emitters.

In addition to imprinting PA behaviour onto other lanthanide dopants, Skripka *et al.*[5] also demonstrated the first transfer of PA nonlinearity to non-lanthanide emitters. $NaGdF_4$:20%Tm^{3+}@$NaGdF_4$ core shell ANPs were used to transfer high energy excitation to CdS/CdSe/CdS quantum dot (QD) heterostructures, which exhibited nonlinearities of 10.5 at the 630 nm QD emission wavelength under sub-band gap 1064 nm excitation. The experience gained with these examples is important because the stringent conditions for PA emission to occur are much more difficult to satisfy compared to simple ET upconversion. The ability to exploit the work-horse photon avalanche 'engine' to achieve PA characteristics broadens the selection of emission spectra to any fluorophore or luminophore, *e.g.* for multiplexing applications.

However, another contribution to multicolour PA emission was recently shown by C. Wang *et al.*,[8] who employed a Tm^{3+} 'PA engine' and Yb^{3+} migrating layer to achieve >60 nonlinearities and Ho^{3+} (S up to 37), Tb^{3+} (S = 48), Eu^{3+} (S = 37), Dy^{3+} (S = 35) and Nd^{3+} emission bands in the PA mode in $NaYF_4$:Tm (8%)@$NaGdF_4$:Yb/Tm (10/1%)@$NaGdF_4$:X (X = Tb, Eu, Dy, Nd)@$NaYF_4$ materials. Although multicolour PA emission was shown, the emission spectra were obviously composed of strong Tm^{3+} emission bands at 450 and 800 nm, which are overlapped with additional weaker bands characteristic for the additional ions.

5.5 PA materials with alternative host matrices: chlorides, bromides, and alloys

The choice of an appropriate host lattice for avalanching lanthanide ions seems to be of critical importance for either PA availability or nonlinearity. For example, the low-phonon energy host lattice minimizes the MPR, increases the occupation of the metastable levels and changes the dynamics of the ET distribution. Oppositely, high-energy phonon hosts are responsible for efficient MPR, which shorten the luminescence lifetimes and reduce the population of intermediate states, ultimately reducing the efficiency of upconversion energy processes. Typically, tetrafluoride $Na(Y/Gd)F_4$ hexagonal nanocrystals have been used, mostly because of their low phonon energies (<400 cm^{-1}), and great advancements have been made in the synthesis of heterostructured nanomaterials for upconversion. These hosts were suitable to show PA phenomenon for the first time in nanomaterials. Recently, colloidal KPb_2Br_5 and KPb_2Cl_5 nanocrystals have been developed, with ultralow 250 and 175 cm^{-1} phonon cut-off energies.[4] Although their synthesis is demanding, these nanoparticles reduced the multiphonon relaxation rates and enabled Nd^{3+} photon avalanche under 1064 nm photoexcitation in the PA regime. This is something that has been postulated previously,[29] but not achieved experimentally in other low-phonon $NaYF_4$ or $LiYF_4$ hosts. It must be noted that although ultralow phonon energy Ln^{3+}-doped materials reduce the multiphonon relaxation, they simultaneously reduce the efficiency of other phonon-assisted processes, such as CR and ET, which in some specific PA schemes may be prerequisite to achieving efficient energy looping.

Beside engineering of MPR, the local crystal field affects the Stark level splitting and has been shown to have a profound importance in PA. For example, replacing the Y^{3+} structural ions with smaller Lu^{3+} ions led to the contraction of the unit cell, and a slight but negligible blue shift in the available phonons and modification of the local crystal field.[28] The spectacularly high, monotonic rise in nonlinearity from S = 41 to over S = 150 was noticed for Lu^{3+} progressively (from 0 to 85%) replacing the Y^{3+} structural ions (at a constant 15%Tm doping of avalanching ions), and a single particle-to-particle variable of S > 400 (up to 525) at 500–600 kW cm^{-2} PA thresholds was explained by the modified magnetic–dipole to electric–dipole transition strength. Even if the results are early and their explanations debatable, this enormously high nonlinearity combined with much shorter rise times of around 9 ms enables the further prediction of new applications in imaging or all-optical data processing. This high nonlinearity enabled the study of S in the center and the edge of 172 nm diameter NPs, confirming the substantial role of surface quenching in PA emission, given that S dropped from 450 in the NP center down to 186 close to the edge.

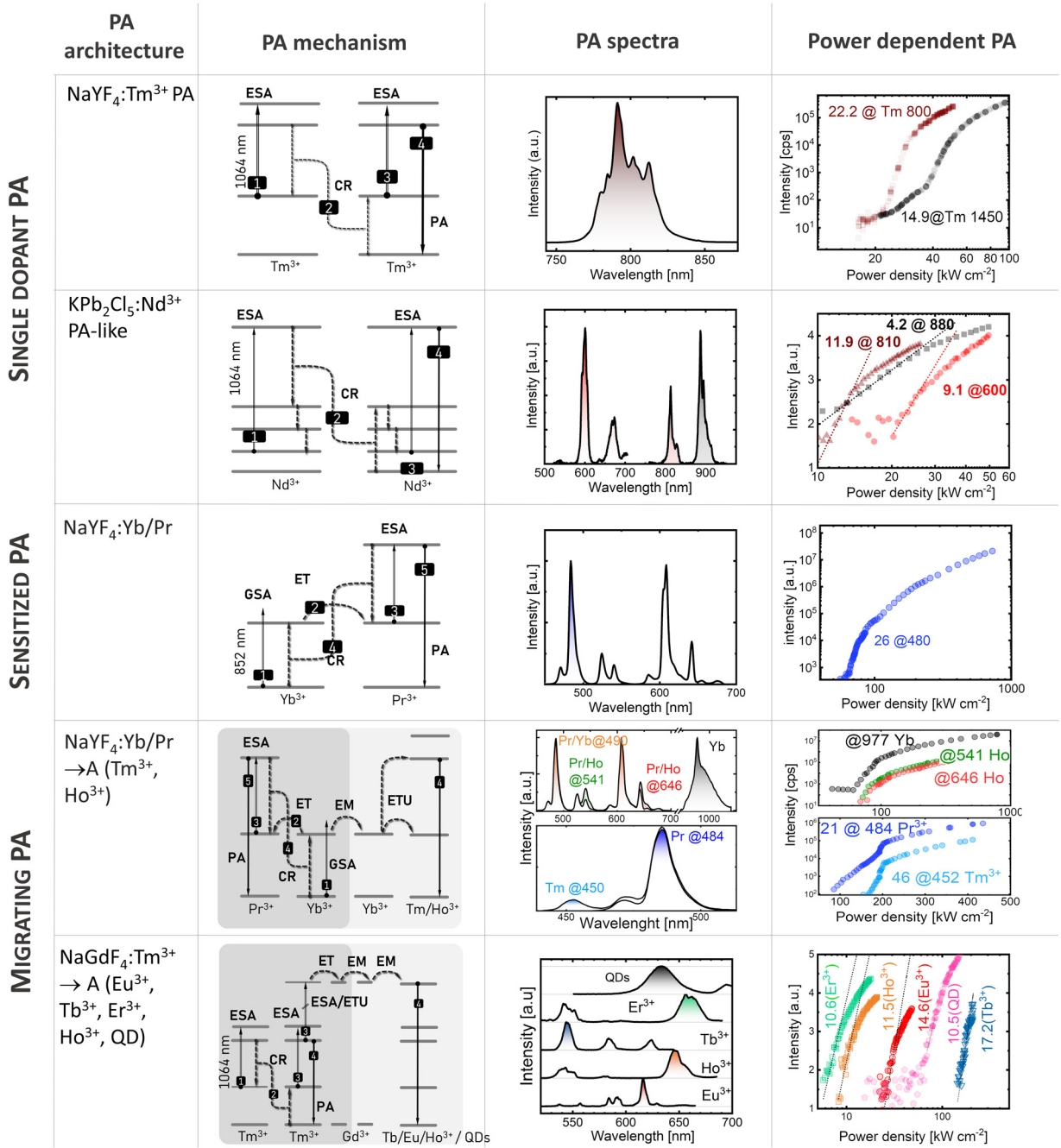

Fig. 14 Mechanisms of multicolour PA emission and examples of PA systems capable of generating PA emission at various wavelengths. (1st and 2nd row) The base approach with a single dopant ion, *i.e.* Tm^{3+} (ref. 2, 6 and 13) or Nd^{3+}.[4] Adapted with permission from ref. 4 Copyright 2023, John Wiley and Sons. (3rd row) Sensitized photon avalanche emission obtained for Pr^{3+}, Yb^{3+}.[3,10,14] (4th and 5th row) New emission lines enabled by multi-shell architecture powered by energy migration from avalanching core.[3–5] Reprinted with permission from ref. 5 Copyright 2023, the American Chemical Society.

6. Applications of photon avalanching nanoparticles

Since its first demonstration in 1979, the PA phenomenon has been studied, aiming for applications in upconversion laser technology[17,36,143,144] or for MIR photon counters.[1,17,31,145] However, the potential to observe this phenomenon in nanoscale materials and at room temperature opens a new range of possible applications that are not achievable with homogenously doped, bulk or microcrystal materials (Fig. 15). Here, we briefly present selected research and technological areas in which ANPs have already realized significant advancements.

Compared to conventional non-linear (*i.e.*, SHG/THG, 2/3PhAbs) or upconversion (*i.e.*, ETU, ESA, CS, and CL) processes, PA shows some features that are critically important and key to enable numerous applications, as follows:

• PA brightness is gained from significantly increased concentration of luminescence centers, which enhance both the absorption and emission intensity.

• PA non-linearity is significantly higher and easier to access (in terms of pump power densities) than other anti-Stokes processes.

• PA nanomaterials stem from UCNP technology, which has made advances in many areas including biofunctionalization, surface passivation, and the development of models that yield a deep understanding of internal ET processes that occur between lanthanide dopants.

Simultaneously, the high non-linearity of the PA luminescence intensity makes it extremely vulnerable to the pump source stability and infinitesimal quenching, which put higher demands on the pump sources and purity of PA materials compared to UC materials, respectively. Although the PA pump power thresholds are relatively moderate (10–100 of kW cm^{-2}) considering sensitive biomedical applications, they are still higher than in conventional upconverting materials (single W cm^{-2}). Moreover, PA materials are much more sensitive to the excitation wavelength selection compared to UC, and suitable compact and cheap laser sources are not always available on the market. Therefore, it is important to explore new applications concurrently with the continuing design of new and improved PA materials.

6.1 PA-based sub-diffraction imaging

6.1.1 Conventional techniques and probes for super-resolution imaging. The first "killer application" of photon avalanching nanoparticles and their giant nonlinear optical properties was their use in sub-diffraction imaging with <100 nm resolution. These ANP applications extend the recent developments in nonlinear optical microscopy and fluorescent dyes, which enable the imaging of single fluorescent molecules[148,149] and nanoscale materials[150–152] with a resolution below the diffraction limit of the excitation wavelength. These breakthroughs and achievements in super-resolution imaging with fluorescent labels, as discussed in numerous reviews,[148,149] were honoured with the Nobel Prize in 2014. Some super-resolution methods, such as structured illumination microscopy (SIM)[153,154] and nearfield and tip-enhanced techniques,[155,156] are based on the manipulation of light used for excitation. Other methods based on stochastic techniques, such as STORM[157] and PALM,[158] require fluorescent species that switch between bright and dark states. Stimulated emission depletion (STED)[159] and related techniques require probes whose output can be manipulated with two beams, one used for excitation, and the second for depleting the population of emitting states *via* stimulated emission (Fig. 16a, left). However, the large excitation intensities required for these super-resolution imaging methods and/or the limited photostability of their fluorophores provide opportunities for the development of more robust sub-diffraction labels based on ANPs.

The need to finely control the optical properties of super-resolution fluorophores has led to the use of nanoparticles for super-resolution imaging.[150–152] In particular, lanthanide-doped nanoparticles have been successfully used as luminescent probes in several super-resolution microscopy techniques, including STED,[95] nonlinear structured illumination microscopy,[161] and near-infrared emission saturation nanoscopy.[162] These excellent demonstrations exploit the unique features of lanthanides, such as long luminescence lifetimes (facilitating depletion), perfect photostability and narrowband excitation end visible/NIR emission bands, with relatively low excitation/depletion power density thresholds and cheap and easily available CW light sources.

One of the first STED-inspired approaches for the application of lanthanide-doped nano labels was realized by Kolesov *et al.*,[163] where Pr^{3+}-doped YAG NPs were imaged with a system composed of two beams, a 609 nm pumping pulse and 532 nm depleting one, giving a spatial resolution of 50 nm for the image collected for UV emission. A different operating scheme for application of lanthanide-doped NPs for STED imaging was proposed by Liu *et al.*[95] In this realization, $NaYF_4$ nanocrystals co-doped with Yb^{3+} and Tm^{3+} were imaged with pumping with a 980 nm laser beam to observe an emission from the $^1D_2$ state, while an 808 nm donut-shaped beam was utilized for inducing stimulated emission ($^3H_4 \rightarrow {}^3H_6$ transition), and therefore depleting the emission from higher energetic levels. As a result, fluorescence imaging with a spatial resolution of 28 nm was achieved. A similar mechanism in Tm^{3+}-doped hosts was shown to give imaging resolutions of 50 nm for laser scanning through tens of micrometers thick tissue.[162]

Although STED-based techniques result in an impressive quality of direct super-resolution imaging, these methods still require rather complex dedicated optical systems operating with two concentric beams, one with a Gaussian profile and the other (depleting beam) characterized by a cylindrical donut shape. These two beams must also be properly synchronized in time to most effectively confine the point spread function of the STED microscope, which is not trivial when femtosecond pulses are used (Fig. 16a, left). In contrast, stochastic methods such as PALM and STORM are not necessarily demanding in terms of complex optical setup, but the sequence of excitation, acquisition, and analysis of fluorescence images at single-photon sensitivity is demanding for the photodetectors and requires significant computational power. From a user perspective, the need to computationally reconstruct images means that these images cannot be viewed and interpreted in real time during acquisition.

6.1.2 Multi-photon microscopy. In contrast to the complex setups of STED or computational reconstruction of stochastic techniques, the use of nonlinear fluorescent dyes has shown a relatively simple way to improve the optical resolution (Fig. 16c). Multi-photon microscopy exploits NIR photoexcitation to achieve visible fluorescence, which offers enhanced photoexcitation penetration into absorbing/scattering bio-samples. Although conceptually straightforward, 2-, 3-, and higher-photon microscopy generates weak fluorescence, and thus requires very sensitive photodetectors. However, only a limited number of dedicated (endogenous or exogenous) dyes is suitable for this type of photoexcitation.[164–166]

Extending the concept of using nonlinear materials for improving the optical resolution, Caillat *et al.*[167] proposed the

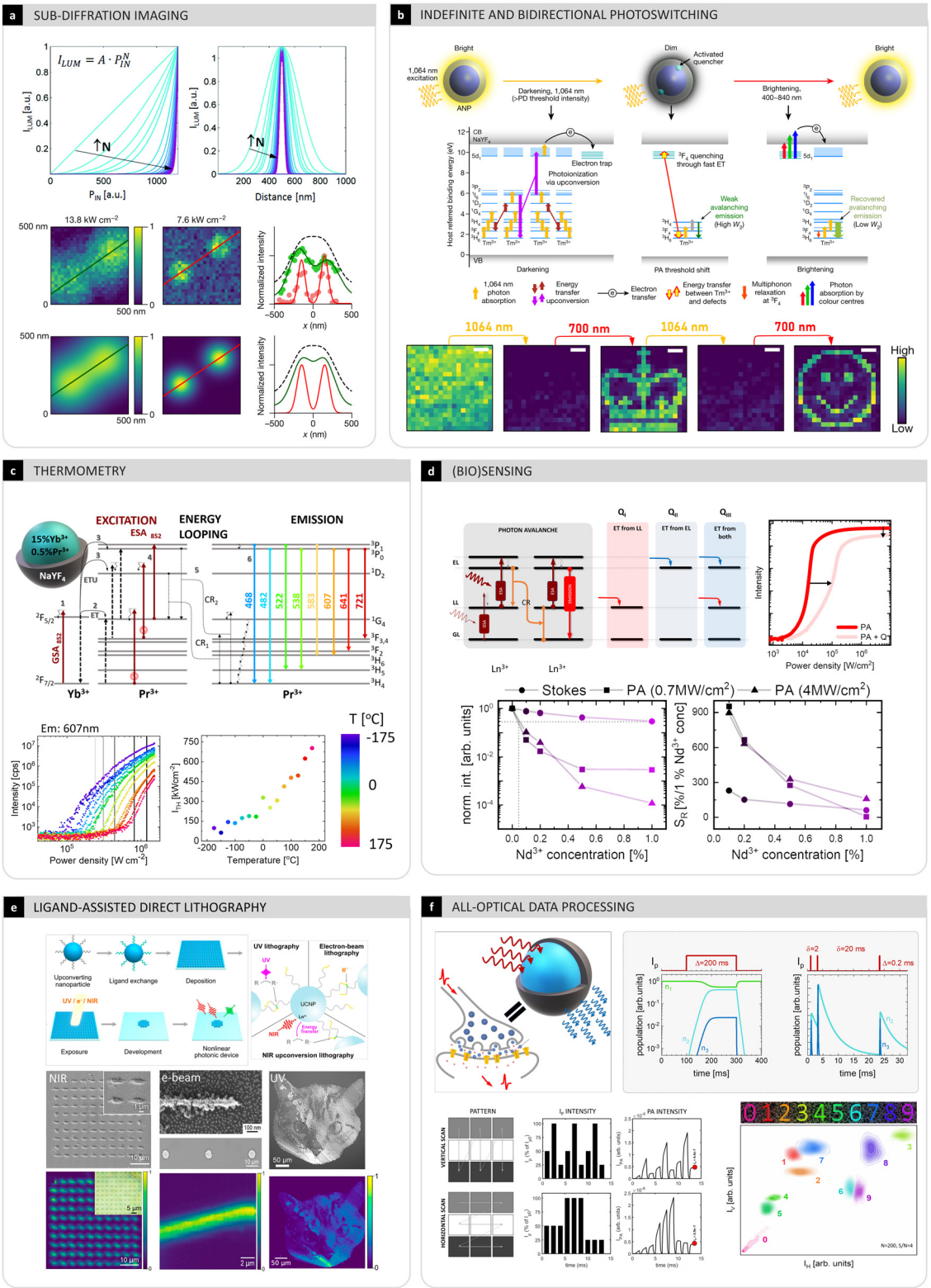

Fig. 15 Novel applications of PA (nano)materials. (a) Highly nonlinear pump power dependence enables a reduction in the effective point spread function volume and allows for sub-diffraction imaging of individual ANPs with single excitation raster scanned beam.[2,29] Reprinted with permission from ref. 29. Copyright 2019, the Royal Society of Chemistry. Reprinted with permission from ref. 2. Copyright 2021, Springer Nature. (b) Efficient energy looping and ESA may help reach high energy levels close to the conduction band of the host material and enable reversible, indefinite and bidirectional photo switching by changing the PA threshold.[146] Reprinted with permission from ref. 146. Copyright 2023, Springer Nature. (c) Positive energy loop is also susceptible to disruption of the energy looping due to changes in temperature and possibly other physical and chemical factors.[10,14] Reprinted with permission from ref. 14. Copyright 2023, AIP Publishing. (d) Positive energy looping within avalanching mechanism is extremely susceptible to quenching by either specific or unspecific quenchers, leading to disruption of both emitting and looping level, and consequently quenching of PA luminescence

being significantly more efficient than in the conventional Stokes photoluminescence mode.[12] Reprinted with permission from ref. 12. Copyright 2024, the Royal Society of Chemistry (https://creativecommons.org/licenses/by/3.0/). (e) By chemical functionalization of the surface of the UCNP, including also ANPs, with photosensitive ligands tending to agglomerate irradiated NCs, UV/NIR or e-beam lithography is possible.[147] Reprinted with permission from ref. 147. Copyright 2024, the American Chemical Society. (f) All optical data processing that mimics functioning of biological synapses; the slow kinetics of the ground (n_1), looping (n_2) and emitting (n_3) levels combined with ESA photoexcitation, lead to paired pulse facilitation and photoexcitation history dependence, which enables optical data analysis such as raster scanned image (*e.g.* of digits) feature extraction.[13] Reprinted with permission from ref. 13. Copyright 2023, John Wiley and Sons.

use of lanthanide-doped upconversion, and over a 2-fold resolution improvement was found for Yb^{3+},Tm^{3+} upconverting nanocrystals characterized with a nonlinearity order equal to $S = 4$. However, this value is the ultimate limit, given that the higher the upconversion order, the dimmer and more blue-shifted (into UV region) the lanthanide luminescence. Extending this concept for enhanced optical resolution was possible with photon avalanche, where high nonlinearity orders are enabled (Fig. 16a, right). Moreover, it is achieved without any blueshift in the emission band, in contrast to other multiphoton processes.

6.1.3 Photon avalanche single-beam super-resolution imaging. Despite the fact that photon avalanche emission still had not been demonstrated experimentally at the nanoscale, in 2019, we predicted theoretically[29] that using ANPs can offer similar results in terms of imaging resolution, similar to pure-STED approaches. The great advantage of ANPs is the ability to reduce the experimental setup to a typical confocal, raster-scanning microscope.[29] This idea originates from the nonlinear relationship (characteristic for PA-hosting materials) between the excitation power density and resulting fluorescence intensity. Thus, when raster-scanning across ANP samples with a diffraction limited Gaussian beam with a power density above the PA threshold it is possible to observe an emission point spread function (PSF) much narrower than the diffraction limit (Fig. 16c, right panels). This enhancement in resolution originates from the fact that, near the PA threshold (*i.e.*, with the highest nonlinearity/slope), minute changes in the excitation power density (in this case, changes in the local power density between the Gaussian wings and central part of Gaussian peak) lead to giant changes in the output intensity. According to the Abbe

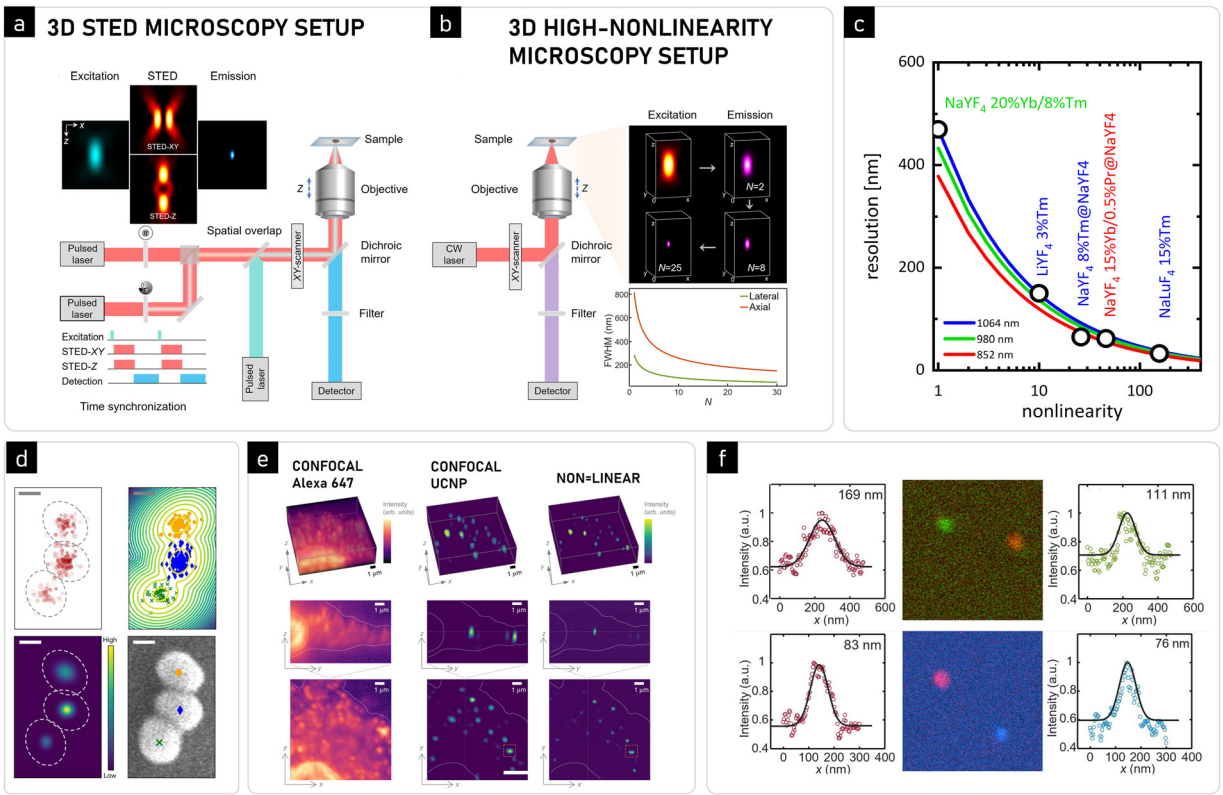

Fig. 16 Sub-diffraction imaging with avalanching nanoparticles. (a) Comparison of instrumentation required for conventional raster scanning STED (left) and (b) sub-diffraction imaging using highly nonlinear avalanching nanomaterials (right).[9] Reprinted with permission from ref. 9. Copyright 2024, Elsevier. (c) Resolution enhancement originating from highly non-linear emission ref. 28. (d) Photodarkening-based imaging of ANPs demonstrated 2 nm localization precision[146] (scale bar: 20 nm). Reprinted with permission from ref. 146. Copyright 2023, Springer Nature. (e) First demonstration of *in vitro* 3D sub-diffraction imaging with super-linear LnNP labels compared to confocal Stokes and UCNP-based imaging.[160] Adapted with permission from ref. 160. Copyright 2019, Springer Nature (https://creativecommons.org/licenses/by/4.0/). (f) Two colour photon avalanche single beam sub-diffraction imaging.[9] Reprinted with permission from ref. 9. Copyright 2024, Elsevier.

resolution equation adapted for nonlinear optics, the improvement in the resolution scales proportionally with $S^{-1/2}$, where S denotes the degree of nonlinearity of this process. Importantly, a resolution improvement appears not only in lateral scanning but also in the axial dimension. We also note that this implies that rather than breaking the resolution limit (*i.e.*, "super-resolution"), this nonlinear PA imaging simply shifts the resolution to a lower limit.

In recent years, several imaging methods have validated the theory of PA single-beam super-resolution imaging (PASSI).[2,3,6,9,142] Table S11 (ESI†) compares the previously demonstrated super-resolution imaging using lanthanide-doped nanoparticles with currently presented examples of PASSI imaging and its modifications. The first experimental realization of PASSI was the 2021 report by Lee *et al.*,[2] who used Tm^{3+}-doped ANPs with nonlinearities as high as 31 to achieve resolutions finer than 70 nm at 800 nm emission. Notably, these resolutions, which were 7.5-fold finer than the diffraction limit of the 1064 nm excitation, precisely match that calculated ones using the revised Abbe diffraction equation.[29] Later, in 2022, multicolour core–shell-shell migrating PA heterostructures with a reported 46th-order nonlinearity were used to label HeLa cells and image them with resolutions reported as high as 62 nm (Fig. 16d–f) at 550 nm ($NaGdF_4$:Yb/Pr (25/0.5%)@$NaGdF_4$:Yb/Tm (8/2%)@$NaGdF_4$:Tb (20%)@$NaYF_4$ ANPs) and 452 nm ($NaYF_4$:Yb/Pr (25/0.5%)@Yb, Tm(10/4%)@Yb/Pr (25/0.5%)@$NaYF_4$).[9] Recently, due to the extreme non-linearity of $S >$ 500, FWHM = 33 nm and 36 nm localization precision were achieved for a single, 27-nm diameter ANP.[28]

These experimental realizations of PASSI and subsequent reports are directly analogous to multi-photon microscopy methods, with the major difference being the ability of ANPs to realize the resolution enhancement of >30–500 photon processes with minimal anti-Stokes shift. Most importantly, these exquisite <30–100 nm resolutions were achieved with inexpensive, commonly available continuous wave lasers and standard confocal microscopes.[152,168] These advantages suggest that PASSI has the potential to democratize sub-diffraction-resolution imaging, although some challenges remain to be solved, such as the size of the ANP label compared to biological species, bio-functionalization, and corona formation around inorganic particles entering living tissues.

6.1.4 Photodarkening and photon avalanche localization microscopy. During the development of ANPs and PASSI, Lee *et al.*[169] made the surprising and confounding realization that unlike conventional UCNPs, which are known for their photostability, the emission intensity of ANPs would darken suddenly when they were excited at intensities far above their PA threshold (*e.g.*, 10^5 W cm^{-2} or >5 times their threshold power density). The mechanism of this photodarkening is postulated to originate from the efficient excitation of ANPs to high-energy excited states whose energy can initiate charge-transfer to defect states in the host matrix. These activated defects can accept energy from other excited Tm^{3+} ions, disrupting their PA/energy-looping processes and shifting their avalanching thresholds to significantly (from 10 to 40 kW cm^{-2}) higher power densities. Notably, this photodarkening is observed in other avalanching systems, such as migrating ANP heterostructures.[5] Critically, Lee *et al.*[146] discovered that higher energy light (400–840 nm) could be used to photobrighten Tm^{3+}-doped ANPs back to their original emission intensities, presumably by reversing the defect formation mechanism.

The ability to switch the bright and dark states of ANPs on demand is reminiscent of photoswitchable fluorophores used for stochastic localization microscopy techniques such as PALM and STORM. Lee *et al.*[146] identified power densities that stochastically photobrightened a sub-population of ANPs such that the centroid positions of individual ANPs could be localized without obfuscation from neighbouring ANPs (which were most likely dark). Due to the robustness of the photobrightening/photodarkening cycle of ANPs, the ANPs could be cycled indefinitely without permanent photobleaching. This indefinite cyclability of ANPs is a critical feature given that the accuracy of photon localization methods such as PALM scales inversely with the square root of the number of collected photons, which is the current limiting factor for the resolution of PALM and STORM. Lee *et al.* used repeated cycling and localization of ANPs to demonstrate indefinite photon avalanche localization microscopy (INPALM), exhibiting <1 Å localization accuracy even with ANPs that were touching (Fig. 16b).[146]

The ability to use the same Tm^{3+}-doped ANPs to achieve two different modes of sub-diffraction imaging (<70 nm resolution with PASSI, and <1 Å accuracy with INPALM) demonstrates the unique and powerful applications of PA nanomaterials.

6.2 Photon avalanche-based sensing and biosensing

One of the most promising applications of the PA phenomenon is imaging, diagnosis and sensing biological activity. Luminescent nanomaterials have found countless of applications in biosensing of proteins, DNA/RNA fragments, antigens, cell components, and eukaryotic/prokaryotic cells.[170–172] There are several requirements that should be satisfied by the given materials that are suitable for this type of utilization. Firstly, they should feature (intrinsic or biofunctionalized) biorecognition and biospecificity, and they should allow for remote optical probing using signals easy to distinguish from the background or tissue autofluorescence. These labels should additionally be non-toxic and small in size, given that their sensitivity is most often proportional to the surface-to-volume ratio. All of these requirements are, in first approximation, fulfilled by lanthanide-doped NPs, including ANPs. From a functional perspective, the biosensing capabilities are considered either biospecific passive labelling of the target objects (*e.g.* cells and cell structures, and proteins) or active sensing of the presence or concentration of the target moieties (*e.g.* proteins and DNA/RNA fragments). In the former case, the luminescent reporter is just a lantern, which is biofunctionalized to specifically anchor to these molecules and report about their presence and location. In the latter case, some specific optical response is expected from the luminescent reporters, such as a change in luminescence colour, intensity or luminescence kinetics.

6.2.1 Advantages of biological sensing with lanthanide-doped nanoparticles and ANPs. Ln^{3+}-doped nanoparticles generally exhibit low absorption (σ_{ABS}) and emission (σ_{EMI}) cross

sections due to the forbidden nature of the f–f transitions.[173] Therefore, searching for organic antenna or plasmonic enhancement remains an emerging field of research and optimisation.[174–177] Their luminescence is additionally affected by their small size, surface quenching (by ligands or solvents) and concentration quenching (by interaction between the Ln^{3+} ions). The size of the UCNPs or ANPs is a critical parameter for biosensing applications. On the one hand, a size below 10 nm diameter is achievable with current synthetic methods,[93,178] but should be considered quite large compared to other endogenous or exogenous molecules. On the other hand, these small NPs are usually dim because of the limited number of lanthanides per particle and large surface-to-volume ratio, which makes most of the lanthanide ions within these nanoparticles exposed to surface ligands and solvents. Despite the fact that lanthanides are in principle barely susceptible to the local chemical environment, their long lived real electronic states mean that lanthanides undergo effective MPR with numerous vibrations (*e.g.* –OH at *ca.* 3300 cm^{-1}) and overtones (Sections 3.2.2 and 4.4). Although the UC in Ln^{3+}-doped NPs is considered the most efficient anti-Stokes process of all known luminescent materials,[178] *i.e.*, much more efficient than 2-photon processes or harmonics generation, the absolute quantum yield of their emission is usually not larger than several percent[179] and rapidly decreases as UCNPs get smaller. Most importantly, in conventional Stokes or upconverting nanoparticles, the concentration of doping ions typically remains low (*ca.* 20% of sensitizing Yb^{3+} or Nd^{3+} ions, and no more than 2% for emitting activator ions). Conversely, in ANPs, where the excitation scheme exploits ESA, the emission increases with an increase in the concentration of dopants, which not only enhances the absorption coefficient, but also augments the energy looping, and thus the luminescence brightness. However, this phenomenon occurs at higher pump intensities than the conventional Stokes or anti-Stokes emission.

Lanthanide emission is perfectly photostable, which is considered one of the most important advantages of these labels and accounts for either Stokes, upconverting or avalanching nanoparticles. This is critical for biosensing capabilities, given that it not only enables the signal to be reliably acquired over longer dwell times to improve the photon budget at a significantly lower background, but most of all it enables long-term time lapse imaging to be performed over hours of continuous illumination. Although this possibility has not answered any serious biological questions to date (spreading of NPs in the blood stream, small organism development, *etc.*), these types of studies will definitely gain interest in the near future. Combining cellular component targeting with multiplexed labels and bio-sensing or super-resolution imaging, these novel luminescence labels may offer unprecedented tools for developmental biology or *in situ* continuous sensing.

In conventional Ln^{3+} luminescence, short-wavelength excitation beams are required, which simultaneously photoexcite organic fluorescent molecules, and thus increase the background.[180] The anti-Stokes emission in UCNPs diminish these problems, but to sensitize their upconversion, Yb^{3+} ions are used with an excitation wavelength at 980 nm, which matches the absorption spectrum of water, and thus may cause undesired sample heating. With the development of core–shell inorganic UCNP nanomaterials, the possibility to sensitize their upconversion with Nd^{3+} ions at *ca.* 800 nm excitation was demonstrated with efficiency and brightness comparable to excitation with Yb^{3+}, and less overheating.[181] Thus far, PA has been observed under a few excitation wavelengths in the visible and NIR (*e.g.*, 852 and 1064 nm) regions, which is promising for biomedical sensing. For example, PA was observed in Tm^{3+}-doped ANPs under biocompatible excitation at 1064 nm using power densities typical or smaller than in conventional confocal microscopes.[2] These high pump power densities are too high for wide-field imaging, but are acceptable for raster scanning and should not harm biological samples.

6.2.2 FRET sensors. The emission of lanthanides exhibits inherently weak susceptibility to the bio-chemical environment, owing to the shielding of optically active 4f electrons by 5s and 5p electrons in their outer electron orbitals. However, the population of excited states of the lanthanide emitters may be perturbed by a sufficiently short distance between quenchers/acceptors, which spectrally overlap these levels. This quenching is described by the well-known Förster-type resonant non-radiative energy transfer (FRET). The interaction between the donor and acceptor is evidenced by the appearance of the acceptor emission under donor pumping and a decrease in the donor emission intensity, which is also accompanied by shortening of the donor luminescence lifetimes.[182] Upconverted emission in lanthanides in first approximation is very advantageous, given that excitation wavelengths in the NIR region do not induce sample (*e.g.* tissue, cellular components) autofluorescence. The long luminescence lifetimes of lanthanides are also technically much easier to quantify. Therefore, many FRET-based sensing nano-platforms have been studied, where the UCNPs act as upconverting energy donors, and organic molecules (*e.g.* Rose Bengal) play the role of energy acceptors. However, the origin of the decreased donor emission and increased acceptor emission, combined the with weak luminescence lifetime dependence of the donor UCNPs, makes these UC-FRET tests unreliable, given that these phenomena may also be caused by reabsorption, and the observation thereof does not guarantee the biological specificity of the object attached on the surface of UCNPs. More frequently, UCNPs are used as luminescent labels (*e.g.* ELISA and lateral-flow assays), where the specific sensing is achieved by indirect physical methods and gained from improved signal-to-background ratio in UCNPs.

In contrast, PA emission should be susceptible to the presence of acceptor molecules in a spectacular manner[79] because a small perturbation to the energy looping should be evidenced by a significant perturbation to the photon avalanche emission. In this context, the PA does not change the physics of the dipole–dipole interaction between the donor and the acceptor but enables the quantification of minute FRET signals occurring at distances beyond 100 nm, where the FRET effectiveness drops down below 1% in conventional approaches. Moreover, the volume of the ANPs that interacts with acceptors would increase or the surface passivation (to protect ANPs from unspecific quenching from ligands) would favour the bio-specific response

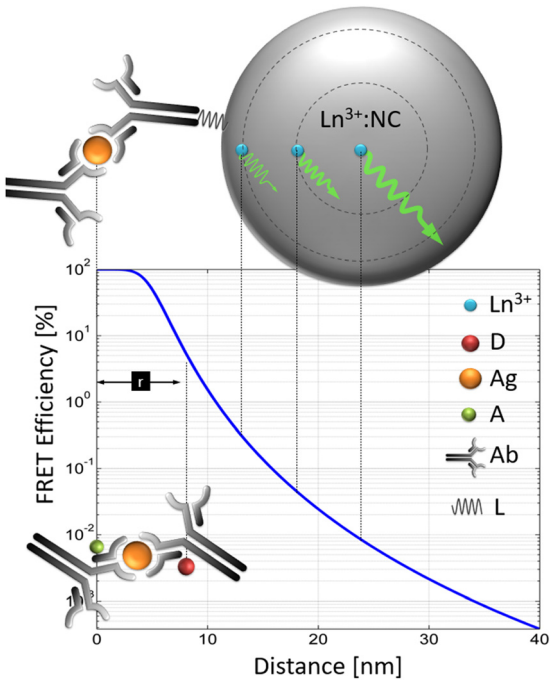

Fig. 17 Issues related to UC-FRET.[79] In molecular FRET, the resonant ET between the donor (D) and acceptor (A) occurs owing to the presence of an antigen. The FRET becomes enabled in carefully selected D and A moieties by a D–A distance (r_{DA}) of a few nanometers and spectral overlap of the D emission with A absorption. In upconverting nanoparticles, not only a single UCNP contains 100–1000 of donor lanthanide ions that participate in RET to multiple A molecules, but these individual D ions remain in statistically variable distance from the UCNP surface, where the A molecules can attach to. Obviously, this complicates the analysis. PA emission may become an alternative type of D nanoparticles, which will augment the FRET efficiency, enable surface passivation and biofunctionalization without compromising the FRET sensitivity. Adapted with permission from ref. 79. Copyright 2020, the Royal Society of Chemistry (https://creativecommons.org/licenses/by/3.0/).

of the ANPs to the presence of appropriate acceptors. This is in contrast to conventional UCNPs used for FRET sensing, where only superficial lanthanide dopants have a chance to interact with the acceptors (Fig. 17) and undergo surface passivation, although to improve the brightness, the acceptors need to be moved further away from the surface of the UCNPs and the donor lanthanides ions.

Although no PA-based biosensors have been experimentally demonstrated beyond simulations,[79] some progress has been made recently in understanding the susceptibility of the PA emission to the presence and concentration of PA quenchers (see Section 7.1.2).[12,80] These studies pave a way to develop PA transducers that can detect specific D–A interactions at increased length scales.

6.2.3 Exploiting PA for physical measurements – temperature sensing. Luminescence thermometry has become an accepted method to measure and map the local variations and distribution of temperature in many applications, where conventional methods, such as point contact thermocouples and remote bolometric 2D cameras, are not suitable. Examples of these applications include the use of thermometric phosphors for (i) high-resolution *in vitro* observations of living cells and sub-cellular structures through an optical microscope,[183] (ii) beneath the skin surface temperature monitoring, aiming for feedback controlled hyperthermia,[184] inflammation,[185] stroke,[169] and cancer[186] studies, and (iii) in technology for studying the temperature distributions in rotating mechanical components,[187] gas and liquids,[188] and catalysis.[189] Besides studying the absolute luminescence intensity, which is considered not very reliable to extract absolute temperature in turbid, scattering or absorbing media, most of the current technologies exploit either the luminescence intensity ratio at two emission wavelengths or luminescence lifetimes.[190–196] Although they have been proven to accurately determine and map temperature in specialized laboratories (*e.g.* using sophisticated microscopes with hyperspectral sensors, switchable filters or fast lasers and time-resolved detectors), they are often too slow or too complex for many other applications. For example, ratiometric imaging requires either hyperspectral tuneable filters, fixed 2 CCD cameras with appropriate bandpass filters or switching between filters in front of a single camera. Although the first two solutions are relatively fast but very expensive, the latter is cheaper but slow. Moreover, the dispersive dependence of light absorbance by the medium in which the phosphor is located or the medium in-between the phosphor and the detector may modify the shape of the luminescence spectrum, and thus falsify the temperature readout.[188,190–194,196–198]

PA performance is expected to be strongly affected by the temperature, resulting in a shift in the PA threshold and in variations of the nonlinearity of the emission (similarly to Fig. 15c).[10] These macroscale effects are a result of the complex interplay between opposite microscopic effects and especially in PA materials may modify the luminescence in a non-trivial way. Interestingly, in the case of PA materials, high temperature relative sensitivity, S_R, was predicted between 4% K^{-1} and over 35% K^{-1}, with a useful temperature range (where $S_R > 1\%\ K^{-1}$) of *ca.* 150 K. Moreover, the range with the highest sensitivity may be tuned by the selection of the pump power used for probing. Optimizing the system for higher sensitivity ranges results in limited temperature useful regions. As a result, two opposite effects can be observed. On the one hand, the capability to select a particular calibration curve ($T = I_L^{-1}$ (T)) tailored for the expected sensitivity and broadest temperature sensitivity range provides the unique ability to dynamically adjust the optical thermometry performance for the given utilization and for its specific requests. Nevertheless, this effect should most probably limit the practical application of PA luminescence thermometry of these materials due to the necessary use of a matrix of pump power and temperature-dependent calibration curves. The other limitation in the utilizing of these types of materials in thermometry is their thermal stability and thermal decomposition at >580 K.[199] Other effects, such as nanoscale effects, presence of ligands and solvents (discussed in Section 4.4), as well the presence of quenchers (discussed in Section 6.2.2), will further make the PA susceptible to the external chemical environment. Thus, the understanding and proper management of these factors are critical for the further development of new PA nanomaterials and their applications.

Therefore, alternative luminescent thermometers and reliable methods for temperature-dependent spectral properties quantification are sought, and the PA concept may offer new possibilities (Fig. 3b). In this case, the so-called single-band ratiometric (SBR) approach,[200–203] the luminescence intensity of a single emission band can be monitored under two, ground and excited-state absorption photoexcitation lines. This approach is advantageous given that it is technically less challenging and cheaper to all-electronically switch between 2 laser/LED light sources and record two (GSA and ESA based) images within a single spectral channel than the opposite of recording two spectral images under a single photoexcitation line. Additionally, by using the same spectral range of emission, the risk of disturbing the temperature readout due to the influence of the medium will be eliminated. The unique configuration of the 4f energy levels of Ln^{3+} opens a wide variety of different ions for which the ESA process can be observed. The former, temperature-dependent ESA-based thermometry has been recently proposed and studied in Nd^{3+}, Eu^{3+}, Tb^{3+}- and Pr^{3+}-doped nanoparticles[204–207] In the case of materials with thermal coupling between the ground and excited states, they enable an enhancement in the ESA-excited luminescence by an increase in the population of the upper energetic state according to the Boltzmann distribution. However, versatile studies enabled the understanding that the interionic interactions, usually *via* the CR process, lead to boosting of the thermal response of the luminescence signal. Therefore, the optimization of the dopant concentration has led to the development of luminescent thermometers with sensitivity to temperature changes as high as $>10\%\ K^{-1}$. Although the probability of the CR process is temperature independent, the splitting energy of the particular 4f multiplets involved in this process may shift the CR process out of resonance. Therefore, the assistance of phonons will lead to the strong thermal dependence of the CR process (see Section 3.2.2). Given that the splitting energy of the 4f levels is dependent on the crystal field strength of the host material, by deliberate selection of the host material stoichiometry, the probability of this process can be modified. Considering the essential dependence of the PA process probability on the CR performance, the sensitivity of luminescent thermometers using photon avalanching nanoparticles will be unprecedently high and should definitely exceed the values reported thus far for thermometers based on the ESA/GSA SBR approach.[208,209] The relative sensitivity of PA-based luminescent thermometers reaching tens of $\%\ K^{-1}$ in a broad and tuneable (by tuning the excitation power) temperature range was predicted recently with the numerical simulations employing the phenomenological model of an avalanching system.[10]

Beside technical issues, metrology factors are also important and the two emission wavelengths (in traditional ratiometric imaging) or the two excitation wavelengths (in ESA/GSA thermometry concept) may be affected by the sample in different ways, which is strongly related to the sample spectral properties (*e.g.* dispersive tissue absorption and scattering coefficients).[209] These aspects are difficult to predict, given that the sample-to-sample and patient-to-patient variability may hinder simple external temperature calibration.[203,209] A solution can be offered by the temperature-dependent kinetics of the luminescence rise or decay times. In the case of luminescence decay, various luminescent compounds have been proposed, whose lifetimes are typically shortened with an increase in temperature due to thermal quenching. However, in the case of thermal imaging, the acquisition time needs to be shorter than the decay itself. Therefore, the shortening of the decay observed at elevated temperatures may affect the number of photons absorbed, and thus the reliability of the temperature estimation. On the other hand, in case of the PA process, for the threshold conditions (excitation density and temperature), the rise time is extended. Therefore, kinetic-based thermometry may beneficially influence the signal-to-noise ratio by facilitating a reliable temperature measurement. Although this approach has not been confirmed experimentally to date, its applicative potential for remote temperature determination from the theoretical perspective is indubitably appealing.

As can be noted in Fig. 3b, temperature may contribute to the PA emission by enhancing the population of the starting level. An educated guess leads to the conclusion that an increase in temperature should reduce the PA threshold, but due to the rich energy level scheme of most lanthanides, temperature may also negatively impact the PA emission, leading to thermal quenching by enhancing multiphonon relaxation rates.[10] Moreover, the rise times of luminescence under PA photoexcitation and looping conditions is not only affected by temperature, but also dependent on the excitation intensity, I_{EXC}, and due to the sample properties, I_{EXC} is actually difficult to be determined. Therefore, the latter features may hinder the practical implementation of PA-based thermometry at the nanoscale in 'difficult' environments, such as absorbing and scattering samples (*e.g.* tissue and cells).

The fact that a slight change in temperature can affect both the spectral broadening of the absorption bands and the activation of energy bridging the CR processes means that even a small change in temperature can cause rapid (up to a dozen or even orders of magnitude) changes in the intensity of luminescence. In this case, the expected rapid changes in thermometric parameters should take place in a narrow temperature range. However, a wide range of possibilities of selecting the appropriate energy levels and activating various physical processes through the appropriate selection of the luminescent host material and Ln^{3+} admixture ions offered by the unique configuration of the 4f energy levels can enable the design of a wide range of supersensitive luminescence thermometers/manometers based on the PA process, whose operating range can cover a wide range of temperatures/pressures. A necessary but not sufficient condition for the occurrence of the PA phenomenon is an efficient ESA process. The first attempts to create luminescence thermometers using the ESA process in nanocrystals, glasses and microcrystalline materials doped with lanthanide ions such as Nd^{3+}, Pr^{3+}, Tb^{3+}, and Eu^{3+} confirmed the high potential of this type of materials for remote temperature reading, which was confirmed by the sensitivity of nearly $15\%\ K^{-1}$. Moreover, the favourable role of CR processes on the variability in temperature parameters was confirmed, which indicates that for the conditions required for the occurrence of PA, high relative sensitivities will be obtained.

A limitation of this type of thermometer may be the fact that it will be necessary to provide a reference signal enabling a ratiometric temperature reading. This can be done using the SBR approach, which due to the need to change the wavelength, may cause some experimental difficulties. Another possibility is the use of the emission band of the co-dopant ion, for which the excitation wavelength used to initiate the PA process, allowing luminescence to be obtained by GSA. This concept has been proposed for ESA/GSA processes but is unpopulated for the PA process thus far. This is because interionic interactions can disturb the equilibrium conditions for PA occurrence. Nevertheless, the appropriate selection of dopant ions and the optimization of their concentration may enable the creation of this type of thermometer in the future. The undoubtful profits coming from the utilization of PA-based luminescence thermometry resulting in the achievements of the nano-spatial and 10^{-3} K thermal resolution of thermal imaging are sufficient motivation, initiating research studies devoted to this in the near future.

Thus far, beside homogenous temperature-dependent PA studies (Fig. 15c)[14,203,209,210] and theoretical modelling of temperature dependence of PA emission,[10] no experimental evidence of temperature quantification at the single ANP level has been demonstrated.

6.2.4 Exploiting PA for physical measurements – force sensing. In addition to temperature, excitation history, and quencher moieties, applied force also strongly affects the emission of ANPs.[211] Mechanical force induces atomic-scale changes in the crystal structure of ANPs, shortening or modifying the distance between the lanthanide ions taking part in the PA and leading to effects analgous to those observed when increasing dopant concentrations (Fig. 18a). Moreover, mechanical forces, may modify energy level splittings and also lead to an increase in the energy of the vibrational modes. This results in higher nonradiative rates and quenching.

The application of PA to force sensing was demonstrated in experiments where Tm^{3+}-doped NCs were studied spectroscopically with forces applied *in situ* using an atomic force microscope tip. Importantly, the impact of the force on the emission varied with the doping concertation of the NPs under study. In the case of ANPs doped with 4.5–8% of Tm^{3+} ions, for which the full-performance PA is observed in a single ANP ($\phi \sim 25$ nm), applying force (from the hundreds of pN to few μN range) resulted in a shift in the power dependence curve towards higher values (Fig. 18b). This enables force sensing based on the luminescence intensity from a single ANP. Alternatively, reducing the doping concentration (to 4%) results in 'pre-avalanching' nanoparticles that exhibit energy looping but not the steep emission intensity rise characteristic for PA. In such pre-ANPs (Fig. 18c), applied mechanical force and reduction in the average distances between the photoactive ions in the NCs pushes these nanoparticles into the avalanching regime, resulting in much brighter luminescence. In a third force-sensing modality, much heavier doping (15%) enables remote force sensing based on the modulation of emission peak ratios with force, known as mechano- or piezochromism. This approach has been demonstrated with the emission from

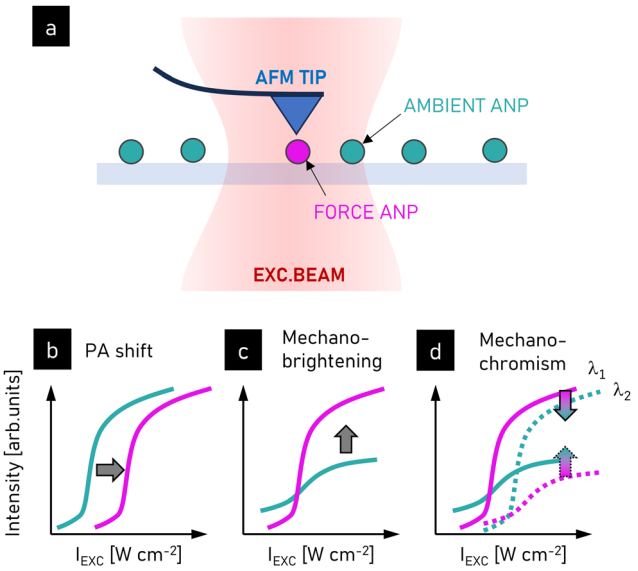

Fig. 18 Photon avalanche-based force sensing. (a) Scheme of the experiment, measurement of the impact of the mechanic force applied by an atomic force microscope tip on avalanche emission of single ANPs; (b) force-induced shifting of the power dependence observed for ANPs (doped with 4.5–8% of Tm^{3+}); (c) force-induced avalanching of pre-ANPs (doped with 4% of Tm^{3+}); and (d) mechano-chromic effect observed for piezo-chromic ANPs (doped with 15% of Tm^{3+}).[211] Adapted with permission from ref. 211 (https://creativecommons.org/licenses/by/4.0/).

two Tm^{3+} energy levels ($^3F_{2,3}$ and $^3H_4$), whose relative intensities respond differently to applied mechanical force (Fig. 18d). It is believed that a force-induced increase in the nonradiative rates results in the relaxation of energy from the higher level ($^3F_{2,3}$, emission at 700 nm) to the lower one ($^3H_4$, emission at 800 nm). This enables sensing of forces with single digit nN resolution.

6.3 All-optical computing and data storage

The switching properties of ANPs[146,212] also provide a path towards optical computing and data storage, as a valuable alternative to microelectronics, which are approaching their physical limits in terms of the size of transistors, heat dissipation, and dielectric breakdown. In optical computing devices, input data are delivered remotely (with no physical wires) and coded as the modulation of light (*e.g.*, its intensity or phase). The output data are also read remotely, which so far has hindered the concatenation of data to the inputs of subsequent processing units. The main advantage of optical computing is its fast and possibly massively parallel operation with high energy efficiency and critically reduced heating. However, it still is problematic to integrate optical computing devices with other functional blocks, such as electronic input–output blocks and memory units. One of the leading approaches is based on waveguide systems composed of Mach-Zehnder interferometer units, in which the phase-sensitive interference of the beams enables the desired operation.[213] However, the recent advances in ANPs open a new field of applications for lanthanide-doped materials in all-optical data processing[13] and memory effects.[146,214]

6.3.1 Optical storage

6.3.1.1 Non-volatile memory. ANPs have demonstrated two different modes of switching, which provide avenues for the long- and short-term optical storage of information. The defect-based switching reported by Lee *et al.*[146] allows long-term information coding through photoswitching into persistent photodarkening or photobrightened states. Although appropriate optical stimulation of PA materials is needed to induce reversible switching between the two physically distinct bright and dark states, optical pumping is not needed to maintain these states. Thus, Tm^{3+}-doped ANPs have been utilized for persistent non-volatile storage, akin to phase change materials in Blu-ray discs. Lee *et al.*[146] illustrated the ability to write, erase, and rewrite two- and three-dimensional patterns of bits in films of Tm^{3+}-doped ANPs. These write/rewrite cycles have been repeated over 1000 cycles for a single bit, demonstrating the robustness of ANPs for optical storage. The sub-diffraction spot sizes afforded by the giant nonlinearity of PA also suggest that bits smaller than 70 nm can be written in films of ANPs. In fact, photo-switchable ANP memory devices have been patterned by switching the solubility of ANPs through the use of photoactive ligands that can cross-link or undergo redox reactions when stimulated with UV, NIR, or electron-beam radiation. Pan *et al.*[147] demonstrated the patterning of features as small as 100 nm and photoswitching of 5 μm patterned arrays of Tm^{3+}-doped $NaYF_4$ ANP memory devices. This reversible optical storage of information can be used in optoelectronics for optical control of the system properties. It also has the capability for long-term volumetric addressable data storage option in all-optical signal processing systems.

6.3.1.2 Volatile memory. In contrast to the persistent storage of photodarkened/photobrightened Tm^{3+}-doped ANPs, Skripka *et al.*[212] demonstrated an orthogonal optical storage method based on the intrinsic optical bistability (IOB) of Nd^{3+}-doped KPb_2Cl_5 ANPs at low temperature. In this IOB phenomenon, the ANPs having two discrete stable luminescence states (dark and bright) that could be treated as logical 0 and 1 bits, respectively. Unlike Tm^{3+}-doped ANPs, whose bright and dark states are physically distinct, bright and dark IOB ANPs have an identical physical structure and operate under identical excitation conditions. The only difference between the two bistable states is their excited state populations, which are distinct due to their differing excitation histories. Skripka *et al.* observed hysteresis in the power-dependent luminescence of Nd^{3+}-doped KPb_2Cl_5 ANPs, similar to that exhibited by magnetic domains. The dark state was observed before the PA threshold, while the bright state appeared when the intensity of the 1064 nm laser exceeded a power threshold associated with the initiation of PA, which exhibited nonlinearities of $S > 200$ at 77 K. Importantly, when the power was subsequently reduced to intermediate levels, the bright state was still maintained; thus, luminescence, or logical 1, may be read out at powers lower than that required to write it. Thus, the history dependence, or hysteresis, of ANPs allows them to store the optically encoded information. Notably, the bright state and all the stored information disappear below a power threshold lower than the PA threshold observed during power ramp up. Given that the minimum excitation power must be maintained, this IOB-storage is analogous to volatile memory.

6.3.2 Optical transistors.

Due to the significant difference in the luminescence intensity for a pumping intensity below and above the PA threshold, PA is ideally suited for high S/N optical AND gates. Either 2 and multiple input AND gates have been proposed.[13] Unfortunately, for complex binary operations, the ability to perform AND gate functionality should be supplemented with other gates such as XOR, OR and NOT. Although some progress has been achieved in multiple optical gate design using lanthanides, data addressability and homogeneity, as well as the very basic data cascadability observed,[215,216] numerous and serious technical challenges still need to be addressed before any complex binary operation can be performed with ANPs in the optical domain.

Besides non-volatile memory, the photoswitching properties of Nd^{3+}-doped KPb_2Cl_5 ANPs have been leveraged as prototype optical transistors. Skripka *et al.* demonstrated the ability of these bistable ANPs to move between their dark and bright states without changing the intensity of the 1064 nm pump laser.[212] A low-power (<100 nW) 808 nm laser pulse was used to cross the instability region that separates the bright and dark states of these ANPs at intermediate powers (thereby creating the hysteresis). This instability crossing switched the ANP emission from a dark to bright state, with the latter maintained by the continuously applied 1064 nm bias. In this configuration, many ANPs may be excited with a diffusely spread 1064 nm laser and flipped from a dark to a bright state by raster scanning with an 808 nm laser in any arbitrary pattern. This low-power, fast, and flexible photoswitching is particularly attractive in developing all-optical processors, memory, and interconnects, although advances in these IOB nanomaterials are needed to increase their operating temperatures to ambient conditions.

6.3.3 Artificial synapses and reservoir computing.

Recently, data processing has been also demonstrated with PA materials, which due to the fact that their luminescence dynamics are dependent on the oddment population of the looping level, show interest in reservoir computing.[13] In contrast to binary operation, avalanche optical computing mimics the function of the synapses, where data are provided as identical pulses, and the information about the amplitude or weight of the stimulus is coded by the frequency of these pulses (Fig. 15f).

This application leverages the photoexcitation history dependence, which can be especially pronounced in PA given that it is severely dependent on the initial population of the looping level. In a simplified perspective, to observe PA emission, a certain seed population of the looping level must be established through processes of GSA and ESA. A larger level population is facilitated by significantly longer lifetimes, typically in the order of tens of milliseconds,[6] in contrast to other levels with decay times measured in the tens to hundreds of microsecond range. Although the emitting level exhibits short electron lifetimes and can be depopulated easily through both radiative and non-radiative relaxation, as well as other non-radiative processes such as ET, the looping level may retain a

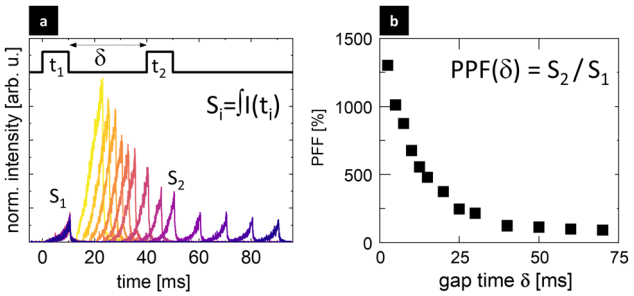

Fig. 19 Complex nature of luminescence originating from the multiple level and multiple dopant interactions in PA mode, where ESA absorption depends on the residual population of the looping level (n_2), and thus, two subsequent excitation pulses (a) induce a pulse-gap dependent emission and the so-called (b) paired-pulse signal facilitation (PPF).[13] Adapted with permission from.[13] Copyright 2023, John Wiley and Sons (https://creativecommons.org/licenses/by/4.0/).

residual population even after a few tens of ms. This long-lived population of the looping level can be likened to a form of system short-term memory. By exciting the PA material with a pulsed light source, with a time gap between the pulses smaller than the lifetime of the looping level, one can observe that the emission is dependent on the train of photo-excitation subsequent pulses, and the first pulse facilitates the emission achieved in the course of the second and subsequent pulses (Fig. 19). The facilitation effect stems from the fact that with the first few pulses, the looping level electron seed population is established, and the subsequent pulses start with non-zero population and contribute to further population growth, which enhances the emission intensity with each subsequent pulse (Fig. 19). The intensity of this emission, which is dependent on the photoexcitation history, can be controlled *in situ* by adjusting the pulse frequency, pulse and gap duration, and pulse power.[13]

This memory-like behaviour of PA resembles the operational principles of biological synapses, given that it demonstrates *in situ* plasticity, inherent short-term memory, and signal facilitation across multiple subsequent pulses. This similarity of the observed behaviour of PA upon pulsed excitation to neural circuits holds particular interest from the perspective of all-optical, training-free, reservoir computing, an alternative computational paradigm aiming to mimic brain function, to reduce the computation time and energy consumption in analysing temporal signals. Additionally, owing to their short memory and high nonlinearity, PA materials can function as optical, analogue AND logic gates with multiple optical inputs.[13]

There are also other characteristic features of the synaptic operation that have been evidenced, *i.e.*, the threshold intensity of the stimulus below which it is neglected, as well as the paired pulse facilitation effect. Both of these features match the characteristics of avalanching materials. One of the required features thereof is a metastable long-living intermediate energy level, given that the $^3H_4$ level in Tm^{3+} is characterized with a lifetime of around 16 ms,[6,13] which is much longer compared to the lifetimes of the levels from where avalanche emission occurs. One of the imminent features of the avalanching is slowing down of the intensity rise dynamics for excitation powers close to the PA threshold. However, the presence of the oddment population in the metastable level at the beginning of illumination leads to a significant reduction in the rise time required to achieve a steady-state emission intensity. Thus, during pulsed excitation with time gaps between the pulses comparable in duration to the lifetime of the metastable level, at the beginning of each of the consecutive pulses, the starting population in the metastable level is a bit higher compared to the previous one, facilitating faster build-up of the emission intensity and providing an increased population of metastable level for the next pulse. This effect can be understood as the short-term (on the timescale of the lifetime of the metastable level, up to tens of milliseconds, typically) memory required for the realization of the paired pulse facilitation effect, in which the response to the stimulus appearing shortly after former stimulus will be enhanced.

This effect, with operation at some points similar to that found in natural synaptic systems, allows all-optical data processing.[13] This includes pulse counting enabled by the short-memory effect caused by maintaining the oddment population in the intermediate state of the avalanching system between the pulses. Thus, for each next pulse, the response from the system (emission intensity) depends on the number of these pulses. However, this effect may be further developed by adding additional parameters modulating the rise dynamics of the avalanche emission. In general, this dynamic not only depends on the frequency of the pulses and their duration and width, but also on the sequence of these parameter changes. This sensitivity to the excitation history opens other fields of application, including pattern recognition, features amplification or extraction, and phase-sensitive detection.[13]

7. Outlook and perspectives

PA emission is indeed a spectacular luminescence phenomenon. The unique features of lanthanide ions, including multiple, long-living real electronic levels with multiple up- and down energy transitions and exchange, fulfils sophisticated conditions to let PA occur in bulk, micro, and down to nanoscale materials. The highly nonlinear response of the luminescence intensity to the pumping intensities and factors such as the history of photoexcitation, the presence and strength of numerous physical and chemical factors open new possibilities for further scientific discoveries and promise an implementation in all-optical metrology, sensing, imaging and data processing. However, to further advance the applicability of these PA materials, additional studies are needed in several areas.

Although the discovery of the PA phenomenon was the result of serendipity, actual progress in the intentional development of PA materials was triggered by understanding the fundamental differences between UC and PA and the shift in paradigms such as an increase in the concentration of the dopants (against conventional thinking about concentration quenching in lanthanide-doped phosphors) and the positive role of energy CR.

Therefore, despite their many similarities, these new PA (nano)-materials require *de novo* optimization of their composition. Obviously, the developments in PA materials stem from the last two decades of intensive progress and optimization of upconverted materials and technology. The most prominent contributions of UCNP to ANP technology are as follows: (i) the existence of reliable protocols for the synthesis of colloidal nanoparticles, (ii) ligand stabilization of individual nanoparticles, (iii) understanding the surface quenching mechanisms and (iv) clustering of dopants, resulting in great interest in single nanoparticle studies and further enabling the development of core-multiple-shell designs. Concerning core–shell nanoparticles, surface passivation with undoped homo- or heterogeneous shells was the key technology enabling the practical implementation of UCNPs in biosensing and bioimaging. Another great step forward was the studies dedicated to a compositional architecture, *i.e.* intentionally doped core and individual shell layers with various compositions of co-dopants, which enabled the engineering of the luminescent properties of these nanoparticles on demand. These fundamental achievements will further stimulate work and discoveries related to interfacial energy migration and lead to improved control of the luminescence colour and lifetimes of PA nanomaterials.

7.1 Current challenges in PA research on the nanoscale

Depending on the driving force of a particular application, skillful optimization of PA materials must be considered. Whether this is a lower PA threshold, higher PA gain range, either smooth or step-like transition from PA to saturation regime, photostability or susceptibility to energy trapping (photodarkening), all these scenarios and requirements may require various and maybe sometimes contradictory solutions. In this view, PA definitely needs many fundamental, experimental and theoretical studies aiming to understand the role of individual (chemical and physical) factors on the PA performance.[4,6,80] Because the PA phenomenon 'encloses' multiparameter dependent non-ground state absorption and energy circulation within a continuous positive loop, it will be enormously sensitive to numerous factors and processes that disrupt this machinery.[12] The examples include the impact of the concentration of dopants on the balance between (positive) energy looping and energy migration, the impact of MPR (stemming from temperature, crystal field, and phonons) on the energy redistribution (*i.e.* emptying or populating-required energy levels) or external factors such as temperature, pressure and electric/magnetic field as a few properties or features. These properties will not only affect the possibility to achieve PA emission characteristic features, but will determine the brightness, nonlinearity, PA gain range and lifetime of the looping level, which will define the possible scope of future applications.

7.1.1 Increased frame-rate sub-diffraction imaging. The use of ANPs can be highly beneficial in the field of high or sub-diffraction-resolution imaging and bioimaging, given that their application as luminescent probes enables imaging procedures to be performed using regular confocal fluorescence microscopy setups operating with a single Gaussian beam. The important advantages of lanthanide-doped luminescent labels and ANPs in particular, include perfect photostability and narrow-band, efficient NIR/anti-Stokes emission for background-free detection. Importantly, no further extension with costly setup is needed, and the only requirements are laser sources emitting lines corresponding to the selected ESA pumping schemes of the desired dopants and producing stable excitation power densities fitting the PA-regime in power-dependence characteristics. In contrast, other similar super-resolution imaging techniques, such as STED, requires a dedicated and complex precisely synchronized dual-beam setup to carry out the imaging process. Therefore, the use of ANPs can make imaging below the diffraction limit much more accessible and establish this approach as a standard research procedure in many laboratories working in the field of biology, biochemistry, biomedicine and materials science, especially when long observation time-lapse experiments are needed. Alternatively, it has been shown that both approaches, STED-like and based on PA or similar energy looping schemes, are characterized by different ranges of applicability. Furthermore, the combination of both techniques simultaneously was found to be highly beneficial and provided an even better performance.[160] However, to ensure the reasonable flexibility of this approach to easily fit the specific requirements of each of these fields of possible application, the development of well-defined and reproducible protocols of ANP design is highly required. This includes both the synthesis of small (currently ANPs are *ca.* 20–25 nm in diameter) ANPs doped with a range of dopants, providing an extensive library of possible combinations of pumping schemes and spectral ranges of outputs, as well as methods for surface modification with ligands to ensure specific attachment to the species intended to image as well as non-toxicity.

Because of the slow rise time of PA emission, some technological aspects must be also developed, such as pre-pumping (to speed up the raster scanning) and parallelization of multiple excitation spots (to image and localize ANPs in many areas simultaneously) similar to localization microscopy or Nipkow-disk approaches.[217] Optimization, *i.e.* shortening of the PA emission rise time, is another way to circumvent the slow frame rates of current PASSI-type imaging.[3,28]

Moreover, PA sensitization with Yb^{3+} co-doping can potentially be beneficial to improve the brightness and reduce the PA threshold and rise times of ANPs. The use of Yb^{3+} ions enables connotation with core–shell nanomaterials, where the Yb^{3+} ions are responsible for the energy migration between the absorbing core and emissive shell, which can potentially increase the number of available PA colours, aiming to perform multiplexed bio-detection or bio-imaging.

7.1.2 Understanding the quenching mechanisms in photon avalanche materials. In nanomaterials, it is impossible to neglect the effects occurring at the surface of nanoparticles because a significant percentage of lanthanide ions becomes exposed to the surface including crystallographic defects, surface ligands, and solvent molecules (Fig. 11). Fig. 20 compares simplified schemes for conventional luminescence (under GSA) (Fig. 20a) and PA upconversion (under ESA) (Fig. 20b), whose excited emitting level (3) or looping level (2) overlaps spectrally with the absorption of the acceptor (or quencher in general). In

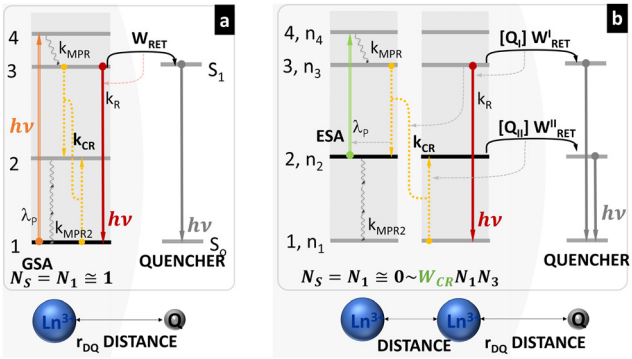

Fig. 20 Impact of donor–acceptor ET on luminescence. Simplified schemes of quenching of conventional luminescence (a) and photon avalanche upconversion (b). The color arrows indicate GSA (orange arrow) and ESA (green arrow) excitation, looping (yellowish), emission (red), D–A RET quenching. For PA scheme, either the emitting level (mechanism Q_I) or looping level (mechanism Q_{II}) can be quenched, which both affect the cross-relaxation, energy looping and PA emission.

the conventional GSA situation, resonant energy transfer (RET) occurs between the molecular donor and molecular acceptor, which is well known as FRET. In the situation discussed here, avalanche nanoparticles (ANPs) contain hundreds to thousands of dopant ions within a single nanoparticle (*ca.* 10–20 nm diameter), whose surface is additionally passivated with a *ca.* 3–4 nm thick undoped shell. However, for the sake of simplicity, we assume that RET occurs between a pair of PA ions and an individual quencher (Q).

In the case of conventional luminescence, the presence of Q reduces the emission output of the donor (D) (I_{DQ}) and shortens the luminescence lifetime of the donor (t_{DQ}) compared to bare donor (I_D and t_D, respectively) proportionally to the D–Q distance, r_{D-Q}, which can be quantified using the well-known Förster relations and theory.[182] In contrast to RET occurring in the conventional photoexcitation scheme (Fig. 20a), for the PA process, the presence of Q may affect the emitting (n_3), looping (n_2), or both levels, while both levels participate in the energy looping and ESA. In mechanism I (Q_I), the quenching occurs to the emitting level, which cannot participate in the CR with neighbouring ions in the ground state. In mechanism II (Q_{II}), the quenching occurs to the looping level, which hinders ESA. These two mechanisms should affect the PA features in different manners.[12]

The impact of the quencher on the emitting level has been theoretically considered by Bednarkiewicz *et al.*[79] The impact of the acceptor was defined as the relative ratio of W_{RET} to the CR rate, W_{CR}, existing in an unperturbed PA system. Next, the steady-state luminescence ratio Ω_{SS} of D accompanied by the acceptor, which is related to the luminescence intensity of the donor alone, was defined as $\Omega_{SS}(r,[Q]) = \frac{I_{DQ}}{I_D}$, enabling the quantification of how the PA emission reacts to an increase in the D–Q effectiveness when assuming that the FRET mechanism (R_0 = 5 nm) is responsible for this ET distance. These simulations indicated the significant susceptibility of the PA emission intensity to perturbations introduced by the quenching species, and consequently it was hypothesized that the interaction distance between D and Q can be extended by a few-fold (2–6) beyond the conventional Förster distance. To some extent, these simulations have been recently confirmed experimentally by studies devoted to unspecific quenching[80] and by cooping the Nd^{3+} quencher in the avalanching Tm^{3+} ions.[12]

The unspecific surface quenching has been demonstrated and modelled at the single-nanocrystal level to uncover the design-dependent heterogeneity in the ANP threshold intensity.[80] The 8%Tm^{3+}-doped $NaYF_4$ core of the R_c radius was passivated by the undoped $NaYF_4$ shell with a variable thickness (from *ca.* 3 to *ca.* 9 nm). As expected, a correlation was found between the mean threshold pump power and the ANP shell thickness ($d \pm \delta$, where δ is the standard deviation of the shell thickness) up to *ca.* 9 nm, beyond which the ANP behaviour did not depend on the 'unspecific' ligand field anymore. It was found that when the CR rate is large, the total depopulation rate, $A_2 + k_2$, of the first excited $^3F_4$ level in Tm^{3+} is proportional to the product of the PA pump threshold and ESA cross-section. Interestingly, the non-radiative quenching through the surface (k_2) was well described by the surface-quenching model, *i.e.* k_2 was found to be dependent on $e^{-\kappa(d\pm\delta)}\left(\frac{R_c + d \pm \delta}{R_c}\right)^2$, where κ [nm^{-1}] is the exponential passivation improvement with shell thickness (Fig. 21a and b).[218] FRET theory was considered in this work; however, it provided less accurate results compared to the surface-quenching model, which most probably originates from the differences between the specific (FRET) and non-specific quenching.

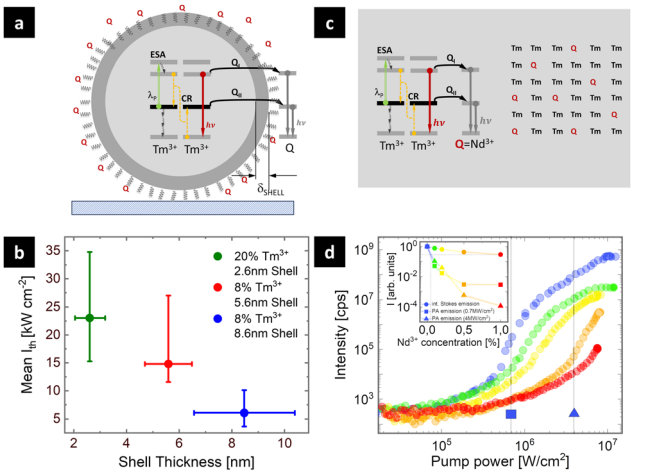

Fig. 21 Impact of quenching on PA emission. (a) Unspecific quenching of Tm^{3+}–Tm^{3+} avalanching pair by surface effects in Tm^{3+}-doped $NaYF_4$ ANPs, (b) mean ± variance pump power threshold *versus* the shell thickness for 2.6, 5.6 and 8.6 nm shell thickness. (b) Correlation between shell thickness and the mean ± variance of single-ANP I_{th} distributions.[80] Reprinted with permission from ref. 80. Copyright 2021, the American Chemical Society. (c) Specific quenching of the Tm^{3+}–Tm^{3+} avalanching pair by volumetric Nd^{3+} ions. (d) Pump power-dependent luminescence of Tm^{3+} ions for an increasing concentration of the quencher in $LiYF_4$ microcrystals and intensity profiles (inset) at fixed pump powers.[12] Adapted with permission from ref. 12. Copyright 2024, the Royal Society of Chemistry (https://creativecommons.org/licenses/by/3.0/).

The specific RET quenching of the emitting and looping levels of the looping Tm^{3+} ions has been recently tackled by incorporating Nd^{3+} acceptor ions within the $LiYF_4$ host material[12] (Fig. 21c and d). The microcrystals were proposed to exclude surface effects and unspecific quenching, which in principle enabled control of RET in a more precise way by varying the average donor–acceptor distance, which was controlled by the acceptor concentration. The $^2H_{9/2}$,$^4S_{5/2}$ and $^4I_{13/2}$ levels of Nd^{3+} remained resonant to the $^3H_4$ (emitting) and $^3F_4$ (looping) levels in Tm^{3+} ions, respectively. The GSA and ESA-based photoexcitation were directly compared, which evidenced many important aspects of PA behaviour. Firstly, a gradual increase in the acceptor concentration from 0.1% to 1% led to gradual quenching of the Tm^{3+} emission was observed both in the steady-state and kinetic domains, but while the GSA only led to a 4 times decrease in the Stokes emission intensity, in the ESA mode, the PA emission dropped by 4 orders of magnitude. Simultaneously, the luminescence decay dropped from 240 μs to *ca.* 80 μs (for 1%Nd^{3+} co-doping), which confirmed the non-radiative RET mechanism. By pump–probe measurement, the luminescence lifetime of the looping level at *ca.* 6000 cm^{-1} was dramatically shortened from 13.6 ms for the pristine Tm^{3+} only-doped crystals to 5.2 ms for as little as 0.1%Nd^{3+} co-doping, which obviously disrupted the energy looping, resulting in a chance to achieve PA emission. Higher acceptor concentrations prohibited the further kinetic characterization of the looping levels. These experimental studies were supplemented with further theoretical modelling based on the phenomenological model of Tm^{3+} PA in $NaYF_4$ nanoparticles,[2] which remains a very useful method to evaluate the impact of the phenomenological parameters on the PA performance.[6,10] Here, this model and the rate equations describing both the looping and emitting levels were extended with the RET mechanism. These simulations enabled the impact of the acceptor individually on the emitting and the looping levels to be distinguished. These theoretical considerations are extremely valuable because it is difficult to find and quantitatively compare the impact of the specific quenching of the looping level because it is typically located in the range of 2000–6000 cm^{-1}. Moreover, the Nd^{3+} levels are suitable to quench both the looping and emitting levels of Tm^{3+} ions, and because within single ANP there are hundreds to thousands of avalanching Tm^{3+} ions, the output luminescence is the sum of luminescence from all the ions exposed to quenchers staying at the average distance. There, the simulations clearly showed distinct effects for the two quenching mechanisms, *i.e.* through quenching of the emitting (Q_I) and the looping (Q_{II}) levels. The Q_{II} mechanism increased the PA threshold but in principle did not affect the nonlinear behaviour and brightness in the saturation regime. The Q_I mechanism reduced the nonlinearity but additionally reduced the brightness. The combination of both processes should be actually observed in real systems.

These results suggest that PA emission is significantly susceptible to the presence of acceptor/quencher molecules at distances, which are a few-fold larger than that expected from the Förster distance calculated for the same D–A pair. This susceptibility is not related to any change in the properties of the D or A alone or the fundamental mechanisms behind RET, but originates from the extreme susceptibility of the donor excitation to minute perturbations in photoexcitation and energy distribution on the looping and emitting levels. The predicted and demonstrated susceptibility is of critical importance because of the practical design of *in situ* bio-sensors.

7.1.3 Threshold powers and photodarkening. Although the excitation powers for ANPs (typically 10–100 kW cm^{-2}) are relatively modest compared to comparable nonlinear optical processes, which is a major challenge faced by ANPs, most of the applications discussed in the previous section would benefit from an even lower power consumption and dose. Lower pump powers are particularly beneficial for applications such as biological sensing to minimize photodamage, or for sensing applications such as infrared detection and night vision.

Another reason to minimize the excitation power is to avoid inadvertent photodarkening. Although photodarkening has been leveraged for photo switching and sub-diffraction imaging,[169] in other applications, photodarkening can be a major disadvantage of ANPs compared to conventional UCNPs, which are generally stable under most excitation powers. Further research into the mechanism of photodarkening in different PA nanosystems is needed, given that there are studies on the mitigation of photodarkening, *e.g.*, through the development of synthetic methods and structures that suppress the defect states in the host matrix.

7.1.4 Lack of standardization in measurements. A major limitation in interpreting the literature on ANPs is the lack of standardization for the analysis, processing, and reporting of ANP data. Most notably, the calculation of the nonlinearity order S (the slopes of log–log power dependence plots) varies significantly with the processing of the data. Small differences in the background subtraction and the amount of data used to fit the slopes can lead to large changes in S, making these values difficult to compare across the literature (readers are encouraged to attach a healthy range of errors to reported S values and discount the significance of incremental improvements in best-of-class metrics). Even within laboratories or within batches of samples, the observed avalanching behaviour can vary significantly. Considering the time-consuming nature of power scans, large numbers of replicate measurements are often not possible. Also, given the infancy of the ANP field, there are no generally accepted standards for data processing or the quantity of data needed for fitting or establishing a representative sample. We strongly advise that stakeholders and researchers in the field of PA nanomaterials (lanthanide and otherwise) collectively establish these standards in data processing and reporting to facilitate fair comparisons, rigorous review, and efficient dissemination of knowledge. These generally accepted practices should also include the deposition of raw data, metadata, documentation, and processing code[6] into open databases. Some proposals for data processing are discussed to some extent in Section 2.7.

It is also critical to mention that the optical setup used to characterize the PA properties should be extremely well evaluated and optimized because any unconscious variation in the pump power in the PA regime (originating from the laser diode intensity/laser optical mode switching/positioning of the diffraction limited beam against the sample, short and long term

instabilities, switching optical components in the light path) can be a source of significant errors. In view of the possible variation in the derived parameters depending on the pump power intensities (due to photodarkening,[214] sample density and way of preparation, single NPs *versus* a monolayer of NPs *versus* aggregates of ANPs), the experimental conditions should be precisely reported. Moreover, for single ANP studies, a change in the ANP position against the laser beam should be verified before and after the experimental evaluation, given that tiny sample shifts in *XYZ* space occurring at the time of the studies may significantly contribute to the outcome and interpretation of the PA results. Moreover, thermal issues should also be avoided and evaluated in the analysis of the results. Typically, large aggregates of particles and a high-power laser with a large beam size will make the samples generate excessive heat, which will be evidenced with broadened emission lines up to white/yellow broadband emission generation and irreversible sample burning and damage.

7.1.5 Biofunctionalization. Another potential difficulty with lanthanide-doped nanoparticles is the fact that they are inherently not bispecific, and thus require proper biofunctionalization. Numerous biofunctionalization protocols have been developed[15,16,92,219,220] and have demonstrated suitability for bio-sensing or bio-imaging, both *in vitro* and *in vivo*. The biofunctionalization of NPs is required to accessorize these NPs with the capability to bio specifically interact with target molecules, which obviously becomes an issue when distance-dependent FRET bio-sensing is considered. Typical antibodies have a size in the range of 5 to 10 nm, which is equal to or even larger than the typical Förster distances at which the donor–acceptor non-radiative ET drops to 50% of the value found for direct interaction. This has led to numerous hypotheses and experimental verifications of core–shell designs of UCNP-based hybrids aiming to improve the sensitivity of upconversion FRET (UC-FRET). Although these UC-FRET systems outperform many other systems based on organic fluorophores in terms of photostability and favourably high signal-to-background ratio, the response of UC-FRET is diminished and more complex due to the fact that many-donors-many-acceptors must be considered. Due to the size of UCNPs (typically 8–25 nm in diameter), the D ions stay in highly statistically variable distances from the surface, where the A molecules can be attached through bio-recognition molecules and reaction (*e.g.* antibody-antigen). The necessity for the latter makes the effective D–A distance even larger (Fig. 17). Photon avalanche nanoparticles may again show some promising features in this area, given that tiny disturbances (owing to the presence of acceptor molecules close to the avalanching system) occurring to the intermediate or emitting levels should be translated to significant variations in spectral properties. However, thus far, only theoretical predictions have been shown,[81] awaiting experimental evaluation.

In any biosensing system, the bio-specific interaction between the optode and the analyte should be translated to a variation in some spectral properties capable of being quantified. In luminescence, they are typically luminescence spectra (or emission intensities at specific wavelength(s)) or luminescence kinetics. In the photon upconversion mode, the typical short wavelength photoexcitation from the commonly applied light sources (lamps with filters, LEDs or sometimes lasers) must be exchanged with stronger NIR lasers matching the sensitizing Yb^{3+} (at 980 nm) or Nd^{3+} (at 800 nm) ion absorption. This imposes further modifications in the spectral filtering of the detection system. Firstly, anti-Stokes emission requires short-pass filters to replace long-pass ones. The large Stokes shift simplifies filtering out the laser excitation, but the small QY translates to a large discrepancy between the excitation and emission line, and thus the dichroic filters must be effective in reflecting the NIR excitation and transmitting the weak visible luminescence. Beneficially NIR photoexcitation undergoes scattering to a lesser extent compared to short wavelength photoexcitation. Alternatively, the tens of microseconds to milliseconds long kinetics are technically much easier to be measured compared to the very demanding time-correlated single-photon counting techniques required for (sub)-nanosecond-long kinetics. However, these slower kinetics are related to dimmer luminescent labels, and ultimately slower fluorescence imaging, *e.g.* during raster scanned imaging. In summary, these properties are distinct from conventional fluorophores and require customization of the detection instruments (*e.g.* well plate readers, and microscopes), but it is clear that the benefits of UCNPs justifies this work. Furthermore, the requirements needed to generate and utilize photon avalanche are not very different than that valid for the conventional UCNPs. With current developments in semiconductor lasers, available photodetectors and appropriate filters, all these modifications are easily within reach. PA requires relatively high pump power (in the order of tens to hundreds of kW cm^{-2}), which precludes wide-field imaging. Nevertheless, ANPs offer other unprecedented features such as single-beam photon avalanche super-resolution imaging (Section 6.1.3) at no additional cost. This means that converting any confocal microscope to the anti-Stokes luminescence mode is not only beneficial for an improved signal-to-background ratio, but with no charge, enables imaging below the diffraction limit with resolutions of *ca.* 60 nm. Combining these features with the expected bio-sensitivity of ANPs should enable functional super-resolution imaging in the near future.

7.1.6 Multiplexed imaging of PA labels. Another challenge in bioimaging and biosensing is related to the capability to distinguish/visualize many target molecules in the same sample simultaneously and favourably with a single excitation wavelength and with no spectral leaks to enable the unequivocal distinguishing of various targets. Most organic fluorescent molecules display very broad excitation and emission bands, which hinder multiplexing capabilities in homogenous samples. Many more codes are available in the flow cytometry scheme under the assumption that single color-code is used at a time. However, this does not apply for homogenous samples and the number of available codes is typically limited to 4 to 7. Although multicolour emissions were demonstrated for UCNPs, these colours are most often a result of the combination of a few narrow (*ca.* FWHM $\sim$ 20 nm) emission bands from a single or multiple lanthanides. Among the lanthanides, only Pr^{3+} (480, 520, 610, and 635 nm), Eu^{3+} (620 nm), Tb^{3+} (540 nm), Ho^{3+} (540 nm), Er^{3+} (520–540 and 650 nm), and Tm^{3+} (470, 650, and 800 nm) have

shown more (Ho^{3+}, Er^{3+}, and Tm^{3+}) or less (Pr^{3+}, Eu^{3+}, and Tb^{3+}) efficient upconverted emission in the visible light range under NIR photoexcitation.[94,221] This upconverted emission is additionally pump power dependent, indicating that the proportion of the emission bands within a single emitter varies with the pump power, and may additionally vary depending on the dispersive properties of the sample, and thus unequivocally decoding the luminescence label becomes troublesome.[222] Moreover, the emissions of Er^{3+}, Ho^{3+} and Tb^{3+} spectrally overlap with the majority of strong emission lines (*e.g.* at 540 nm), and many similarities also exist with the emission of Pr^{3+} (630–650 nm). In the Stokes mode, additional weak Sm^{3+} (600, 650, and 710 nm) and Dy^{3+} (480 and 570 nm) emissions were measured, and also here many emission lines overlap with that from other lanthanides. This is critical for biosensing, given that the spectral fingerprints of the UCNPs are ascribed to the biospecificity of the UCNP label in the course of the biofunctionalization process. Later problems with the identification of the labels translate to problems with the proper identification of the target molecules. In the course of the upconversion process, Nd^{3+} and Yb^{3+} ions also play an important role, which absorb (at *ca.* 800 and 980 nm, respectively) end emit (860, 1060 and 1020 nm, respectively) in the NIR region, which falls in the optical transmission window of biologically relevant fluids and components (in particular water).

Despite the engineering of materials with different visual colors,[221] a limited number of spectral fingerprints can be effectively considered when lanthanide-doped nanoparticles are not overlapping spatially. Otherwise, two labels that differ only in proportion between, *e.g.* the green and red emission band ratio, will not be distinguished if they co-localize in space (*e.g.* within the point spread function of the confocal photoexcitation beam). A number of attempts tried to provide spectrally pure emission by precise optimization of the co-doping with various lanthanides[223] or by co-doping the upconverting lanthanides with additional ions (*e.g.* Mn^{2+} ions) that can quench some of the energy levels, *e.g.* green Er^{3+} emission.[224] Moreover, although lanthanides produce characteristic (lanthanide and host dependent) emission bands, recognizing these labels is not trivial and requires high-resolution spectrally resolvable photodetectors, which make these detection systems more complex, costly, slower and computationally (due to spectral deconvolution) demanding.

The multiple band emissions from lanthanides have been demonstrated to be suitable for the so-called ratiometric sensing, which exploits the inner filter effect. For example, Er^{3+}-doped nanoparticles emit simultaneously at 520–540 nm (green) and 650 nm (red). When only green emission intensity is modulated by external factors, for example by pH-sensitive dye, whose absorption spectrum varies in this green spectral region, the erbium red emission may serve as a reference for the pH (indirectly)-dependent green emission, and after a simple calibration procedure this green-to-red ratio pH probe can be easily detected or imaged. It should be noted there is no direct interaction between the emitting erbium ions and the pH-sensitive dye, but the erbium green emission from the nanoparticle is spectrally filtered (modulated) by the dye anchored at the UCNP surface. PA emission should show similar features, but the very steep nonlinearity of ANPs to the pump power may complicate the technical side of the measurements. Alternatively, PA offers an unprecedented referencing feature because the PA emission under ESA photoexcitation may be used as a FRET sensor reporter, while the emission at the same wavelength but excited in GSA mode may provide the reference signal. Alternatively, the very slow and pump power-dependent PA rise times have not been explored at all thus far. All these possibilities will surely be studied in the future.

In contrast to multicolour spectral fingerprints, fingerprints that enable various luminescence labels to be distinguished in the time domain have been also proposed and demonstrated. For example, by varying the concentration quenching labels that emit photons of the same energy (colour), but whose luminescence lifetimes are designed such that the luminescence kinetics may be analysed and ascribed. PA emission is quite specific and different from the conventional upconversion. All the problems with creating multilabel (multicolour or time tags) emission are also valid for ANPs, but the specific features of PA emission may enable the generation of additional emission lines or the capability to emit only at a specific photoexcitation wavelength. There is some expectancy in sensitized avalanche emission and core–shell ANP designs, which under a single excitation wavelength may generate numerous new emission lines. However, experimental demonstrations are missing thus far, which will gather interest in the near future.

Multiplexing, *i.e.* the ability to target multiple analytes in liquid or complex samples such as cells of tissues, requires unique and easily quantifiable spectral codes. Considering the recent emergence of PA nanomaterials, the range of emission wavelengths and excitation wavelengths for ANPs is still limited, presenting an opportunity for the continued development of methods to expand the library of ANPs. A good example of tunability for multiplexing is quantum dots, where the quantum confinement effect produces a spectrally distinct shift in the emission bands. Despite their efficient absorption and emission, improved photostability and small size, QDs demonstrate relatively broad and overlapping emission bands, and ubiquitous short wavelength excitation, which overlap with endogenous chromophores in the absorption, scattering and excitation regions.

To realize the multiplexed imaging of multiple labels, a wider range of spectrally distinct ANP labels must be developed. There are four viable strategies for using lanthanide-doped ANPs as luminescence labels, as follows:

1. The first is displacing these labels in space or sample volume, aiming to address them one-by-one by raster scanning confocal imaging. However, due to light diffraction, the best spatial resolution offered does not go below a few hundreds of nanometers. Therefore, despite the multicolour emission, achieving many unique fingerprints with UCNP LnNP labels remains a challenge.

2. The second approach relies on creating pure, single emission band labels, which enable the detection of various LnNP labels in the spectral domain even when the spatial resolution is limited. However, due to the nature of the Ln^{3+} emission, this approach can only generate a limited number of spectral codes, often reducing the brightness.[223]

3. The third approach relies on time domain labels. However, although the lifetimes of LnNPs are long (μs–ms) and they can be engineered to design up to a few time tags,[225] the possibility to distinguish them in complex samples containing multiple labels within the diffraction limited volumes is in practice difficult for numerous reasons, *e.g.*, brightness under short pulses becomes weak and results in a poor signal to noise ratio.

4. The last possibility is using various excitation wavelengths suitable to excite a particular LnNP. However, although short wavelength excitation is often suitable to excite multiple Ln^{3+} nano-labels, it is typically undesirable in bio-applications because it stimulates bio-sample autofluorescence and enhances the background signal. In the case of upconverting labels, NIR excitation (at 920, 976, 800 or 1530 nm) can initiate visible emission, but this remains a technical challenge to switch between light sources, avoid crosstalk between these excitation lines and optically align multispectral images under various excitations.

Therefore, it remains highly desirable to develop ANPs as nanoscale labels, exhibiting multiple pure colour emission spectral fingerprints under a single excitation laser line. However, thus far, only a limited number of singular lanthanide ions in a limited number of host materials under well-adjusted excitation wavelength of sufficient excitation pump power density has been capable of generating PA emission at the nanoscale.

7.2 Novel opportunities for PA studies and applications

Despite the fact that the physical mechanism responsible for PA is relatively well understood and that PA emission has been experimentally demonstrated in single-crystals, further studies and optimization of PA in nano- and micro-scale materials may bring a whole plethora of new features and benefits, and thus may generate active elements for new optical and photonic applications. Here, we briefly discuss some of these application areas, where potentially highly controllable, scalable PA-hosting materials with customizable performance, can stimulate great progress and may promise new possible applications.

7.2.1 Plasmonics. Although plasmons have been shown to enhance the luminescence of lanthanide-doped nanoparticles,[174,226,227] their effects were not spectacular in most cases. However, one may predict that PA will respond to the collective oscillations of electrons in noble metals in a more significant way, in which the sensitivity to the modified electromagnetic environment has analogues to the sensing of changing chemical environments exploited for biosensing. Therefore, one can expect that plasmons will support PA quenching at enhanced distances rather than enhancing the PA emission intensity. Alternatively, a lower PA threshold can also be expected. These questions will undoubtedly stimulate new research in this unexplored area.

7.2.2 Patterning, lithography, and additive manufacturing. The high spatial resolution afforded by the narrow emission profile of ANPs offers opportunities for utilizing these materials for optical lithography[147] and three-dimensional printing with nanometer resolution. The ability to pattern nanoscale features with infrared light offers opportunities for additive manufacturing at depth or highly scattering media using photolabile materials such as biopolymers and inexpensive diodes rather than the costly femto- or picosecond lasers used for multiphoton lithography. In addition to mixing ANPs with traditional photopatternable resins,[228] which exploits the efficient generation of blue and UV wavelengths enabled by PA (as shown with polymer nanoparticles that exhibit triplet–triplet annihilation upconversion), ANPs can be photopatterned directly from thin films. This direct optical lithography may be valuable in applications where polymers cannot be used (*e.g.*, electrical devices) or higher loadings of inorganic materials are necessary.[147]

7.2.3 Ultraviolet (UV) disinfection. Owing to the inherent mechanism of PA compared to conventional GSA/ETU-based upconversion, the generation of short-wavelength light from long-wavelength up to UV photons became possible.[2,146,229] Therefore, ANPs are an ultimate source of local UV light, with numerous possible applications, starting from 3D printing and manufacturing (as noted above), through UV photocatalysis to health care and disinfection. In the latter case, the typical UV cleaning methods rely on external UV sources, which pose risks (*e.g.* harmful UV exposure to human eyes and skin) and additional costs (*e.g.* costly optics and UV-induced material degradation). Therefore, *in situ* UV light generation on the surfaces to be disinfected, under cell/material safe[230] and deeply penetrating (*e.g.* in personal protective equipment (PPE)[231,232]) NIR photoexcitation is of great interest. This concept is not only applicable to PPE, medical tools and instruments, but also public surfaces and commercial apparel including clothing and accessories.

7.2.4 Anti-counterfeit protection. It is worth noting that PA-based materials and constructs can provide additional benefits from the point of view of cryptography and security, given that their proper well-defined excitation beam properties may be employed to observe the desired output. Besides the proper combination of illumination power densities (defined by threshold value, which can vary depending on dopant concentrations, temperature, sample architecture, *etc.*), a very specific combination of excitation wavelengths is also required to be well fitted to the desired narrow transition bands. All these requirements make the reading of coded output a significant task. Reverse engineering of these materials will be extremely difficult, given that even sophisticated material studies will not be sufficient to replicate these luminescent features.

7.2.5 Sensing chemical and biological analytes. Lanthanide ions, and especially lanthanide-doped nanoparticles serving as energy donors for homogenous FRET assay promise numerous potential advantages, where background-free detection is their most important feature. However, the inherent nature of LnNPs, such as size, hinders the wider adoption[30] of these otherwise promising candidates for biosensing.[30,233–237] The PA demonstrates a very steep relationship between input pumping power and luminescence achieved in the course of recursive energy circulation in these systems. By theoretical simulation, it was predicted that even a tiny perturbation in the energy looping may lead to an unproportionally large change in the output luminescence, which suggests that this PA emission may serve as reporting technology for biosensing. This has

been confirmed in proof-of-the-concept experiments where the highly nonlinear behaviour of PA emission demonstrated extreme susceptibility to the presence of quenchers.[12] The fact that PA was demonstrated at the nanoscale opens new perspectives, because FRET, which is typically used for homogenous immunoassays, is a short-range interaction, meaning that its effectiveness, and thus capability of sensing the donor and acceptor interaction depends on the inverse of the 6th power of the distance between them, and consequently the Förster distance is typically shorter than 6 nm. In view of the relatively large size of lanthanide-doped nanoparticle donors and the bio-specific recognition molecules (*e.g.* IgG antibodies have a length of around 10 nm), the small perturbation (quenching) occurring at extended distances is of paramount importance for the sensitive and bio-specific detection of antigens or DNA/RNA fragments. Although conventional LnNPs are barely suitable for this purpose, this extreme susceptibility of PA emission may become a solution.

7.2.6 Mid-infrared sensing and imaging. One of the first applications of PA, in addition to upconversion lasers, was the construction of photon counters, especially those dedicated to the NIR and MIR spectral range (3–20 μm). In these concepts, the PA material is pre-pumped with light tuned just below the critical PA threshold. Thus, the presence of low-energy photons matching the transition from the ground state to the looping excited states can lead to significant changes in the outcome of PA emission intensity.

There is great demand for the detection of MIR photons due to the importance of this radiation in many applications, such as spectroscopy, metrology, (bio)imaging, molecular analysis of gases and astronomy.[238–242] Unfortunately, the detection of MIR radiation in a sensitive and cost-effective way is challenging, mostly due to the insufficient sensitivity of the available detectors in this wavelength range.[242] Moreover, its detection is hampered by the high noise signal due to the natural emission above absolute zero in the infrared range. Thus, there is a substantial need to develop new MIR photon counters allowing to bypass the limitations resulting from the low energy of the analysed radiation, and hence the high thermal background.[243]

One of the proposed methods for the detection of the MIR signal is its conversion to visible radiation, where the detectors are much more sensitive, cheap and widely available. An example is the upconversion process, which in the most well-known case shifts the NIR photons to a higher energy in the visible, and thus it can be detected with the generally available detectors.[243] In 1959, Bloembergen proposed an IR quantum counter (IRQC), the operation of which is based on a two-step excitation process.[244] In the Bloembergen IRQC, the operation scheme includes the first step when infra-red radiation excites the atoms to a metastable level, followed by the next step in which the intense pump excites the atoms to a higher emission level. Therefore, the IR signal is incoherently upconverted to emission in the spectral range where very sensitive and much cheaper detectors are commonly available.

Based on the Bloembergen approach, in 1968, Esterowitz *et al.* proposed an ideal five-level IRQC system (Fig. 22a), where

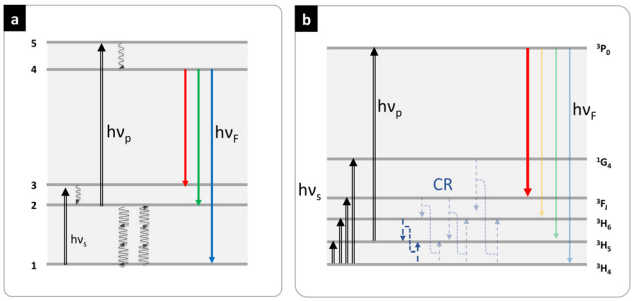

Fig. 22 MIR photon counting (a) five-level quantum counter scheme (hv_p – pump, hv_s – signal, hv_f – fluorescence. Wavy arrows indicate non-radiative transitions).[145] (b) IR detection scheme based on Pr^{3+}.[245] Dashed arrows are possible cross relaxations (CR) responsible for photon avalanche phenomenon. Transparent lines are additional possible CR and fluorescence transitions not shown in ref. 245.

the IR signal transition (1 → 3) is followed by rapid depopulation *via* a nonradiative transition to the lower lying metastable level (2).[145] Subsequently, the pump transition (2 → 5) occurs, which is followed by a fast nonradiative transition to the fluorescent lower lying level (4). The proposed system allows the problems occurring in the simplest IRQC system with three energy levels to be bypassed, in particular to eliminate the reabsorption of the resulting radiation by the active ions and pump saturation. Moreover, additional levels allow the electron to be recycled, and thus for each absorbed IR photon, more than one visible photon may be emitted. In their work, the authors reported 165 schemes of IRQC found in trivalent rare earth ions in various host materials, the amount of which, as indicated, can be greatly increased by the addition of another co-dopant ion (*e.g.* Yb^{3+}). However, most of the reported IRQC schemes were established for IR radiation shorter than 3 μm. Recently, Liang *et al.*[238] proposed an approach with an inverted sequence, with continuous visible pumping responsible for promoting the ions from the ground to the excited level, which is followed by fast energy relaxation to the lower energy levels, and then NIR emission. However, presence of the MIR photons results in the ions being excited back from this emitting level to a higher one, from where also higher energy emission occurs. Thus, the intensity of the MIR radiation affects the luminescence intensity of these two emitting bands.

PA medium infrared quantum counter detectors (MIRQC) were first reported in 1979 by Chivian *et al.*, who while studying materials for IR quantum counters, discovered the PA phenomenon in Pr^{3+}-doped $LaCl_3$ and $LaBr_3$ hosts.[1] The underlying concept was simple, *i.e.*, the materials were pre-pumped with wavelength matching ESA ($^3H_5 \rightarrow {}^3P_J$) instead of GSA ($^3H_4 \rightarrow {}^3P_J$) excitation. Above some pump power density threshold (*ca.* 1.2–12.2 W cm^{-2}), a sharp 100-fold increase in the red luminescence intensity at 600–640 nm ($^3P_0 \rightarrow {}^3H_6$, $^3P_1 \rightarrow {}^3F_2$, $^3P_0 \rightarrow {}^3F_2$) was observed. When the system was close to the PA threshold, the 4.5 μm photons (matching ground $^3H_4$ to $^3H_5$ level of Pr^{3+} ions) at 1–10 mW cm^{-2} intensities were sufficient to trigger PA emission, and consequently a 4-fold increase in the sensitivity of MIR photon detection was demonstrated.[1] The

interpretation of the obtained results was based on the sequence of ion interactions, in which the absorption of one photon in the infrared region led to the generation of multiple excitations.

In 1983, Krasutsky presented the first crystal quantum counter working at a wavelength longer than 5 μm. This system, based on the $LaBr_3$:Sm^{3+} crystal, was sensitive in the spectral range of 2 to 10 μm due to the utilization of a low phonon material.[37] The authors described the pump-dependent background noise as the main limitation of the studied system detectivity. The PA, observed above pump power densities of 3 kW cm^{-2}, was considered a limitation mainly due to difficulties in performing experiments and ensuring pump stability and intensity. Consequently, the PA phenomenon set an upper limit on the maximum pump power density that could be used for IRQC experiments.

Although benefits arising from the utilization of PA were not fully recognized initially, in 2003, D. B. Gatch *et al.* showed that due to PA, the signal-to-noise ratio for the IRQC can be improved.[245] This was shown by both experimental results and numerical modelling. Moreover, this experiment was carried out at room temperature. The authors used an $LaCl_3$:8%Pr^{3+} crystal pumped by a focused dye laser beam (560 nm), while the IR signal was provided by a tungsten-halogen lamp. They demonstrated an enhancement in the detection of the IR signal corresponding to the three transitions, *i.e.*, $^3H_4 \rightarrow {}^3H_6/{}^3F_J/{}^1G_4$, in the range of 1.0–2.3 μm for monitored PA emission. Below the critical threshold of pump power (30 mW) and with the addition of an 11 mW IR signal, an increase in the visible emission was observed with a signal-to-noise ratio greater than one. In contrast, for the same IR signal but for a pump power above the threshold, an increase in the visible emission was observed with a signal-to-noise ratio of less than unity. Moreover, the signal-to-noise ratio decreased to 0.5 at the threshold power of 30 mW when the IR signal was reduced to 5 mW.

Fig. 22b presents a schematic illustration of the IRQC based on Pr^{3+} ions. When the ion concentration is increased, cross-relaxation (CR) processes loop the energy between the excited and ground states of two neighbouring Pr^{3+} ions, leading to doubling of the population of intermediate excited level in every iteration of the loop and an increase in resonant photon absorption of pump photons, $h\nu_P$. Consequently, a visible emission was observed from the $^3P_0$ level, and the intensity thereof is dependent on the initial population of the $^3H_5$ level. The population of the latter level depends on the flux of MIR photons, and thus the visible emission is nonlinearly dependent on the MIR light detected by this quantum converter.

Among the methods for detecting single photons in MIR, one can mention the technique based on a crystal detector utilizing the sum frequency generation phenomenon. Photons are upconverted to near infrared radiation, and then detected by avalanche photodiodes.[246] Another method for MIR detection is the use of the nonlinear optics process of three-wave mixing, but this technique requires precise phase matching and high pulse powers, which are only achievable with femto- and picosecond lasers.[246] InGaAs semiconductor materials provide technical feasibility to detect or image MIR photons, but these detectors are not very sensitive and are also very expensive.[247] The mid-infrared light detection by optomechanical frequency upconversion is a novel advanced method and was first theoretically studied by P. Roelli *et al.*[248] and further developed by W. Chen *et al.*[242] and A. Xomalis *et al.*[249] In this method the frequency upconversion was achieved by the utilization of the IR absorption and Raman activity of molecular vibrations. The coherent interaction of the electronic state of a molecule with its vibrational states through IR light, together with specially designed antennas and gold nanospheres confining the MIR energy to a narrow slot allowed the detection of the MIR signal with a power of less than a microwatt. However, despite their enormous potential, the presented devices showed limited stability due to the use of organic molecules. The lifetime of these device can exceed one month only if proper encapsulation that excludes the presence of oxygen is provided.[243]

The broad application field of MIR detectors is constantly motivating researchers to develop new sensitive, cost-effective detection schemes. IRQC based on the PA phenomenon, as detailed in this review, can bring new possibilities of measurements at room temperature with a reduced signal-to-noise ratio and, through ladder-like energy levels, prevent rapid saturation of the level from which emission occurs. The development of new PA materials based on various lanthanide ions and nanoscale host materials together with advancements in measuring systems may also open new possibilities of MIR detection at the nano-microscale in biology through optical microscopes that traditionally work in the visible spectral range.[1,37,145,243,245,246,250]

Extending the concept of photon counting with PA nanomaterials, a straightforward extrapolation is IR imaging instead of simple intensity measurements counting from one single point or total intensity emitted from the bulk volume of a sample. The involvement of PA as a workhorse enables the reaping of the essential benefits connected to it, such as great sensitivity and signal amplification accompanied with translation of the detected MIR photons into visible or NIR photons, which are more suitable to detect even with simple and cheap photodetectors. Two valuable architectures of the PA-based optically active element can be proposed. The first, utilizing a bulk monocrystal, acting as a screen or photographic film, inside which the image constructed by the incoming MIR photons is transferred into the visible projection, making it possible to map with optical microscopy techniques. An analogous operating blueprint can be also found for the second approach, where the active element is composed of a film of nanocrystals, and each of them can operate as an independent pixel (or voxel), providing better resolution due to the limited cross-talk (owing to energy migration) between neighbouring regions. Moreover, this design opens the possibility of sensitivity at multiple spectral bands owing to the use of mixtures of several ANP. Nevertheless, in these approaches for narrowband sensitivity, MIR detection is inherently connected with several technical difficulties. Firstly, a wide area of the avalanching material should be pumped homogeneously with a stable power density

slightly below the threshold value. This can be challenging because tens or hundreds of kW cm^{-2} are required for the most well-known materials featuring efficient PA. Furthermore, the MIR spectral sensitivity can require the application of various PA ions or PA schemes, and thus different pumping wavelengths or thresholds may apply. These issues can be at least partially overcome, similarly as some challenges arising from the point of view of sub diffraction imaging, thermometry or FRET sensors, by the development of materials featuring efficient PA and characterized by a low power threshold value.

7.2.7 Photon avalanching nano lasers. The ability of PA to nonlinearly amplify and invert excited-state populations makes ANPs promising materials for PA lasers, particularly in micro- and nanoscale applications. Rare earth ions have been commonly utilized in lasers due to their high stability, long-lived metastable electronic states and narrow emission lines. The rich electronic structure of the lanthanide $4f^N$ states facilitate 3- and 4-level laser operation and offers a wide range of pump and output wavelengths. Beside the conventional Stokes lasers, anti-Stokes processes such as upconversion and PA enable lasers that exploit excitation wavelengths matching high absorption cross-section transitions within rich energy levels in lanthanides to ultimately broaden the choice of available laser lines from these solid-state lasers. The most common mechanisms utilized to obtain up-conversion-based laser emission are ESA and ETU, as reviewed previously for bulk materials by M. Joubert and R. Scheps.[17,34] An interesting alternative to these broadly developed Stokes and anti-Stokes pumping schemes is lasing based on the PA mechanism.[251]

PA pumping of lasers has been observed since 1990 in Pr^{3+} (7%)-doped $LaCl_3$ material,[252] where 677 nm input photons were converted into a 644 nm laser output, giving an efficiency of 25%. Other early reports presented lasing in bulk materials and fibers[46] doped with Nd^{3+} (ref. 32) and Tm^{3+} (ref. 253) and co-doped with combinations such as Pr^{3+}/Yb^{3+}.[254] A broad range of visible emissions is covered by PA lasers, with most of the laser systems (and all the ones exhibiting efficiencies above 10%) produced based on Pr^{3+} or Pr^{3+}/Yb^{3+} co-doped materials. However, the great majority of the known reports on this topic were published in the 90s and early 2000s, which had no chance to gain from the current knowledge and technologies developed and provided by the nanotechnology field in the last decade.

The use of upconverting nanomaterials as gain media for lasers has opened new applications for lasers, such as microscale lasers as ultrasharp emitters for bioimaging. Unlike bulk materials, UCNPs can be readily coated onto or assembled into resonators and cavities (including the whispering gallery modes),[255–257] microcavities or plasmonic array nanocavities,[258,259] Promising results have been reported using $NaYF_4$ core–shell nanoparticles doped with Tm^{3+} ions, which are known for hosting energy looping[77] and PA. These nonlinear processes promote population inversion through the avalanche-like building of the population of the $^3H_4$ metastable state.[95] These nanoparticles, assembled on 5 μm polystyrene microspheres, emit at the room temperature whispery gallery mode-enhanced continuous wave laser light at 800 nm and 450 nm.[260] The avalanche-like pumping (with a slope of ~7 or ~4 for emissions at 800 nm and 450 nm, respectively, and the average threshold value of 44 ± 23 kW cm^{-2}) was presented with a 1064 nm ESA-resonant excitation beam. Moreover, controlled assembling of the UCNP layer on the microcavities enabled the production of systems with a down-shifted threshold power density to 0.7–0.9 kW cm^{-2}, with demonstrated potential for biosensing.[261] Other types of lasing with avalanche-like characteristics (slope of 4.4 and threshold of emission intensity at 70 W cm^{-2}) have been reported for $NaYF_4$ core–shell nanoparticles, with their core co-doped with Er^{3+} and Yb^{3+} ions, assembled on an array of plasmonic Ag nanopillars.[262] The studies of the highly nonlinear response of materials and possibility of laser emission in micro or nano laser cavities can not only provide insights into laser light and interaction at the molecule level but also for photonics devices or mechanisms on the nanoscale.

Although PA-based lasers preserve all the key advantages of conventional lanthanide ion-based upconverting lasers, they offer new possibilities. Firstly, they significantly extend the selection of available combinations of pumping wavelengths, which are not resonant with GSA transitions (like in most common pumping schemes) and have to be well fitted to the desired ESA transition. The resulting laser lines often provide emission and amplification in the visible range, similar to the case of Pr^{3+}-doped systems. Also important, in conventional UC mechanisms, efficient energy CR is a parasitic effect hindering population inversion and attenuating the laser emission, and therefore higher dopant concentrations are neither recommended nor assure the optimal performance. However, an increase in the concentration of dopants in the case of the PA scheme is highly desirable because energy looping, which is governed by the CR mechanism, is responsible for fuelling the multiplication of ions in the intermediate metastable state. Not only a *ca.* 10-fold larger absorption cross section (for excitation powers exceeding the threshold value) can be obtained compared to laser materials operating in other schemes, but the brightness is enhanced as well with an increase in the number of emitting ions. The nature of the PA phenomenon exhibits a highly nonlinear relation between pumping power and resulting output efficiency. Consequently, PA lasers provide a high in-out efficiency performance; however, they require pumping power densities exceeding the threshold value for their optimal operation.[251] Finally, the fact that the PA has become available at the nanoscale level opens new possibilities in the fields of nano-bio-technology, biology or environment sensing, nanophotonics, telecommunication and optical computing.[251]

8. Conclusion

This review surveyed the fundamentals of photon avalanche, the development of lanthanide-doped photon avalanching nanoparticles, their application, challenges and opportunities for their further investigation. As a nascent field, the examples of true PA in nanomaterials are sparse, together with their practical applications. However, these few examples have been

groundbreaking, with their impacts and applications far beyond the immediate field of lanthanide-doped upconverting nanoparticles. The unprecedented optical feedback within these ANPs makes them the most nonlinear materials reported thus far, a fact that has captured the imagination of scientists across a broad range of disciplines. These diverse applications include sub-diffraction imaging, mechanical sensing, optical computing, and machine learning. We envision that through collaborations within these disciplines, further new applications will arise from the basic concepts developed thus far and reviewed herein. Similar to the mechanism of PA, the initial seeds of progress in the ANP research reviewed herein will explode into outsized scientific contributions to any field that can utilize the unique optical nonlinear responses of these materials.

Abbreviations

AF	Autofluorescence
ANPs	Photon avalanche nanoparticles
APD	Avalanche photodiodes
Bkg	Background signal (*e.g.* autofluorescence)
CET	Cooperative energy transfer
CL	Cooperative luminescence
CR	Cross relaxation
CS	Cooperative sensitization
CW	Continuous wave
C@S	General naming strategy for core@shell nanoparticles
EM	Energy migration
EMU	Energy migration-based energy transfer upconversion
ESA	Excited state absorption
ET	Energy transfer
ETU	Energy transfer upconversion or APTE addition de photon par transferts d'energie
FED	Fluorescence emission difference
FRET	Förster resonant energy transfer
GSA	Ground state absorption
IRQC	The infrared quantum counter
PMT	Photomultiplier
LIR	Luminescence intensity ratio
LN	Nonlinear luminescence
LnNP	Lanthanide doped nanoparticle
LT	Luminescence lifetime
MIR	Medium infrared
MPA	Migrating photon avalanche
MPR	Multiphoton relaxation
MRI	Magnetic resonance imaging
NGRER	Non-GSA-resonant ESA-resonant
NIR	Near infrared
NIRES	Near-infrared emission saturation
NR	Nonradiative relaxation
NSI	Nonlinear structured illumination microscopy
PA	Photon avalanche
PAA	Poly(acrylic acid)
PAET	Photon assisted energy transfer
PALM	Photoactivated localization microscopy
PANP or ANP	Photon avalanching nanoparticles,
PA-RET	Photon avalanche resonant energy transfer
PASSI	Photon avalanche single beam super resolution imaging
PAT	Photon avalanche thermometry
PEG	Poly(ethylene glycol)
PEI	Poly(ethyleneimine)
PVP	Polyvinylpyrrolidone
qCW	Quasi continuous wave
QD	Quantum dot
RS	Raster scanning
RE ions	Rare earth ions
RET	Resonant energy transfer
SAT	Saturation nanoscopy
SBR	Single band ratiometric
SFG	Sum frequency generation
SHG	Second harmonic generation,
SIM	Structured illumination microscopy
SPA	Sensitized photon avalanche
STED	Super-resolution stimulated emission depletion microscopy
STORM	Stochastic optical reconstruction microscopy
THG	Third harmonic generation
UC	Up-conversion
UCNP	Upconverting nanoparticle
UC RET	Upconversion RET
uSEE	Super-linear excitation–emission
WNR	Non-radiative rates
VIS	Visible radiation
ZBLAN	ZrF_4–BaF_2–LaF_3–AlF_3–NaF

Author contributions

Conceptualization, resources and funding acquisition (AB, EC, JS, AS, MSz), writing original draft (AB, MSz, EC), writing – review & editing and visualisation (all authors), supervision (AB).

Data availability

No primary research results, software or code have been included and no new data were generated or analysed as part of this review.

Conflicts of interest

There are no conflicts to declare.

Acknowledgements

The authors acknowledge financial support from NCN, Poland, grant numbers NCN 2018/31/B/ST5/01827 (AB, MSz, ZK, MD), 2021/43/B/ST5/01244 (AB, MMa, MMi, KP). Work at the Molecular Foundry was supported by the Office of Science, Office of Basic Energy Sciences (BES), of the U.S. Department of Energy

(DOE) under Contract No. DE-AC02-05CH11231. A. S. acknowledges partial support from the European Union's Horizon 2020 research and innovation program under the Marie Skłodowska-Curie Grant Agreement No. 895809 (MONOCLE). A. S. and E. M. C. were partially supported by the DOE Office of Science, BES, through the Chemical Sciences, Geosciences, and Biosciences Division, Separations Program under Contract no. DE-AC02-05CH11231. P. J. S. acknowledges support from the National Science Foundation grant CHE-2203510.

References

1 J. S. Chivian, W. E. Case and D. D. Eden, *Appl. Phys. Lett.*, 1979, **35**, 124–125.
2 C. Lee, E. Z. Xu, Y. Liu, A. Teitelboim, K. Yao, A. Fernandez-Bravo, A. M. Kotulska, S. H. Nam, Y. D. Suh, A. Bednarkiewicz, B. E. Cohen, E. M. Chan and P. J. Schuck, *Nature*, 2021, **589**, 230–235.
3 Y. Liang, Z. Zhu, S. Qiao, X. Guo, R. Pu, H. Tang, H. Liu, H. Dong, T. Peng, L.-D. Sun, J. Widengren and Q. Zhan, *Nat. Nanotechnol.*, 2022, **2022**, 1–7.
4 Z. Zhang, A. Skripka, J. C. Dahl, C. Dun, J. J. Urban, D. Jaque, P. J. Schuck, B. E. Cohen and E. M. Chan, *Angew. Chem., Int. Ed.*, 2023, **62**, e202212549.
5 A. Skripka, M. Lee, X. Qi, J. A. Pan, H. Yang, C. Lee, P. J. Schuck, B. E. Cohen, D. Jaque and E. M. Chan, *Nano Lett.*, 2023, **23**, 7100–7106.
6 M. Dudek, M. Szalkowski, M. Misiak, M. Ćwierzona, A. Skripka, Z. Korczak, D. Piątkowski, P. Woźniak, R. Lisiecki, P. Goldner, S. Maćkowski, E. M. Chan, P. J. Schuck and A. Bednarkiewicz, *Adv. Opt. Mater.*, 2022, 2201052.
7 C. Wang, Z. Wen, R. Pu, B. Pan, B. Wang, K. Zheng, Y. Du and Q. Zhan, *Adv. Mater.*, 2023, **2**, e2307848.
8 C. Wang, Z. Wen, R. Pu and Q. Zhan, *Laser Photonics Rev.*, 2024, 2400290.
9 Z. Zhu, Y. Liang, Q. Zhao, H. Wu, B. Pan, S. Qiao, B. Wang and Q. Zhan, *Sci. Bull.*, 2023, **69**, 458–465.
10 M. Szalkowski, M. Dudek, Z. Korczak, C. Lee, Ł. Marciniak, E. M. Chan, P. J. Schuck and A. Bednarkiewicz, *Opt. Mater.: X*, 2021, **12**, 100102.
11 M. Dudek, Z. Korczak, K. Prorok, O. Bezkrovnyi, L. Sun, M. Szalkowski and A. Bednarkiewicz, *Nanoscale*, 2023, **15**, 18613–18623.
12 M. Majak, M. Misiak and A. Bednarkiewicz, *Mater. Horiz.*, 2024, 4791–4801.
13 A. Bednarkiewicz, M. Szalkowski, M. Majak, Z. Korczak, M. Misiak and S. Maćkowski, *Adv. Mater.*, 2023, **35**, 2304390.
14 Z. Korczak, M. Dudek, M. Majak, M. Misiak, Ł. Marciniak, M. Szalkowski and A. Bednarkiewicz, *Low Temp. Phys.*, 2023, **49**, 322.
15 A. Sedlmeier and H. H. Gorris, *Chem. Soc. Rev.*, 2015, **44**, 1526–1560.
16 A. Hlaváček, Z. Farka, M. J. Mickert, U. Kostiv, J. C. Brandmeier, D. Horák, P. Skládal, F. Foret and H. H. Gorris, *Nat. Protoc.*, 2022, **2022**, 1–45.
17 M.-F. F. Joubert, *Opt. Mater.*, 1999, **11**, 181–203.
18 S. Guy, M. F. Joubert and B. Jacquier, *J. Alloys Compd.*, 1998, **275–277**, 186–190.
19 M. F. Joubert, S. Guy, B. Jacquier and C. Linarés, *Opt. Mater.*, 1994, **4**, 43–49.
20 M. Runowski, P. Woźny, I. R. Martín, K. Soler-Carracedo, T. Zheng, H. Hemmerich, F. Rivera-López, J. Moszczyński, P. Kulpiński and S. Feldmann, *Adv. Funct. Mater.*, 2024, **34**, 2307791.
21 R. M. Corn and D. A. Higgins, *Chem. Rev.*, 1994, **94**, 107–125.
22 A. Teitelboim, B. Tian, D. J. Garfield, A. Fernandez-Bravo, A. C. Gotlin, P. J. Schuck, B. E. Cohen and E. M. Chan, *J. Phys. Chem. C*, 2019, **123**, 2678–2689.
23 H. Wen, H. Zhu, X. Chen, T. F. Hung, B. Wang, G. Zhu, S. F. Yu and F. Wang, *Angew. Chem., Int. Ed.*, 2013, **52**, 13419–13423.
24 F. Wang, R. Deng, J. Wang, Q. Wang, Y. Han, H. Zhu, X. Chen and X. Liu, *Nat. Mater.*, 2011, **10**, 968–973.
25 X. Xie, N. Gao, R. Deng, Q. Sun, Q. H. Xu and X. Liu, *J. Am. Chem. Soc.*, 2013, **135**, 12608–12611.
26 S. Liu, L. Yan, J. Huang, Q. Zhang and B. Zhou, *Chem. Soc. Rev.*, 2022, **51**, 1729–1765.
27 M. Pollnau, D. R. Gamelin, S. R. Luthi, H. U. Gudel and M. P. Hehlen, *Phys. Rev. B: Condens. Matter Mater. Phys.*, 2000, **61**, 3337–3346.
28 X. Liu, J. Chen, C. Liu, S. Xi, S. Tan Tan, Q. He and L. Liang, *Extreme Optical Nonlinearity (>500) at Room Temperature through Sublattice Reconstruction*, 2024.
29 A. Bednarkiewicz, E. M.-Y. E. M. E. M. Chan, A. M. Kotulska, L. Marciniak and K. Prorok, *Nanoscale Horiz.*, 2019, **4**, 881–889.
30 A. M. Kotulska, A. Pilch-Wróbel, S. Lahtinen, T. Soukka and A. Bednarkiewicz, *Light: Sci. Appl.*, 2022, **11**, 1–14.
31 N. J. Krasutsky, W. E. Case and J. S. Chivian, *J. Appl. Phys.*, 1979, **50**, 3142–3145.
32 W. Lenth and R. M. M. Macfarlane, *J. Lumin.*, 1990, **45**, 346–350.
33 H. Zellmer, P. Riedel and A. Tünnermann, *Appl. Phys. B*, 1999, **69**, 417–421.
34 R. Scheps, *Prog. Quantum Electron.*, 1996, **20**, 271–358.
35 T. Sandrock, H. Scheife, E. Heumann and G. Huber, *Opt. Lett.*, 1997, **22**, 808–810.
36 P. Goldner and F. Pelle, *Opt. Mater.*, 1996, **5**, 239–249.
37 N. J. Krasutsky, *J. Appl. Phys.*, 1983, **54**, 1261–1267.
38 N. Pelletier-Allard and R. Pelletier, *Opt. Commun.*, 1991, **81**, 247–250.
39 M. F. Joubert, S. Guy and B. Jacquier, *Phys. Rev. B: Condens. Matter Mater. Phys.*, 1993, **48**, 10031–10037.
40 B. P. Scott, F. Zhao, R. S. F. Chang and N. Djeu, *Opt. Lett.*, 1993, **18**, 113.
41 L. Yang, B. Zhang, K. Yin, T. Wu, Y. Zhao and J. Hou, *Photonics Res.*, 2018, **6**, 417.
42 M. Malinowski, A. Wnuk, Z. Frukacz, G. Chadeyron, R. Mahiou, S. Guy and M. F. Joubert, *Journal of Alloys and Compounds*, Elsevier, 2001, vol. 323–324, pp. 731–735.

43 T. R. Gosnell, *Electron. Lett.*, 1997, **33**, 411.
44 S. Guy, D. P. Shepherd, M. F. Joubert, B. Jacquier and H. Poignant, *J. Opt. Soc. Am. B*, 1997, **14**, 926.
45 F. Auzel and Y. H. Chen, *J. Non-Cryst. Solids*, 1995, **184**, 57–60.
46 P. Xie and T. R. Gosnell, *Opt. Lett.*, 1995, **20**, 1014.
47 O. K. Liu, Y. H. Chen and J. V. Beitz, *J. Lumin.*, 1999, **81**, 7–12.
48 S. Guy, M. F. Joubert and B. Jacquier, *J. Lumin.*, 1997, **72–74**, 65–67.
49 M. F. Joubert, S. Guy, C. Linarès, B. Jacquier and J. L. Adam, *J. Non-Cryst. Solids*, 1995, **184**, 98–102.
50 H. Ni and S. C. Rand, *Opt. Lett.*, 1991, **16**, 1424.
51 M. F. Joubert, S. Guy, S. Cuerq and P. A. Tanner, *J. Lumin.*, 1997, **75**(4), 287–293.
52 B. C. Collings and A. J. Silversmith, *J. Lumin.*, 1994, **62**, 271–279.
53 I. R. Martín, C. Goutaudier, S. Guy, Y. Guyot, G. Boulon, M.-T. Cohen-Adad and M.-F. Joubert, *Phys. Rev. B: Condens. Matter Mater. Phys.*, 1999, **60**, 7252–7257.
54 E. Bielejec, E. Kisel and A. Silversmith, *J. Lumin.*, 1997, **72–74**, 62–64.
55 N. Kodama and T. Park, *J. Phys.: Condens. Matter*, 1999, **11**, 4775–4782.
56 M. Bouffard, J. P. Jouart and G. Mary, *Phys. Status Solidi B*, 1996, **193**, 239–245.
57 A. W. Kueny, W. E. Case and M. E. Koch, *J. Opt. Soc. Am. B*, 1993, **104**(10), 1834–1839.
58 F. Auzel and Y. Chen, *J. Lumin.*, 1995, **65**, 45–56.
59 S. Kück and I. Sokólska, *Chem. Phys. Lett.*, 2000, **325**, 257–263.
60 A. Tymiński and T. Grzyb, *J. Lumin.*, 2017, **181**, 411–420.
61 A. Tymiński, T. Grzyb and S. Lis, *J. Am. Ceram. Soc.*, 2016, **99**, 3300–3308.
62 T. V. Gavrilović, D. J. Jovanović, V. Lojpur and M. D. Dramićanin, *Sci. Rep.*, 2014, **4**, 4209.
63 K. Kadono, H. Higuchi, M. Takahashi, Y. Kawamoto and H. Tanaka, *J. Non-Cryst. Solids*, 1995, **184**, 309–313.
64 I.-I. Oprea, H. Hesse and K. Betzler, *Phys. Status Solidi B*, 2005, **242**, R109–R111.
65 S. Sinha, M. K. Mahata and K. Kumar, *New J. Chem.*, 2019, **43**, 5960–5971.
66 Y. Liu, Y. Chen, Y. Lin, Q. Tan, Z. Luo and Y. Huang, *J. Opt. Soc. Am. B*, 2007, **24**, 1046–1052.
67 M. Back, E. Trave, N. Mazzucco, P. Riello and A. Benedetti, *Nanoscale*, 2017, **9**, 6353–6361.
68 S. Heer, K. Kömpe, H. U. Güdel and M. Haase, *Adv. Mater.*, 2004, **16**, 2102–2105.
69 B. Szefczyk, R. Roszak and S. Roszak, *RSC Adv.*, 2014, **4**, 22526–22535.
70 C. dos S. Bezerra and M. E. G. Valerio, *Phys. B*, 2016, **501**, 106–112.
71 S. Janssens, G. V. M. Williams and D. Clarke, *J. Appl. Phys.*, 2011, **109**, 511.
72 M. J. Weber, *Phys. Rev. B: Condens. Matter Mater. Phys.*, 1973, **8**, 54–64.
73 A. A. Kaminskiĭ, *Crystalline lasers: physical processes and operating schemes*, 1996.
74 T. Miyakawa and D. L. Dexter, *Phys. Rev. B: Condens. Matter Mater. Phys.*, 1970, **1**, 2961–2969.
75 N. Yamada, S. Shionoya and T. Kushida, *J. Phys. Soc. Jpn.*, 1972, **32**, 1577–1586.
76 J. M. Collins and B. Di Bartolo, *J. Lumin.*, 1996, **69**, 335–341.
77 E. S. Levy, C. A. Tajon, T. S. Bischof, J. Iafrati, A. Fernandez-Bravo, D. J. Garfield, M. Chamanzar, M. M. Maharbiz, V. S. Sohal, P. J. Schuck, B. E. Cohen and E. M. Chan, *ACS Nano*, 2016, **10**, 8423–8433.
78 N. J. J. J. Johnson, S. He, S. Diao, E. M. Chan, H. Dai and A. Almutairi, *J. Am. Chem. Soc.*, 2017, **139**, 3275–3282.
79 A. Bednarkiewicz, E. M. Chan and K. Prorok, *Nanoscale Adv.*, 2020, **2**, 4863–4872.
80 K. W. C. Kwock, C. Lee, A. Teitelboim, Y. Liu, K. Yao, S. B. Alam, B. E. Cohen, E. M. Chan and P. J. Schuck, *J. Phys. Chem. C*, 2021, **125**, 23976–23982.
81 G. Yi, H. Lu, S. Zhao, Y. Ge, W. Yang, D. Chen and L. H. Guo, *Nano Lett.*, 2004, **4**, 2191–2196.
82 H.-X. Mai, Y.-W. Zhang, R. Si, Z.-G. Yan, L. Sun, L.-P. You and C.-H. Yan, *J. Am. Chem. Soc.*, 2006, **128**, 6426–6436.
83 J. C. Boyer, F. Vetrone, L. A. Cuccia and J. A. Capobianco, *J. Am. Chem. Soc.*, 2006, **128**, 7444–7445.
84 H. S. Qian and Y. Zhang, *Langmuir*, 2008, **24**, 12123–12125.
85 G. Yi and G. Chow, *Chem. Mater.*, 2007, **19**, 341–343.
86 X. Chen, D. Peng, Q. Ju and F. Wang, *Chem. Soc. Rev.*, 2015, **44**, 1318–1330.
87 C. Song, Z. Ye, G. Wang, J. Yuan and Y. Guan, *ACS Nano*, 2010, **4**, 5389–5397.
88 X. Liu, C. H. Yan and J. A. Capobianco, *Chem. Soc. Rev.*, 2015, **44**, 1299–1301.
89 J. W. Stouwdam and F. C. J. M. Van Veggel, *Langmuir*, 2004, **20**, 11763–11771.
90 M. M. Lezhnina, T. Jüstel, H. Kätker, D. U. Wiechert and U. H. Kynast, *Adv. Funct. Mater.*, 2006, **16**, 935–942.
91 X. Li, F. Zhang and D. Zhao, *Chem. Soc. Rev.*, 2015, **44**, 1346–1378.
92 C. C. S. Pedroso, V. R. Mann, K. Zuberbühler, M. F. Bohn, J. Yu, V. Altoe, C. S. Craik and B. E. Cohen, *ACS Nano*, 2021, **15**, 18374–18384.
93 D. J. Gargas, E. M. Chan, A. D. Ostrowski, S. Aloni, M. V. P. Altoe, E. S. Barnard, B. Sanii, J. J. Urban, D. J. Milliron, B. E. Cohen and P. J. Schuck, *Nat. Nanotechnol.*, 2014, **9**, 300–305.
94 S. Wen, J. Zhou, K. Zheng, A. Bednarkiewicz, X. Liu and D. Jin, *Nat. Commun.*, 2018, **9**, 2415.
95 Y. Liu, Y. Lu, X. Yang, X. Zheng, S. Wen, F. Wang, X. Vidal, J. Zhao, D. Liu, Z. Zhou, C. Ma, J. Zhou, J. A. Piper, P. Xi and D. Jin, *Nature*, 2017, **543**, 229–233.
96 K. Prorok, A. Bednarkiewicz, B. Cichy, A. Gnach, M. Misiak, M. Sobczyk and W. Strek, *Nanoscale*, 2014, **6**, 1855–1864.
97 Q. Su, S. Han, X. Xie, H. Zhu, H. Chen, C. K. Chen, R. S. Liu, X. Chen, F. Wang and X. Liu, *J. Am. Chem. Soc.*, 2012, **134**, 20849–20857.
98 R. Arppe, I. Hyppänen, N. Perälä, R. Peltomaa, M. Kaiser, C. Würth, S. Christ, U. Resch-Genger, M. Schäferling and T. Soukka, *Nanoscale*, 2015, **7**, 11746–11757.

99 C. Dong, J. Pichaandi, T. Regier and F. C. J. M. van Veggel, *J. Phys. Chem. C*, 2011, **115**, 15950–15958.
100 J.-C. Boyer and F. C. J. M. van Veggel, *Nanoscale*, 2010, **2**, 1417–1419.
101 F. T. Rabouw, P. T. Prins, P. Villanueva-Delgado, M. Castelijns, R. G. Geitenbeek and A. Meijerink, *ACS Nano*, 2018, **12**, 4812–4823.
102 H. Deng, S. Yang, S. Xiao, H. M. Gong and Q. Q. Wang, *J. Am. Chem. Soc.*, 2008, **6**, 2032–2040.
103 M. Misiak, K. Prorok, B. Cichy, A. Bednarkiewicz and W. Stręk, *Opt. Mater.*, 2013, **35**, 1124–1128.
104 K. Prorok, A. Gnach, A. Bednarkiewicz and W. Stręk, *J. Lumin.*, 2013, **140**, 103–109.
105 Y. Wang, *Nanoscale*, 2019, **11**, 10852–10858.
106 B. Zhou, L. Tao, Y. H. Tsang and W. Jin, *J. Mater. Chem. C*, 2013, **1**, 4313–4318.
107 G. Chen, J. Shen, T. Y. Ohulchanskyy, N. J. Patel, A. Kutikov, Z. Li, J. Song, R. K. Pandey, H. Ågren, P. N. Prasad and G. Han, *ACS Nano*, 2012, **6**, 8280–8287.
108 Y. Shang, S. Hao, W. Shao, T. Chen, Y. Zhu and C. Yang, *J. Mater. Chem. C*, 2020, **8**, 2847–2851.
109 J. Wang, F. Wang, C. Wang, Z. Liu and X. Liu, *Angew. Chem., Int. Ed.*, 2011, **50**, 10369–10372.
110 Z. Wang and A. Meijerink, *J. Phys. Chem. C*, 2018, **122**, 26298–26306.
111 Z. Li, L. Wang, Z. Wang, X. Liu and Y. Xiong, *J. Phys. Chem. C*, 2011, **115**, 3291–3296.
112 X. Kang, Z. Cheng, C. Li, D. Yang, M. Shang, P. Ma, G. Li, N. Liu and J. Lin, *J. Phys. Chem. C*, 2011, **115**, 15801–15811.
113 L. Liang, Y. Liu, C. Bu, K. Guo, W. Sun, N. Huang, T. Peng, B. Sebo, M. Pan, W. Liu, S. Guo and X.-Z. Zhao, *Adv. Mater.*, 2013, **25**, 2174–2180.
114 B. Zhang, J. Meng, X. Mi, C. Zhang, Z. Zhang and H. Zheng, *RSC Adv.*, 2018, **8**, 37618–37622.
115 J. Zhao, T. Jia, X. Wang and X. Kong, *J. Nanomater.*, 2014, **2014**, 821706.
116 P. Yuan, Y. H. Lee, M. K. Gnanasammandhan, Z. Guan, Y. Zhang and Q.-H. Xu, *Nanoscale*, 2012, **4**, 5132–5137.
117 B. Dong, S. Xu, J. Sun, S. Bi, D. Li, X. Bai, Y. Wang, L. Wang and H. Song, *J. Mater. Chem.*, 2011, **21**, 6193–6200.
118 Z. Wang, C. Wang, Q. Han, G. Wang, M. Zhang, J. Zhang, W. Gao and H. Zheng, *Mater. Res. Bull.*, 2017, **88**, 182–187.
119 Y. Chen, C. D'Amario, A. Gee, H. T. T. Duong, O. Shimoni and S. M. Valenzuela, *Acta Biomater.*, 2020, **102**, 384–393.
120 X. Liu, X. Zhang, G. Tian, W. Yin, L. Yan, L. Ruan, Z. Yang, D. Xiao and Z. Gu, *CrystEngComm*, 2014, **16**, 5650–5661.
121 S. Niu, Y. Zhou, H. Yu, C. Lu and K. Han, *Energy Convers. Manage.*, 2017, **149**, 495–504.
122 L. Guerrini, R. A. Alvarez-Puebla and N. Pazos-Perez, *Materials*, 2018, **11**, 1154.
123 S. F. Himmelstoß and T. Hirsch, *Part. Part. Syst. Charact.*, 2019, **36**, 1900235.
124 P. Dolcet, A. Mambrini, M. Pedroni, A. Speghini, S. Gialanella, M. Casarin and S. Gross, *RSC Adv.*, 2015, **5**, 16302–16310.
125 C. Dubey, A. Yadav, D. Baloni, S. Kachhap, S. K. Singh and A. K. Singh, *RSC Adv.*, 2023, **13**, 20975–20983.
126 A. Kruk, *Materials*, 2020, **13**, 4928.
127 J. Mitrić, U. Ralević, M. Mitrić, J. Ćirković, G. Križan, M. Romčević, M. Gilić and N. Romčević, *J. Raman Spectrosc.*, 2019, **50**, 802–808.
128 D. Errandonea, O. Gomis, P. Rodríguez-Hernández, A. Muñoz, J. Ruiz-Fuertes, M. Gupta, S. N. Achary, A. Hirsch, F. J. Manjon, L. Peters, G. Roth, A. K. Tyagi and M. Bettinelli, *J. Phys.: Condens. Matter*, 2018, **30**, 065401.
129 S. Kostić, Z. Lazarević, V. Radojević, A. Milutinović, M. Romčević, N. Romčević and A. Valčić, *Mater. Res. Bull.*, 2015, **63**, 80–87.
130 A. K. Singh, K. Kumar, A. C. Pandey, O. Parkash, S. B. Rai and D. Kumar, *Appl. Phys. B*, 2011, **104**, 1035–1041.
131 H. M. Gong, Z. K. Zhou, S. Xiao, X. R. Su and Q. Q. Wang, *Plasmonics*, 2008, **3**, 59–64.
132 Z. Ma, Y. Yu, S. Shen, H. Dai, L. Yao, Y. Han, X. Wang, J.-B. Han and L. Li, *Sci. Rep.*, 2016, **6**, 18857.
133 Q. Q. Wang, J. B. Han, D. L. Guo, S. Xiao, Y. B. Han, H. M. Gong and X. W. Zou, *Nano Lett.*, 2007, **7**, 723–728.
134 A. Fernandez-Bravo, K. Yao, E. S. Barnard, N. J. Borys, E. S. Levy, B. Tian, C. A. Tajon, L. Moretti, M. V. Altoe, S. Aloni, K. Beketayev, F. Scotognella, B. E. Cohen, E. M. Chan and P. J. Schuck, *Nat. Nanotechnol.*, 2018, **13**, 1.
135 S. Kück, A. Diening, E. Heumann, E. Mix, T. Sandrock, K. Sebald and G. Huber, *J. Alloys Compd.*, 2000, **300**, 65–70.
136 N. J. Krasutsky, *J. Appl. Phys.*, 1983, **54**, 1261–1267.
137 M. Rathaiah, I. R. Martín, P. Babu, K. Linganna, C. K. Jayasankar, V. Lavín and V. Venkatramu, *Opt. Mater.*, 2015, **39**, 16–20.
138 E. Osiac, S. Kück, E. Heumann, G. Huber, E. Sani, A. Toncelli and M. Tonelli, *Opt. Mater.*, 2003, **24**, 537–545.
139 P. Babu, I. R. Martín, K. Venkata Krishnaiah, H. J. Seo, V. Venkatramu, C. K. Jayasankar and V. Lavín, *Chem. Phys. Lett.*, 2014, **600**, 34–37.
140 M. Plöschner, D. Denkova, S. de Camillis, M. Das, L. M. Parker, X. Zheng, Y. Lu, S. Ojosnegros and J. A. Piper, *Opt. Express*, 2020, **28**, 24308.
141 T. Sandrock, E. Heumann, G. Huber, V. Lupei, B. Bejan and E. Osiac, *Optical Society of America. Australian Council on Quantum Electronics. International Quantum Electronics Conference (20th: 1996: Sydney, N.S.W.)*, Optical Society of America, Sydney, 1996, p. ThQ7.
142 H. Wu, B. Pan, Q. Zhao, C. Wang, R. Pu, C. Liu, Z. Chen, Z. Luo, J. Huang, W. Wei, T. Chen and Q. Zhan, *Adv. Photonics*, 2024, **6**(5), 056010.
143 M. E. Koch, A. W. Kueny and W. E. Case, *Appl. Phys. Lett.*, 1990, **56**, 1083–1085.
144 E. Osiac, E. Heumann, G. Huber, S. Kuck, E. Sani, A. Toncelli and M. Tonelli, *Conference on Lasers and Electro-Optics Europe – Technical Digest*, 2003.
145 A. Schnitzler, J. Bahler, J. Noonan and L. Esterowitz, *Appl. Opt.*, 1968, **7**, 2053–2070.
146 C. Lee, E. Z. Xu, K. W. C. Kwock, A. Teitelboim, Y. Liu, N. Fardian-Melamed, C. C. S. Pedroso, H. S. Park, J. Kim, S. D. Pritzl, S. H. Nam, T. Lohmueller, P. Ercius, Y. D. Suh, B. E. Cohen, E. M. Chan and P. J. Schuck, *Nature*, 2023, **618**, 951–958.

147 J.-A. Pan, A. Skripka, C. Lee, X. Qi, A. L. Pham, J. J. Woods, R. J. Abergel, P. J. Schuck, B. E. Cohen and E. M. Chan, *J. Am. Chem. Soc.*, 2024, **146**, 7487–7497.
148 L. Schermelleh, R. Heintzmann and H. Leonhardt, *J. Cell Biol.*, 2010, **190**, 165–175.
149 G. Vicidomini, P. Bianchini and A. Diaspro, *Nat. Methods*, 2018, **15**, 173–182.
150 D. Jin, P. Xi, B. Wang, L. Zhang, J. Enderlein and A. M. van Oijen, *Nat. Methods*, 2018, **15**, 1–9.
151 L. Francés-Soriano, J. Ferrera-González, M. González-Béjar and J. Pérez-Prieto, *Anal. Bioanal. Chem.*, 2022, **414**, 4291–4310.
152 W. Li, G. S. Kaminski Schierle, B. Lei, Y. Liu and C. F. Kaminski, *Chem. Rev.*, 2022, **122**, 12495–12543.
153 M. G. L. Gustafsson, *J. Microsci.*, 2000, **198**, 82–87.
154 M. G. L. Gustafsson, *Proc. Natl. Acad. Sci. U. S. A.*, 2005, **102**, 13081–13086.
155 J. M. Gerton, L. A. Wade, G. A. Lessard, Z. Ma and S. R. Quake, *Phys. Rev. Lett.*, 2004, **93**, 180801.
156 N. Mauser and A. Hartschuh, *Chem. Soc. Rev.*, 2014, **43**, 1248–1262.
157 M. J. Rust, M. Bates and X. Zhuang, *Nat. Methods*, 2006, **3**, 793–796.
158 E. Betzig, G. H. Patterson, R. Sougrat, O. W. Lindwasser, S. Olenych, J. S. Bonifacino, M. W. Davidson, J. Lippincott-Schwartz and H. F. Hess, *Science*, 2006, **313**, 1642–1645.
159 S. W. Hell and J. Wichmann, *Opt. Lett.*, 1994, **19**, 780.
160 D. Denkova, M. Ploschner, M. Das, L. M. Parker, X. Zheng, Y. Lu, A. Orth, N. H. Packer and J. A. Piper, *Nat. Commun.*, 2019, **10**, 1–12.
161 B. Liu, C. Chen, X. Di, J. Liao, S. Wen, Q. P. Su, X. Shan, Z.-Q. Xu, L. A. Ju, C. Mi, F. Wang and D. Jin, *Nano Lett.*, 2020, **20**, 4775–4781.
162 C. Chen, F. Wang, S. Wen, Q. P. Su, M. C. L. L. Wu, Y. Liu, B. Wang, X. Shan, M. Kianinia, I. Aharonovich, M. Toth, S. P. Jackson, P. Xi and D. Jin, *Nat. Commun.*, 2018, **9**, 4–9.
163 R. Kolesov, R. Reuter, K. Xia, R. Stöhr, A. Zappe and J. Wrachtrup, *Phys. Rev. B: Condens. Matter Mater. Phys.*, 2011, **84**, 1–4.
164 F. Helmchen and W. Denk, *Nat. Methods*, 2005, **2**, 932–940.
165 W. Denk, J. H. Strickler and W. W. Webb, *Science*, 1990, **248**, 73–76.
166 M. Oheim, E. Beaurepaire, E. Chaigneau, J. Mertz and S. Charpak, *J. Neurosci. Methods*, 2001, **111**, 29–37.
167 L. Caillat, B. Hajj, V. Shynkar, L. Michely, D. Chauvat, J. Zyss and F. Pellé, *Appl. Phys. Lett.*, 2013, **102**, 143114.
168 S. Lamon, H. Yu, Q. Zhang and M. Gu, *Light: Sci. Appl.*, 2024, **13**, 252.
169 S. Li, F. Li, N. Kong, J. Liu and X. Zhu, *Adv. Healthcare Mater.*, 2023, **12**, e2302276.
170 J. Yao, M. Yang and Y. Duan, *Chem. Rev.*, 2014, **114**, 6130–6178.
171 T.-M. T. M. Liu, J. Conde, T. Lipiński, A. Bednarkiewicz and C.-C. C. C. Huang, *Prog. Mater. Sci.*, 2017, **88**, 89–135.
172 T.-M. T. M. Liu, J. Conde, T. Lipiński, A. Bednarkiewicz and C.-C. C. C. Huang, *NPG Asia Mater.*, 2016, **8**, 1–25.
173 F. Auzel, *Chem. Rev.*, 2004, **104**, 139–173.
174 W. Park, D. Lu and S. Ahn, *Chem. Soc. Rev.*, 2015, **44**, 2940–2962.
175 S. Hao, J. Liu, M. Tan and G. Chen, *Upconversion Enhancement Using Epitaxial Core–Shell Nanostructures*, CRC Press, 1st edn, 2016.
176 S. Han, R. Deng, Q. Gu, L. Ni, U. Huynh, J. Zhang, Z. Yi, B. Zhao, H. Tamura, A. Pershin, H. Xu, Z. Huang, S. Ahmad, M. Abdi-Jalebi, A. Sadhanala, M. L. Tang, A. Bakulin, D. Beljonne, X. Liu and A. Rao, *Nature*, 2020, **587**, 594–599.
177 D. J. Garfield, N. J. Borys, S. M. Hamed, N. A. Torquato, C. A. Tajon, B. Tian, B. Shevitski, E. S. Barnard, Y. D. Suh, S. Aloni, J. B. Neaton, E. M. Chan, B. E. Cohen and P. J. Schuck, *Nat. Photonics*, 2018, **12**, 402–407.
178 A. D. Ostrowski, E. M. Chan, D. J. Gargas, E. M. Katz, G. Han, P. J. Schuck, D. J. Milliron and B. E. Cohen, *ACS Nano*, 2012, **6**, 2686–2692.
179 M. Kaiser, C. Würth, M. Kraft, I. Hyppänen, T. Soukka and U. Resch-Genger, *Nanoscale*, 2017, **9**, 10051–10058.
180 B. E. Cohen, *Nature*, 2010, **467**, 407–408.
181 Y. Zhong, G. Tian, Z. Gu, Y. Yang, L. Gu, Y. Zhao, Y. Ma and J. Yao, *Adv. Mater.*, 2014, **26**, 2831–2837.
182 I. Medintz and N. Hildebrandt, *FRET – Förster Resonance Energy Transfer: From Theory to Applications*, Wiley-VCH Verlag, 2013.
183 C. Wang, H. Lin, Z. Xu, Y. Huang, M. G. Humphrey and C. Zhang, *ACS Appl. Mater. Interfaces*, 2016, **8**, 6621–6628.
184 E. Carrasco, B. del Rosal, F. Sanz-Rodríguez, Á. J. de la Fuente, P. H. Gonzalez, U. Rocha, K. U. Kumar, C. Jacinto, J. G. Solé and D. Jaque, *Adv. Funct. Mater.*, 2015, **25**, 615–626.
185 D. Ruiz, B. del Rosal, M. Acebrón, C. Palencia, C. Sun, J. Cabanillas-González, M. López-Haro, A. B. Hungría, D. Jaque and B. H. Juarez, *Adv. Funct. Mater.*, 2016, **27**, 1604629.
186 E. Carrasco, B. del Rosal, F. Sanz-Rodríguez, Á. J. de la Fuente, P. H. Gonzalez, U. Rocha, K. U. Kumar, C. Jacinto, J. G. Solé and D. Jaque, *Adv. Funct. Mater.*, 2015, **25**, 615–626.
187 J. P. Feist, A. L. Heyes and S. Seefelt, *Proc. Inst. Mech. Eng., Part A*, 2003, **217**, 193–200.
188 C. Abram, B. Fond and F. Beyrau, *Prog. Energy Combust. Sci.*, 2018, **64**, 93–156.
189 R. G. Geitenbeek, A.-E. Nieuwelink, T. S. Jacobs, B. B. V. Salzmann, J. Goetze, A. Meijerink and B. M. Weckhuysen, *ACS Catal.*, 2018, **8**, 2397–2401.
190 D. Jaque and F. Vetrone, *Nanoscale*, 2012, **4**, 4301–4326.
191 C. D. S. Brites, A. Millán and L. D. Carlos, *Handbook on the Physics and Chemistry of Rare Earths*, Elsevier B.V., 2016, vol. 49, pp. 339–427.
192 M. Dramićanin, *Luminescence Thermometry*, 2018.
193 A. Rabhiou, J. Feist, A. Kempf, S. Skinner and A. Heyes, *Sens. Actuators, A*, 2011, **169**, 18–26.
194 X. D. Wang, O. S. Wolfbeis and R. J. Meier, *Chem. Soc. Rev.*, 2013, **42**, 7834–7869.
195 C. D. S. Brites, P. P. Lima, N. J. O. Silva, A. Millán, V. S. Amaral, F. Palacio and L. D. Carlos, *Nanoscale*, 2012, **4**, 4799–4829.

196 B. del Rosal, E. Ximendes, U. Rocha and D. Jaque, *Adv. Opt. Mater.*, 2017, **5**, 1600508.
197 C. D. S. Brites, A. Millán and L. D. D. Carlos, *Handb. Phys. Chem. Rare Earths*, 2016, **49**, 339–427.
198 A. Bednarkiewicz, L. Marciniak, L. D. D. Carlos and D. Jaque, *Nanoscale*, 2020, **12**, 14405–14421.
199 A. Bednarkiewicz, D. Wawrzynczyk, A. Gagor, L. Kepinski, M. Kurnatowska, L. Krajczyk, M. Nyk, M. Samoc and W. Strek, *Nanotechnology*, 2012, **23**, 145705.
200 J. Drabik, R. Kowalski and L. Marciniak, *Sci. Rep.*, 2020, **10**, 1–11.
201 K. Trejgis, F. Tian, J. Li, A. Bednarkiewicz and L. Marciniak, *Mater. Res. Bull.*, 2021, **139**, 111288.
202 K. Trejgis, K. Ledwa, K. Maciejewska, L. Li and L. Marciniak, *Sci. Rep.*, 2022, **12**, 1–14.
203 L. Marciniak, A. Bednarkiewicz and K. Elzbieciak, *J. Mater. Chem. C*, 2018, **6**, 7568–7575.
204 K. Trejgis, K. Maciejewska, A. Bednarkiewicz and L. Marciniak, *ACS Appl. Nano Mater.*, 2020, **3**, 4818–4825.
205 K. Trejgis, R. Lisiecki, A. Bednarkiewicz and L. Marciniak, *J. Lumin.*, 2020, **224**, 117295.
206 J. Drabik, K. Ledwa and Ł. Marciniak, *Nanomaterials*, 2020, **10**, 1333.
207 K. Trejgis, R. Lisiecki, A. Bednarkiewicz and L. Marciniak, *J. Lumin.*, 2020, **224**, 117295.
208 J. Drabik and L. Marciniak, *ACS Appl. Nano Mater.*, 2020, **3**, 3798–3806.
209 K. Trejgis, A. Bednarkiewicz and Ł. Marciniak, *Nanoscale*, 2020, **12**, 4667–4675.
210 A. Bednarkiewicz, K. Trejgis, J. Drabik, A. Kowalczyk and L. Marciniak, *ACS Appl. Mater. Interfaces*, 2017, **9**(49), 43081–43089.
211 N. Fardian-Melamed, A. Skripka, C. Lee, B. Ursprung, T. Darlington, A. Teitelboim, X. Qi, M. Wang, J. Gerton, B. E. Cohen, E. M. Chan and P. J. Schuck, *Nature*, DOI: **10.1038/s41586-41024-08221-41582**, preprint available at **https://arxiv.org/abs/42404.02026**.
212 A. Skripka, Z. Zhang, X. Qi, B. Ursprung, P. Ercius, B. E. Cohen, P. J. Schuck, D. Jaque and E. M. Chan, *Nat. Photonics*, DOI: **10.1038/s41566-024-01577-x**, preprint available at **https://arxiv.org/abs/2403.04098**.
213 I. V. Dyakonov, I. A. Pogorelov, I. B. Bobrov, A. A. Kalinkin, S. S. Straupe, S. P. Kulik, P. V. Dyakonov and S. A. Evlashin, *Phys. Rev. Appl.*, 2018, **10**, 044048.
214 C. Lee and P. J. Schuck, *Annu. Rev. Phys. Chem.*, 2023, **74**, 415–438.
215 S. Zanella, M. A. Hernández-Rodríguez, L. Fu, L. D. Carlos, R. A. S. Ferreira, C. D. S. Brites, S. Zanella, M. A. Hernández-Rodríguez, L. Fu, L. D. Carlos, R. A. S. Ferreira and C. D. S. Brites, *Adv. Opt. Mater.*, 2022, 2200138.
216 H. Bian, X. Qin, Y. Wu, Z. Yi, S. Liu, Y. Wang, C. D. S. Brites, L. D. Carlos and X. Liu, *Adv. Mater.*, 2022, **34**, 2101895.
217 Y. Wang, B. Liu, L. Ding, C. Chen, X. Shan, D. Wang, M. Tian, J. Song, Z. Zheng, X. Xu, X. Zhong and F. Wang, *Laser Photonics Rev.*, 2024, 2400746.
218 S. Fischer, N. D. Bronstein, J. K. Swabeck, E. M. Chan and A. P. Alivisatos, *Nano Lett.*, 2016, **16**, 7241–7247.
219 A. Gnach and A. Bednarkiewicz, *Nano Today*, 2012, **7**, 532–563.
220 U. Kostiv, Z. Farka, M. J. Mickert, H. H. Gorris, N. Velychkivska, O. Pop-Georgievski, M. Pastucha, E. Odstrčilíková, P. Skládal and D. Horák, *Biomacromolecules*, 2020, **21**, 4502–4513.
221 F. Wang and X. Liu, *J. Am. Chem. Soc.*, 2008, **130**, 5.
222 H. H. Gorris and O. S. Wolfbeis, *Angew. Chem., Int. Ed.*, 2013, **52**, 3584–3600.
223 E. M. Chan, G. Han, J. D. Goldberg, D. J. Gargas, A. D. Ostrowski, P. J. Schuck, B. E. Cohen and D. J. Milliron, *Nano Lett.*, 2012, **12**, 3839–3845.
224 G. Tian, Z. Gu, L. Zhou, W. Yin, X. Liu, L. Yan, S. Jin, W. Ren, G. Xing, S. Li, Y. Zhao, G. Tian, Z. Gu, L. Zhou, W. Yin, X. Liu, L. Yan, S. Jin, W. Ren, G. Xing, Y. Zhao and S. Li, *Adv. Mater.*, 2012, **24**, 1226–1231.
225 Y. Lu, J. Zhao, R. Zhang, Y. Liu, D. Liu, E. M. Goldys, X. Yang, P. Xi, A. Sunna, J. Lu, Y. Shi, R. C. Leif, Y. Huo, J. Shen, J. A. Piper, J. P. Robinson and D. Jin, *Nat. Photonics*, 2014, **8**, 32–36.
226 H. Chen, Z. Jiang, H. Hu, B. Kang, B. Zhang, X. Mi, L. Guo, C. Zhang, J. Li, J. Lu, L. Yan, Z. Fu, Z. Zhang, H. Zheng and H. Xu, *Nat. Photonics*, 2022, **16**, 651–657.
227 S. Schietinger, T. Aichele, H. Q. Wang, T. Nann and O. Benson, *Nano Lett.*, 2010, **10**, 134–138.
228 S. N. Sanders, T. H. Schloemer, M. K. Gangishetty, D. Anderson, M. Seitz, A. O. Gallegos, R. C. Stokes and D. N. Congreve, *Nature*, 2022, **604**, 474–478.
229 E. Z. Xu, C. Lee, S. D. Pritzl, A. S. Chen, T. Lohmueller, B. E. Cohen, E. M. Chan and P. J. Schuck, *Opt. Mater.: X*, 2021, **12**, 100099.
230 S. H. Nam, Y. M. Bae, Y. Il Park, J. H. Kim, H. M. Kim, J. S. Choi, K. T. Lee, T. Hyeon and Y. D. Suh, *Angew. Chem., Int. Ed.*, 2011, **50**, 6093–6097.
231 B. Tian, A. Fernandez-Bravo, H. Najafiaghdam, N. A. Torquato, M. V. P. Altoe, A. Teitelboim, C. A. Tajon, Y. Tian, N. J. Borys, E. S. Barnard, M. Anwar, E. M. Chan, P. J. Schuck and B. E. Cohen, *Nat. Commun.*, 2018, **9**, 4–11.
232 F. Ş. Boydağ, Sh. V. Mamedov, V. A. Alekperov and Y. Lenger Özcanli, *Opt. Spectrosc.*, 2003, **95**, 225–229.
233 S. Bhuckory, E. Hemmer, Y.-T. Wu, A. Yahia-Ammar, F. Vetrone and N. Hildebrandt, *Eur. J. Inorg. Chem.*, 2017, 5186–5195.
234 Y. Wang, K. Liu, X. Liu, K. Dohnalová, T. Gregorkiewicz, X. Kong, M. C. G. Aalders, W. J. Buma and H. Zhang, *J. Phys. Chem. Lett.*, 2011, **2**, 2083–2088.
235 L. Mattsson, K. D. Wegner, N. Hildebrandt and T. Soukka, *RSC Adv.*, 2015, **5**, 13270–13277.
236 K. Kuningas, T. Rantanen, T. Ukonaho, T. Lövgren and T. Soukka, *Anal. Chem.*, 2005, **77**, 7348–7355.
237 N. Sirkka, A. Lyytikäinen, T. Savukoski and T. Soukka, *Anal. Chim. Acta*, 2016, **925**, 82–87.
238 L. Liang, C. Wang, J. Chen, Q. J. Wang and X. Liu, *Nat. Photonics*, 2022, **16**, 712–717.
239 J. S. Dam, P. Tidemand-Lichtenberg and C. Pedersen, *Nat. Photonics*, 2012, **6**, 788–793.

240 A. Khalid, C. Xie, D. R. S. Cumming, I. G. Thayne, M. Sorel, M. Steer, M. Aziz and V. Pusino, *Optica*, 2017, **4**, 1498–1502.
241 I. M. Pavlovetc, K. Aleshire, G. V. Hartland and M. Kuno, *Phys. Chem. Chem. Phys.*, 2020, **22**, 4313–4325.
242 W. Chen, P. Roelli, H. Hu, S. Verlekar, S. P. Amirtharaj, A. I. Barreda, T. J. Kippenberg, M. Kovylina, E. Verhagen, A. Martínez and C. Galland, *Science*, 2021, **374**, 1264–1267.
243 R. Gordon, *Science*, 2021, **374**, 1201–1202.
244 N. Bloembergen, *Phys. Rev. Lett.*, 1959, **2**, 84.
245 D. B. Gatch, W. M. Dennis and W. M. Yen, *Appl. Opt.*, 2003, **42**, 615–620.
246 G. Temporão, S. Tanzilli, H. Zbinden, N. Gisin, T. Aellen, M. Giovannini and J. Faist, *Opt. Lett.*, 2006, **31**, 1094–1096.
247 H. C. Liu, C. Y. Song, E. Dupont, P. Poole, P. H. Wilson, B. J. Robinson and D. A. Thompson, *Electron. Lett.*, 1999, **35**, 2055–2056.
248 P. Roelli, D. Martin-Cano, T. J. Kippenberg and C. Galland, *Phys. Rev. X*, 2020, **10**, 031057.
249 A. Xomalis, X. Zheng, R. Chikkaraddy, Z. Koczor-Benda, E. Miele, E. Rosta, G. A. E. Vandenbosch, A. Martínez and J. J. Baumberg, *Science*, 2021, **374**, 1268–1271.
250 K. Ueno, E. G. Camargo, T. Katsumata, H. Goto, N. Kuze, Y. Kangawa and K. Kakimoto, *Jpn J. Appl. Phys.*, 2013, **52**, 092202.
251 P. Goldner and F. Pellé, *Opt. Mater.*, 1996, **5**, 239–249.
252 M. E. Koch, A. W. Kueny and W. E. Case, *Appl. Phys. Lett.*, 1990, **56**, 1083–1085.
253 T. Hebert, R. Wannemacher, R. M. MacFarlane and W. Lenth, *Appl. Phys. Lett.*, 1992, **60**, 2592–2594.
254 T. Sandrock, E. Heumann, G. Huber and B. H. T. Chai, *Advanced Solid State Lasers (1996)*, paper PM1, The Optical Society, 2017, p. PM1.
255 H. Zhu, X. Chen, L. M. Jin, Q. J. Wang, F. Wang and S. F. Yu, *ACS Nano*, 2013, **7**, 11420–11426.
256 T. Wang, H. Yu, C. K. Siu, J. Qiu, X. Xu and S. F. Yu, *ACS Photonics*, 2017, **4**, 1539–1543.
257 T. Wang, C. K. Siu, H. Yu, Y. Wang, S. Li, W. Lu, J. Hao, H. Liu, J. H. Teng, D. Y. Lei, X. Xu and S. F. Yu, *Inorg. Chem.*, 2018, **57**, 8200–8204.
258 P. Molina, E. Yraola, M. O. Ramírez, C. Tserkezis, J. L. Plaza, J. Aizpurua, J. Bravo-Abad and L. E. Bausá, *Nano Lett.*, 2016, **16**, 895–899.
259 Z. Chen, G. Dong, G. Barillaro, J. Qiu and Z. Yang, *Prog. Mater. Sci.*, 2021, **121**, 100814.
260 A. Fernandez-Bravo, K. Yao, E. S. Barnard, N. J. Borys, E. S. Levy, B. Tian, C. A. Tajon, L. Moretti, M. V. Altoe, S. Aloni, K. Beketayev, F. Scotognella, B. E. Cohen, E. M. Chan, P. J. Schuck, B. Tian, C. A. Tajon, L. Moretti, M. V. Altoe, S. Aloni, K. Beketayev, F. Scotognella, B. E. Cohen, E. M. Chan and P. J. Schuck, *Nat. Nanotechnol.*, 2018, **13**, 1.
261 Y. Liu, A. Teitelboim, A. Fernandez-Bravo, K. Yao, M. V. P. Altoe, S. Aloni, C. Zhang, B. E. Cohen, P. J. Schuck and E. M. Chan, *ACS Nano*, 2020, **14**, 1508–1519.
262 A. Fernandez-Bravo, D. Wang, E. S. Barnard, A. Teitelboim, C. Tajon, J. Guan, G. C. Schatz, B. E. Cohen, E. M. Chan, P. J. Schuck and T. W. Odom, *Nat. Mater.*, 2019, **18**, 1172–1176.

